Christian-Albrechts-University of Kiel
Faculty of Mathematics and Natural Sciences

Master's Thesis

Controls of Recent Patterns and Trends in Global Oceanic Oxygen Content

submitted by
Helene A. L. Hollitzer

In Partial Fulfilment of the Requirements for the
Degree of Master of Science

First Examiner: **Prof. Dr. Andreas Oschlies**
Second Examiner: **Dr. Lavinia Patara**
GEOMAR Helmholtz Centre for Ocean Research Kiel

Degree Programme: Biolocical Oceanography
Research Unit: Biogeochemical Modelling

Kiel, September 2023

Abstract

The global oceanic oxygen (O_2) inventory has declined by more than 2% over the last half century, threatening marine ecosystems and altering biogeochemical cycles. This study uses a high-resolution ocean model in hindcast mode, forced by atmospheric reanalysis data, to investigate how changing atmospheric forcing may have affected global and regional O_2 variability and long-term trends through changes in solubility, ventilation (diagnosed using CFC-12), and biological consumption. Alongside the standard hindcast run, two sensitivity experiments were performed to isolate the effects of interannual variability in wind stress and buoyancy forcing on the modulation of these dynamics. The time series of simulated global oceanic O_2 content can be clustered into four periods: (1) From 1958 to 1967, the O_2 inventory increased (218.7 ± 33.9 teramoles per decade) largely due to a buoyancy-induced increase in O_2 solubility. (2) From 1967 to 1994, O_2 gradually decreased by -46.6 ± 4.5 teramoles per decade due to buoyancy-induced decreases in both solubility and ocean ventilation. (3) Between 1994 and 2002, there was a transient low in the global oceanic O_2 inventory, likely linked to strong El Niño conditions in 1997-1998. (4) Thereafter, the decline continued, but at an accelerated rate of -108.6 ± 7.6 teramoles per decade; threefold less than the observed decline over the same period. For the past five decades, changes in wind stress have acted continuously to mitigate the dominant buoyancy-driven decline in global oceanic O_2, mainly in the intermediate waters of the Southern Hemisphere. This mitigation is primarily attributed to the intensification and poleward shift of westerly winds, and raises concerns about a potential acceleration of oxygen loss following the projected weakening of wind stress intensification in the Southern Hemisphere. On a regional scale, oxygen changes show substantial temporal and spatial variability, as do their underlying drivers. By identifying regional structures of dominant influences, this analysis contributes to a much-needed improved mechanistic understanding of O_2 changes, allows to better understand differences between simulated and observed O_2 changes, and in turn facilitates the anticipation of future global and regional O_2 inventory changes forced by ongoing climate change.

Acknowledgments

I would like to express my sincere gratitude to several individuals who have played a vital part in the completion of this Master's thesis.

First and foremost, I am deeply grateful to my supervisor, Lavinia Patara, for her constant support and guidance along the way. Lavinia was always there to answer my questions and provide invaluable advice. Her encouragement and the freedom she gave me to develop my own ideas has contributed greatly to the shaping of this thesis. I would also like to express my sincere gratitude to Andreas Oschlies for his constructive feedback and kind, supportive manner. Andreas not only generously provided his knowledge and expertise, but also made me feel valued within the research group.

I owe a special debt of gratitude to my friends and family who have stood by me throughout this time. To Adnan, I am truly grateful for every late night workout session that kept my back straight and allowed me to endure the long hours of study. To Jöran, your constant presence, listening ear and support during our breaks from work were truly irreplaceable. Finally, I would like to express my heartfelt thanks to Nil for your unfailing emotional and moral support. You have always kept my spirits up.

The collective encouragement, help and understanding of these individuals has been invaluable to the successful completion of this thesis. I could not have undertaken this journey without all of you.

Contents

1 Introduction **7**

1.1 Oxygen concentration controls . . . 7

1.2 Rationale . . . 11

2 Methods **13**

2.1 Model description . . . 13

2.2 Model simulations . . . 13

2.3 Analyses . . . 16

2.4 Observational data sets . . . 18

2.4.1 Oxygen, oxygen saturation concentration, and AOU . . . 19

2.4.2 Temperature and salinity . . . 20

2.4.3 Mixed layer depth . . . 20

2.4.4 Phytoplankton . . . 20

2.4.5 Zooplankton . . . 20

3 Model Performance **22**

3.1 Climatological mean state of oxygen . . . 22

3.2 Climatological mean state of controls . . . 24

3.2.1 Oxygen saturation concentration . . . 24

3.2.2 Controls of remineralisation . . . 25

3.2.3 Ocean ventilation . . . 26

4 Results **29**

4.1 Oxygen inventory from 1958-2018 . . . 29

4.1.1 Globally integrated oxygen change . . . 29

4.1.2 Regional patterns in oxygen trends . . . 30

4.2 Interannual and decadal variability . . . 31

4.3 Controls underlying oxygen trends . . . 34

4.3.1 Global scale controls . . . 34

4.3.2 Regional scale controls . . . 39

4.3.3 Regional in-depth analysis . . . 40

5 Discussion **43**

5.1 Limitations . . . 43

5.2 Past oxygen trends . . . 45

5.2.1 Buoyancy forcing-induced changes . . . 45

5.2.2 Wind stress-induced changes . . . 48

5.3 Oxygen dynamics related to the El Niño-Southern Oscillation . . . 52

5.4 Implications for future O_2 changes . . . 54

5.4.1 Trends in buoyancy forcing . . . 54

5.4.2 Trends in wind stress forcing . . . 54

5.5 Model-observation mismatch since the early 2000s 57

6 Conclusions **59**

A Appendix **72**

Declaration **102**

List of Abbreviations and Acronyms

AABW	Antarctic Bottom Water
AAIW	Antarctic Intermediate Water
AMOC	Atlantic Meridional Overturning Circulation
AOU	Apparent Oxygen Utilization
BUOY	Buoyancy forcing sensitivity experiment; performed by suppressing the interannual variability of wind stress, while the interannual variability of all variables needed to compute the air-sea fluxes of heat, freshwater, oxygen, and chlorofluorocarbon-12 was maintained
BUOY$_{\mathrm{ns}}$	Isolated non-steady-state components of the buoyancy forcing sensitivity experiment
C	Dissolved inorganic carbon
CFC	Chlorofluorocarbon
CFC-12	Chlorofluorocarbon-12
CLIM	Climatological experiment; performed by suppressing the interannual variability of all atmospheric variables needed to force the ocean model
GOBM	Global ocean biogeochemical model
HIND	Hindcast experiment; performed under interannual forcing (1958-2018) of JRA55-do
HIND$_{\mathrm{ns}}$	Isolated non-steady-state components of the hindcast simulation
MOC	Meridional Overturning Circulation
MLD	Mixed layer depth
N	Nitrogen
NADW	North Atlantic Deep Water
NH	Northern Hemisphere
NO$_3$	Nitrate
O$_2$	Oxygen
O$_2^{\mathrm{ns}}$	Non-steady-state components of O_2 fluxes; those that arise solely because of year-to-year atmospheric variability
O$_2^{\mathrm{sat}}$	Oxygen saturation concentration
O$_2^{\mathrm{ss}}$	Steady-state components of O_2 fluxes; those that exist under the suppression of interannual variability
OMZ	Oxygen minimum zone
P	Phosphorus
PO$_4$	Phosphate
POC	Particulate organic carbon
SAMW	Subantarctic Mode Water

SH	Southern Hemisphere
TCD	Thermocline depth
WIND	Wind stress sensitivity experiment; performed by suppressing the interannual variability of all variables needed to compute the air-sea fluxes of heat, freshwater, oxygen, and chlorofluorocarbon-12, while the interannual variability of wind stress was maintained
$\mathbf{WIND}_{\mathrm{ns}}$	Isolated non-steady-state components of wind stress sensitivity experiment

1 Introduction

Observed changes in oxygen (O_2) over the past 50 years have revealed that the global oceanic O_2 content of 227.4 ± 1.1 petamoles has decreased by more than 2% (Schmidtko et al. 2017). This decrease in oceanic oxygen content (i.e., deoxygenation) is an alarming response to climate change, with climate-model projections predicting that this trend of deoxygenation is set to persist, and even intensify over the coming century (Bopp et al. 2013; Oschlies 2021). Oxygen is a critical component of the marine environment, regulating the rates and pathways of remineralisation processes and the associated cycling of a number of important elements. The impacts are far-reaching as the chemical imprint of oxygen concentration propagates through ocean circulation. On global scale the oceanic oxygen content decreases as the residual of an increasing O_2 loss and a positive O_2 source term. While the O_2 source term may also alter in response to global warming, the sign of this change remains less certain. On smaller spatial and temporal scales, however, changes in O_2 are non-uniform (Stramma & Schmidtko 2021). Consideration of regional O_2 changes on smaller temporal scales produces a more sophisticated pattern of decadal fluctuations in O_2 concentrations, with large and systematic differences across ocean basins and depths, indicating different mechanisms responsible for O_2 changes in space and time (Schmidtko et al. 2017; Stramma & Schmidtko 2021). Here I aim to attribute the regional changes in O_2 inventories to the different causes, focusing on non-steady-state changes in O_2 (Box 1) on decadal and longer time scales in open ocean regions.

1.1 Oxygen concentration controls

The ocean takes up O_2 at the sea-surface through air-sea gas exchange. Through rapid equilibration rates, waters within the mixed layer are, to first order, in equilibrium with the O_2 partial pressure of the atmosphere, and thus close to saturation. Throughout the water column and in the sediments, O_2 is lost by the respiration of organic matter. In simplified terms (but see, e.g., Robinson 2019), marine respiration is foremost limited by the availability of organic substrates and is thus dependent on biological production in the surface ocean producing organic matter that eventually sinks into the ocean interior (Oschlies 2019). In the interior ocean, there are no significant oxygen sources and O_2 can only be supplied through ventilation, defined as the physical processes by which waters from the surface mixed layer, and associated properties, are injected into the ocean interior, isolated from the atmosphere for a timescale set by the patterns of interior transport (Portela et al. 2020).

Three main controls of O_2 change are inferred (Keeling et al. 2010; Oschlies 2019): (i) changes in initial O_2 concentrations in surface waters, i.e., before transport to the ocean interior; (ii) changes in biological production in the upper ocean and associated changes in biological consumption in the ocean interior; and (iii) changes in ventilation affecting the time span during which respiratory oxygen losses accumulate in ocean-interior since equilibration with the O_2 partial pressure of the atmosphere. Although these controls are distinguishable in concept, in the ocean they interact, as for example circulation can transport O_2 and nutrients to influence all three factors (Keeling et al. 2010).

Initial O_2 concentrations in the surface ocean depend primarily on O_2 solubility. While O_2 solubility is a function of both temperature and salinity, in the ocean, changes in salinity are minor and unlikely to have a substantial impact on O_2 saturation concentrations (Weiss 1970). Thus, non-steady-state changes in initial O_2 concentrations in the surface ocean depend mainly on mixed layer temperature and are modulated by both natural climate variability and anthropogenic climate change. Solubility-related

Box 1 The steady-state and non-steady-state concept

O_2 fluxes can be described in terms of two components (Hauck et al. 2020; Gruber et al. 2023): (i) steady-state components (O_2^{ss}), that represent the O_2 fluxes under constant climate conditions, and (ii) non-steady-state components (O_2^{ns}), that capture the O_2 fluxes related to anthropogenic climate change and natural climate variabiliy. In a steady-state ocean, the oceanic O_2 inventory remains stable and the global O_2 fluxes across the air-sea interface are balanced on global scale. Steady-state is reached when oceanic physical and biological processes are allowed sufficient time to adjust to constant climate forcing and become unchanging on interannual timescales. However, both anthropogenic climate change and natural climate variability shift the climate away from a constant state by causing changes in atmospheric forcing, such as alterations in wind patterns and heat and freshwater fluxes, leading to a non-steady-state ocean. This affects ocean circulation, temperature, salinity, and biology and leads to additional O_2 fluxes and changes in O_2 inventories.

changes associated with anthropogenic warming and the continuous ocean heat-uptake (von Schuckmann et al. 2020) are estimated to account for about half of the O_2 loss in the upper 1,000 m of the water column; at present, in the deep ocean the contribution is negligible (Schmidtko et al. 2017), implying that the dominant fraction must be explained by changes in biological consumption or ventilation.

As marine respiration is mostly substrate-limited, and the biological production of organic substrate is, in most ocean regions, nutrient or light-limited, total marine respiration is indirectly contingent upon nutrient concentrations in the sun-lit surface ocean (Oschlies 2019). Beginning with the industrial production of fertilisers in the 1950s, coastal waters have been subjected to extensive human inputs of nitrogen and phosphorus (i.e., eutrophication), causing intense coastal deoxygenation in affected areas (Rabalais 2019). Further, metabolic rates are temperature-dependent and, although temperatures are not affecting the total amount of respiration[1], changes in temperature shift the vertical profile of respiration with possible implications for the O_2 flux across the air-sea interface, the vertical nutrient gradient, and the burial of organic matter. In response to anthropogenic warming, for example, it has been proposed that the associated shoaling of remineralisation profiles, might cause O_2 deficits closer to the air-sea interface, rapid re-saturation through air-sea gas exchange, and a net O_2 influx (Segschneider & Bendtsen 2013; Oschlies 2019). Opposing this, shoaled remineralisation might lead to increased nutrient resupply to the euphotic zone and reduced burial of organic matter, both increasing the substrate available for respiration and associated biological oxygen consumption (Segschneider & Bendtsen 2013; Oschlies 2019). However, on global scale, warming-induced changes in biogeochemical processes are estimated to contribute less than 15% to the present O_2 decline (Schmidtko et al. 2017).

Ocean ventilation describes the transfer of fluid from the mixed layer into the ocean interior. Its past changes can be constrained through the use of conservative transient tracers such as chlorofluorocarbons (CFCs). With a 100% atmospheric source, CFCs enter the ocean through air-sea gas exchange and are carried within the ocean as a tracer of ocean ventilation (Patara et al. 2021). The process of ocean ventilation is a composite of two conceptual mechanisms: O_2-rich waters from the mixed layer are (i) transported into the permanent thermocline (i.e., subduction), where they are (ii) subjected to interior

[1] Assuming resource-limitation rather than temperature-limitation of biological production.

transport. Although subduction is the sole dynamical mechanism able to increase the global O_2 inventory, subsequent interior transport controls the spatial and temporal distribution of O_2 and dictates the time that subducted waters remain in the interior before being re-entrained into the surface mixed layer and re-saturated to initial O_2 concentrations (Portela et al. 2020). For example, anthropogenic warming induces a poleward migration of the isopycnal outcrops (Durack & Wijffels 2010), increasing the transit time of a water parcel, and thus the time for O_2 losses to accumulate, before being re-entrained into the surface mixed layer (Oschlies 2019).

It is important to note that the time scales at which changes in these mechanisms impact O_2 concentrations differ. The adjustment of the ocean to changes in the rate of water mass formation or its properties is gradual and related to depth. While the upper ocean adjusts to surface conditions after a couple of years, the deep ocean adjusts on millennial time scales (Grégoire et al. 2019), as altered water masses must first be transported to depth (Schmidtko et al. 2017); an important shortcut, however, is provided by particles that sink rapidly through the water column and, upon being respired, can generate oxygen signals also at depth. In contrast, a reduction in the large-scale overturning circulation, as now indicated by observations (Srokosz & Bryden 2015), leads to an immediate global-scale decrease in oxygen, as less O_2-rich water is pushed into O_2-depleted areas (Visbeck 2007; Schmidtko et al. 2017).

Although there are a number of mechanisms of subduction, and uncertainties remain about their relative importance (Morrison et al. 2022), on global scale O_2-subduction is shaped by: (i) lateral induction, defined as the transfer of fluid across a sloping winter mixed-layer base, and (ii) the wind-driven vertical Ekman velocity (Portela et al. 2020). Lateral induction is largest in well-defined locations in the North Atlantic and Southern Ocean, together contributing about two-thirds to global subduction. In contrast, vertical velocity causes weaker but homogeneous subductive regions in the subtropical gyres of each ocean basin (Portela et al. 2020). The opposite of subduction, obduction, transfers fluid and tracers from the permanent to the seasonal thermocline. Major obduction regions are the Southern Ocean, which accounts for almost half of global obduction, the subtropical-subpolar North Atlantic, and the equatorial strip (Portela et al. 2020). Obduction modifies the properties of the mixed layer, altering air-sea gas exchange and biogeochemical processes. For example, obduction promotes the transfer of nutrients into the mixed layer and euphotic zone, thereby enhancing biological production and subsequent respiration, but at the same time may upwell O_2-depleted waters, enhancing O_2 fluxes into the ocean.

Anthropogenic warming results in increased stratification and the decoupling of O_2-saturated surface waters from O_2-undersaturated subsurface waters. This may decrease ocean oxygenation as a result of reduced transport of O_2-rich waters into the permanent thermocline, but may moderate deoxygenation through reduced upwelling, reduced biological production, and reduced respiration (Bopp et al. 2001; Bopp et al. 2013). Similar but inverse mechanisms may operate in response to the predicted strengthening of the Pacific trade winds and Southern Ocean westerlies (Oschlies 2019). Further, changes in stratification may alter the mixed layer depth and the source depth of upwelling water masses, with increased stratification resulting in reduced source depths and reduced nutrient re-supply to the euphotic zone (Bograd et al. 2023). The change in nutrient re-supply mediated by this mechanism may be modified by the potential temperature-induced shifts in remineralisation profiles.

Subduction and interior transport can be separated into buoyancy-dominated and wind-stress-dominated components. The buoyancy-dominated circulation results from changes in air-sea heat and freshwater fluxes and the associated surface density

distribution. In the northern North Atlantic, strong surface buoyancy loss triggers open-ocean convection, generating North Atlantic Deep Water (NADW) that contributes to the lower branch of the upper cell of the Meridional Overturning Circulation (MOC). In mid-latitudes of the Southern Hemisphere (SH), deep mixed layers generate mode and intermediate waters which feed the upper branch of the MOC. In the Southern Ocean, coastal and offshore polynya convection are sources of significant sea-surface water-mass transformation, producing Antarctic Bottom Water (AABW) that feeds the lower overturning cell of the MOC and spreads into all ocean basins. Notably, the energy source for the MOC includes winds and tides that produce the turbulence needed for the diffusive upwelling across isopycnals that closes the overturning circulation.

The wind-stress-dominated circulation operates on much shorter timescales than the buoyancy-dominated circulation and is of prime importance for the ventilation of the thermocline (Oschlies 2019). Wind stress is the stress that the wind imposes on the ocean surface. It creates a vertically integrated ocean velocity, referred to as Ekman transport, perpendicular to the wind direction. Wind stress curl, caused by spatial gradients in wind stress, leads to mass convergence and divergence in the near-surface frictional layer, essential for large-scale gyre circulations (North et al. 2014). The internal flow, of prime importance for the general circulation of the upper ocean, is described by the Sverdrup balance and induces equatorward Sverdrup transport in subtropical gyres and poleward Sverdrup transport in subpolar gyres (Talley et al. 2011). In long zonal bands in the tropics, easterlies cause poleward divergence of surface waters, replenished by the upwelling of cold internal waters, while downwelling and subsequent equatorward transport at thermocline level is present throughout the subtropical regions (Talley et al. 2011). This motion is associated with the Subtropical-Tropical Cells, which connect the tropical upwelling regions with the subtropical subduction region in both hemispheres (Tuchen et al. 2019). Further, deep-water upwelling is caused by strong westerlies in the SH (Talley et al. 2011) and shapes the pattern and magnitude of the global MOC. While wind-stress-dominated circulation and buoyancy-dominated ventilation can be distinguished as such in theory, in the ocean these components interact.

Together, these mechanisms define the large-scale global patterns of ventilation and, in conjunction with remineralisation, the climatological mean state oxygen concentration: The Southern and North Atlantic Oceans are well-aerated and respired oxygen is rapidly replenished by physical processes. Conversely, in the eastern tropical regions, large eastern boundary upwelling systems are located above unventilated, quasi-stagnant shadow zones of the ventilated thermocline, giving rise to the Atlantic and Pacific Oceans oxygen minimum zones (OMZs). The remaining sluggish ventilation of such shadow zones is ascribed to meridional supply by lateral mixing, diapycnal oxygen fluxes from oxygen-rich layers above and below the OMZ, and zonal eastward advection of oxygen-rich waters from the well-ventilated western boundary (Brandt et al. 2015). As the zonal currents in the tropical Pacific and Atlantic are similar in strength, the difference in basin width between the two oceans results in comparatively older water masses and lower oxygen concentrations in the eastern tropical Pacific (Brandt et al. 2015). Any unbalanced oxygen consumption within these regions contributes to the observed long-term oxygen trend.

The Atlantic and Pacific OMZs differ considerably in shape and circulation patterns from the northern Indian Ocean OMZs. In the Indian Ocean, the presence of eastern boundary current upwelling systems is hindered by the geographical configuration (Rixen et al. 2020). Instead, there is a large monsoon-driven upwelling system in the western Arabian Sea off the Arabian Peninsula and a smaller one along the southwest coast of India during the Northern Hemisphere

(NH) summer. Important pathways of oxygen supply to the Arabian Sea OMZ are mesoscale eddies and filaments and the inflow of oxygen-rich water from the central Indian Ocean (Rixen et al. 2020). In the Bay of Bengal, the influx of oxygen-poor water from the Arabian Sea reduces the lateral oxygen supply, while anticyclonic eddies supply oxygen to the subsurface layer; cyclonic eddies in the Bay of Bengal instead inject nutrients into the euphotic zone, increasing productivity and oxygen consumption at depth (Rixen et al. 2020).

Non-steady-state changes in ocean ventilation may result from changes in buoyancy forcing and changes in wind stress patterns, and respond to both anthropogenic climate change and natural climate modes. Anthropogenic climate change mostly induces long-term trends in stratification and ventilation, with warming and freshening considered the major drivers of the observed long-term decline (Levin 2018; Cooley et al. 2022). Natural climate modes contribute to strong interannual to multidecadal variations in ventilation and superimpose regional long-term trends (Grégoire et al. 2019). Changes in ventilation, with indirect effects on all of the major controls of O_2 change, are estimated to be the dominant source of O_2 changes. However, the predominant control of O_2 concentration varies depending on water depth. In the upper $\sim$200 m of the water column and in the upper $\sim$1,000 m of the water column, changes are attributed in large part to a warming-induced decrease in solubility and to biological consumption, respectively (Schmidtko et al. 2017). However, remineralisation and the associated changes in consumption are assumed to decrease strongly with depth and changes in consumption are unlikely to be large below 1,000 m. Thus, integrated over the entire water column, ventilation is estimated to account for up to 85% of the observed oxygen loss, with an even larger contribution in the deeper ocean (Schmidtko et al. 2017).

Natural climate modes related to O_2 variability include the Pacific Decadal Oscillation (Duteil et al. 2018), North Pacific Gyre Oscillation (Di Lorenzo et al. 2008), and El Niño–Southern Oscillation (Espinoza-Morriberón et al. 2019) in the Pacific Ocean, the North Atlantic Oscillation (Frölicher et al. 2009), Atlantic Multidecadal Oscillation (Montes et al. 2016), and Atlantic Meridional Mode (Burmeister et al. 2019) in the Atlantic Ocean, and the Indian Ocean Dipole Mode (Vallivattathillam et al. 2017) in the Indian Ocean. Furthermore, volcanic eruptions superimpose the trends and natural climate modes, as they can have far-reaching impacts on temperature (Grégoire et al. 2019).

O_2 concentrations display a nuanced pattern in space and time, related both to anthropogenic climate change and natural climate fluctuations that exercise influence on O_2 through manifold means. However, our present understanding of the spatial distribution of O_2 changes and their causes is limited, in part as a result of sparse accessible observational data (Grégoire et al. 2021). Besides, the superposition of various forcings and mechanisms complicates the attribution of causes for O_2 distribution and change (Oschlies et al. 2018). Global ocean biogeochemical models (GOBMs), although limited in their abilities to reproduce temporal and spatial patterns of O_2 (Oschlies et al. 2017), permit the disaggregation and delineation of mechanisms that are superimposed in nature. As such, GOBMs can be used to deconstruct the mechanisms that force changes in oceanic O_2 inventories, as well as to gain a more detailed understanding of their functioning and contribution to O_2 inventory changes.

1.2 Rationale

The primary objective of this thesis is to investigate O_2 long-term changes and variability over the period 1958-2018, and attribute the spatial and temporal patterns in oxygen to the driving physical and biological processes. The relative contributions of solubility, respiration, and ventilation-induced changes to the

total O_2-interannual changes are estimated, as is the role of wind stress and buoyancy forcing in modulating these changes. The decomposition of oceanic O_2 trends into controls and regions will improve our mechanistic understanding of O_2 changes and, in turn, our ability to understand and predict future changes in O_2.

This thesis is structured as follows: After this introduction, the subsequent Section 2 details the methods used, including a description of the model used (Section 2.1), specifications of the simulations and analyses performed (Sections 2.2 and 2.3), and descriptions of the observational datasets, including any pre-processing steps, that were used for comparison against model results (Section 2.4). The body of the thesis is then organised into two main components. The first component is dedicated to the evaluation and discussion of model performance in terms of the climatological mean state of oxygen and the variables related to this state (Section 3). The second component comprises a detailed analysis of the non-steady-state changes of the oceanic oxygen content spanning the years 1958 to 2018 (Sections 4.1 and 4.2) and the factors contributing to the simulated oxygen trends and variability at global and regional scales (Section 4.3). This forms the central results section (4). The paper concludes with a discussion (5) and conclusions (6) section, which summarise the main findings and their implications in the context of existing knowledge, and identify future research needs.

Box 2 Section 1: Key takeaways

1. The global oceanic oxygen inventory has declined by more than 2% over the last 50 years (Schmidtko et al. 2017), impacting marine ecosystems and the cycling of a number of important elements.
2. Regional oxygen changes are more complex and vary by ocean basin and depth, implying different mechanisms responsible for O_2 changes in space and time (Stramma & Schmidtko 2021).
3. Fundamentally, oxygen enters the ocean through air-sea exchange and is lost mainly through the respiration of organic matter throughout the water column; in the absence of significant oxygen sources in the ocean interior, the oxygen supply to the deep ocean relies on physical ocean ventilation processes. [Section 1.1]
4. From these source-sink dynamics, three key pathways are identified that may underlie any oxygen change (Keeling et al. 2010; Oschlies 2019): (i) changes in initial oxygen concentrations in surface waters, mainly regulated by oxygen solubility, (ii) changes in biological consumption in the ocean interior, and (iii) changes in ocean ventilation; these interact in the ocean. [Section 1.1]
5. This study aims to analyse non-steady-state (see note hereunder) oxygen changes from 1958-2018 by means of a global ocean biogeochemical model, attributing oxygen trends and variability to their underlying causes, and additionally determining the contribution of wind stress and buoyancy forcing to the modulation of oxygen dynamics. [Section 1.2]

   Note: O_2 fluxes include steady-state and non-steady-state components, reflecting O_2 fluxes under constant climate conditions and O_2 fluxes related to anthropogenic climate change and natural climate variability, respectively.

2 Methods

2.1 Model description

A global configuration of the ocean-sea ice model NEMO version 3.6 (Madec & the NEMO team 2016) was used, with Louvain-la-Neuve sea Ice Model version 2 (LIM2) as the dynamic–thermodynamic sea ice model (Madec & the NEMO team 2016), coupled to the marine biogeochemical model MOPS (Kriest & Oschlies 2015); ORCA025-MOPS. ORCA025-MOPS has a 0.25° x 0.25° horizontal resolution on a tri-polar grid and 46 vertical levels, with vertical resolution decreasing with depth.

There is an increasing recognition of the significance of ocean mesoscale processes, such as currents, fronts, and eddies that occur on spatial scales of tens to hundreds of kilometres, in transporting and transforming biogeochemical tracers (McGillicuddy 2016). The spatial scale of processes that can be resolved by an ocean model is set by its horizontal resolution. A horizontal resolution of 0.25° x 0.25° is sufficient to resolve the mesoscale eddy field in most parts of the lower and mid-latitude regions where mesocale eddies are in the order of 100 kilometres. At high latitudes mesocale eddies can be as small as 10 kilometres and only the larger eddies can be explicitly resolved (Chelton et al. 2011; Hallberg 2013).

NEMO is coupled to the marine biogeochemical model MOPS (Kriest & Oschlies 2015; Chien et al. 2022), which simulates the lower trophic levels of the marine ecosystem and associated nutrient cycles using four chemical elements in nine compartments: phosphorus (P), nitrogen (N), O_2, phytoplankton (C, N, P), zooplankton (C, N, P), detritus (C, N, P), dissolved organic matter (C, N, P), dissolved inorganic carbon (C), and alkalinity. Phytoplankton growth depends on ambient phosphate (PO_4), nitrate (NO_3), temperature, and light. O_2 changes due to photosynthesis with a fixed stoichiometric ratio: $R_{-O_2:P}$ (i.e., mole oxygen released per mole phosphorus assimilated). Zooplankton grazing on phytoplankton is parameterised by the Holling-III function (Holling & Buckingham 1976). Zooplankton egestion and phytoplankton mortality produce sinking detritus, with sinking speed increasing linearly with depth, and neutrally buoyant dissolved organic matter. The remineralisation rate is constant and independent of temperature. In MOPS, remineralisation of organic substrates (i.e., detritus and dissolved organic matter) is dependent on ambient O_2 concentrations. Aerobic respiration requires a fixed amount of moles of oxygen to oxidise 1 mole of organic phosphorus, denoted by the ratio $R_{-O_2:P}$. If oxygen is below a certain threshold, organic matter is remineralised anaerobically (i.e., denitrification) under reduction of NO_3. A fraction of the organic detritus deposited on the seafloor is buried[2]. To compensate for the burial of organic matter (as PO_4 and associated elements) and mass budget closure, the amount of globally integrated PO_4 and associated elements lost to the sediment is homogeneously redistributed in the uppermost model layer of areas with river discharge. Nonburied detritus is resuspended into the water column. Air–sea gas exchange of O_2 is parameterised following the OMIP protocol (Orr et al. 2017), with air-sea gas transfer velocity and saturation computed from 3-hour mean wind speed, temperature, and salinity. For details about MOPS see Kriest & Oschlies (2015) and Chien et al. (2022).

2.2 Model simulations

ORCA025-MOPS was forced by the JRA55-do atmospheric data set (v.1.4) and runoff data sets (v1.1) from 1958 to 2018 (Tsujino et al. 2018), which delivers high-resolution forcing in both space (0.5° horizontal resolution) and time (3-hour resolution). The JRA55-do forcing fields are surface air temperature and specific humidity, zonal and meridional wind speed, ingoing shortwave radiation and outgoing

[2]In MOPS, there is no sediment module and detritus is buried in a hypothetical sediment.

longwave radiation, rain- and snowfall, and river and ice-related runoff. The forcing fields were used to calculate air-sea fluxes of momentum, heat, freshwater, and oxygen using bulk formulae. ORCA025-MOPS was initialised by a spin-up performed with the 0.5 resolution model ORCA05-MOPS. ORCA05-MOPS was initialised with Levitus 98 conditions (Levitus 1998) for temperature and salinity, with World Ocean Atlas 2013 conditions (Garcia et al. 2014b; Garcia et al. 2014a) for PO_4, NO_3, and O_2, and with GLODAPv.2 conditions (Lauvset et al. 2016) for alkalinity and C_{nat}. ORCA05-MOPS was run under three cycles of JRA-55do atmospheric forcing from 1958 to 2018, amounting to a total spin-up of 183 years. The end of the third cycle of ORCA05-MOPS provided the biogeochemical initial conditions for a spin-up with ORCA025-MOPS, run under one cycle of JRA-55do atmospheric forcing. For technical reasons, the physics had to be restarted from Levitus 98. The end of the fourth cycle in turn provided the initial conditions for the series of ORCA025-MOPS experiments analysed here.

Four experiments were performed: (i) a hindcast experiment (HIND) was performed under interannual forcing of JRA55-do (1958–2018) and (ii) a climatological experiment (CLIM) was performed, where the interannual variability of all atmospheric variables needed to force the ocean model was suppressed. This steady-state climate was obtained by repeating the JRA55-do forcing of a single year (1st May 1990 to 30th April 1991), most neutral in terms of major climate modes (Stewart et al. 2020). In addition, two sensitivity experiments were performed, aiming at isolating the effect of the interannual variability of wind stress and buoyancy forcing on oxygen inventories and controls. (iii) In the buoyancy forcing experiment (BUOY) the interannual variability of wind stress was suppressed, while the interannual variability of all variables needed to compute the air-sea fluxes of heat, freshwater, oxygen, and chlorofluorocarbon-12 (CFC-12) was maintained. (iv) In the wind stress experiment (WIND) the interannual variability of the variables needed to compute the air-sea fluxes of heat, freshwater, oxygen, and CFC-12 was suppressed, while the interannual variability of the wind stress needed to compute the air-sea momentum flux was preserved. The atmospheric variables to compute the air–sea fluxes of heat, freshwater, oxygen, and CFC-12 are wind speed, air temperature, air humidity, incoming solar radiation, outgoing longwave radiation, and precipitation. It is important to note that the experiments do not permit complete isolation of buoyancy forcing and wind stress effects, as changes in wind stress affect the patterns of sea surface temperature and thus the air-sea heat and freshwater fluxes. In a similar manner, buoyancy forcing may alter wind stress through changes in ocean circulation, as wind stress is controlled by the difference between wind speed and ocean current speed. However, the effect of ocean current speed on wind stress is minor and the effect of wind speed dominates.

Following a frequently used strategy (Gruber et al. 2023), this simulation series was used to differentiate between steady-state and non-steady-state components of the O_2 fluxes and inventories (Box 1). The steady-state fluxes (O_2^{ss}) are those that exist under the repeated-annual-cycle conditions simulated by the CLIM experiment. The non-steady-state fluxes (O_2^{ns}) are those which arise solely because of year-to-year atmospheric variability. To obtain an estimate of O_2^{ns}, the O_2 inventories in CLIM (i.e., O_2^{ss}) were gridpoint-wise removed from those in HIND (i.e., O_2^{ss} + O_2^{ns}), assuming the same steady state in CLIM and HIND (Patara et al. 2021). A schematic of the procedure is shown in Figure 1. HIND, of which CLIM has been subtracted, is hereafter referred to as $HIND_{ns}$. In addition, the role of interannual variability of wind stress and buoyancy forcing on O_2^{ns} was isolated by removing CLIM from the sensitivity experiments. BUOY and WIND, of which CLIM has been subtracted, are hereafter referred to as $BUOY_{ns}$

and $WIND_{ns}$, respectively.

An important and interesting question is to what extent the choice of different physical and biogeochemical parameterisations may influence the steady-state and non-steady-state components of O_2 dynamics. Therefore, a 3-member ensemble of HIND-CLIM twins (Table 2), differing in both biogeochemical parameters (stoichiometric O_2:P ratio) and physics (freshwater runoff), was used to estimate the uncertainty associated with different parameter choices. As shown in Figure A.1a, different biogeochemical parameters and physical boundary conditions produce different O_2^{ss} mean inventories and long-term trends (although the climatological distributions of oxygen are generally similar across runs 1-3 [Figure A.2]): Due to the limited spin-up time compared to deep ocean equilibration timescales and imperfect model parameterisation, O_2^{ss} was not fully equilibrated and a small drift is present throughout the simulations. The drifts in CLIM runs 1, 2, and 3 measured 0.28, 0.23, and -0.13 petamoles O_2 per decade, respectively. Considering the long-term climatological mean of each run, these rates translate to a change of approximately 0.12%, 0.09%, and -0.06% per decade for runs 1, 2, and 3, respectively. For comparison: Schmidtko et al. (2017) estimated an actual decrease in oceanic oxygen content over the last 50 years of 4.8 $\pm$ 2.1 petamoles, corresponding to about 0.96 $\pm$ 0.42 petamoles O_2 per decade.

Important in the context of this study is to assess whether the different O_2^{ss} also impact on the O_2^{ns}, obtained by subtracting CLIM from HIND for each ensemble member. As can be seen in Figure A.1b, $HIND_{ns}$ shows a similar progression of the global oxygen inventory in all three ensemble members throughout the simulation period; the long-term mean[3] measures about 186.672 teramoles O_2 with a standard deviation of approximately 4.17 teramoles

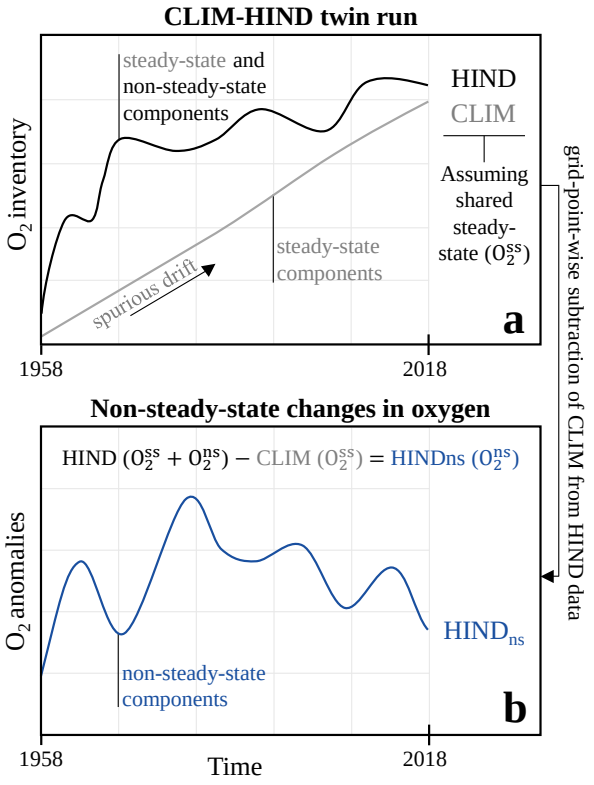

Figure 1: Schematic of the non-steady-state component extraction. **(a)** Scheme of oxygen temporal evolution in an ORCA025-MOPS CLIM (grey) and HIND (black) experiment. **(b)** O_2 inventory anomalies relative to CLIM, obtained by grid-point-wise subtraction of the O_2 inventory in CLIM from that in HIND. These anomalies, based on the assumption of a common steady-state between CLIM and HIND, capture the non-steady-state O_2 fluxes due solely to year-to-year atmospheric variability.

O_2. This consistency lends confidence that the projected trajectory of the oxygen inventory is insusceptible to major biases arising from the choice of biogeochemical or physical parameters. In addition, this consistency reinforces the assumption that the CLIM and HIND experiments of each ensemble member share a similar drift.

[3]Note that O_2^{ns} is not oscillating around zero as O_2^{ns+ss} is on global-average above O_2^{ss} in each run. The value of the offset depends on the choice of the specific year used to perform the CLIM experiment, and is not of particular interest in this context.

Table 2: List of experimens performed. Under Configuration (Config.), the same letters symbolise the same configuration of the biogeochemical parameters (BGC) or physical configuration (Physics). For BGC, a and b correspond to a $R_{\text{-}O_2:P}$ of 150 and 162, respectively. For Physics, a and b indicate different runoff fields.

Run	Config.		Experiment	Stored output			
	BGC	Physics		Oxygen	(O_2^{sat})	CFC-12	RR
1	a	a	CLIM	yes	no	no	no
			HIND	yes	no	no	no
2	a	b	CLIM	yes	yes	no	no
			HIND	yes	yes	yes	no
			WIND	yes	yes	yes	no
			BUOY	yes	yes	yes	no
3	b	b	CLIM	yes	no	yes	yes
			HIND	yes	no	yes	yes

Abbreviations: RR = remineralisation rate.

Note: (O_2^{sat}) here refers to the output used to calculate O_2^{sat}, namely potential temperature and salinity.

2.3 Analyses

For the analysis of underlying controls, changes in oceanic dissolved oxygen were separated into three components: (i) solubility-induced changes; (ii) respiration-induced changes; and (iii) ventilation-induced changes. O_2 solubility in seawater was approximated by O_2^{sat}, representing the O_2 concentration that a water mass can reach when in equilibrium with the O_2 partial pressure of the overlying atmosphere (Garcia & Gordon 1992). Respiratory O_2 consumption was approximated by respiration rate and was stored as model output. Changes in ventilation were assessed using the anthropogenic transient tracer CFC-12[4]. Atmospheric CFC-12 entered the ocean during spin-up, so that CFC-12 inventories in 1958 reflect observations. The same steady-state and non-steady-state separation approach was used for the explanatory variables. This permitted the use of $HIND_{ns}$ to assess the relative contributions of solubility, respiration, and ventilation-induced changes to the total O_2 interannual change, and the use of $BUOY_{ns}$, and $WIND_{ns}$ to assess the contributions of buoyancy forcing and wind stress to the solubility, respiration, and ventilation-induced O_2 interannual change.

The analyses performed fall into two key components: (Section 3) the assessment of the performance of ORCA025-MOPS, focusing on (Section 3.1) the climatological mean state of oxygen and (Section 3.2) variables related to the climatological mean state of oxygen, and (Section 4) - including the time dimension - the assessment of (Section 4.1) non-steady-state changes in O_2 from 1958-2018, along with (Section 4.3) the assessment of the causes underlying the simulated oxygen trends and variability. To this end, the following analyses were performed:

(Section 3.1) The assessment of model performance for the representation of the climatological mean state of oxygen encompassed the comparison of the oxygen concentration climatology in ORCA025-MOPS HIND against observations, as well as the juxtaposition of global vertical profiles of O_2 concentrations in $HIND_{ns}$ and observations.

(Section 3.2) Apart from oxygen, the climatological mean states simulated by ORCA025-MOPS HIND

[4] All experiments were forced by identical atmospheric CFC-12 concentrations.

were compared with observations for O_2^{sat}, Apparent Oxygen Utilisation (AOU), phytoplankton and zooplankton biomass, sea surface temperature, salinity, and mixed layer depth (MLD).

(Section 4.1) Incorporating the time dimension, annually-averaged O_2 inventory anomalies were integrated above 1,000 m depth (i.e., across the coinciding dimensions of model and observational datasets; see Section 2.4) and compared between $HIND_{ns}$ and observations. Ordinary least squares regression models were fitted to the time-series to quantify the magnitude of linear trends and their significance using the function `OLS` from the Python package `statsmodels`. In addition, the depth dimension was considered by horizontally integrating the annual global O_2 inventory anomaly data at each vertical level for both $HIND_{ns}$ and observations. Also, for higher spatial resolution, grid-point least squares regressions of annually-averaged O_2 inventory anomalies against time were fitted for both $HIND_{ns}$ model projections and observations using the `polyfit` function from the Python package `xarray`.

Note that any long-term linear trend in O_2 concentration is superimposed by some degree of variability. This variability can be separated by the time scales of its periodicity. To this end, low and high-pass-filter extraction was performed on the detrended[5], one-dimensional O_2 anomaly time-series of each gridpoint in both $HIND_{ns}$ and observations, as demonstrated in Figure A.3.

For low-pass filtering, the moving average was calculated. By averaging data points within a window of specified length (i.e., filter length), the output signal becomes smoother and high frequency components are attenuated - the frequency depending on the filter length. Here, the Hanning window, a taper formed by using a weighted cosine, was used as the window function and applied to the annual O_2 concentration anomaly time-series of each gridpoint in both $HIND_{ns}$ and observations. Filter length was set to 7. The low-pass filtered data is considered to capture the decadal variability. For high-pass filtering, the low-pass-filtered data was subtracted from the corresponding points in time of the original signal for the residual to capture the higher frequency components of the signal (i.e., components of periodicities higher than decadal; interannual variability).

The process of averaging by means of a sliding window inherently introduces data loss at the beginning and tail of the time-series. These edge effects occur because at the beginning and end of the time-series there is an insufficient number of data points to satisfy the window requirements of the moving average. Edge effects are addressed by signal reflection. Signal reflection involves adding a mirrored version of the signal to both ends of the original signal before applying the filter. This technique assumes the presence of periodic signals that continue with similar frequency and amplitude. Reflecting the start and end points of the original signal has been omitted to avoid repeating data points.

Standard deviations were calculated from the low and high-pass filtered data for each gridpoint and plotted in mmol O_2 m^{-3}. In addition, standard deviations were normalised relative to the simulated climatological mean oxygen concentration to account for spatial variations in the baseline oxygen levels and facilitate comparison across regions.

(Section 4.3) To assess the controls on oxygen trends and variability, global integrals were computed from annually-averaged O_2 inventory, remineralisation rate, CFC-12 inventory, and O_2^{sat} anomaly data in ORCA025-MOPS $HIND_{ns}$, $BUOY_{ns}$, and $WIND_{ns}$. Ordinary least squares regression models were fitted to the time-series to quantify the magnitude of the linear trends and their significance using the function `OLS` from the Python package `statsmodels`. In addition, the same variables were integrated across

[5]Linear trend estimated by `xarray`'s function `polyfit` removed from each grid point (see earlier).

Table 3: Specification of the boundaries of the areas subject to in-depth regional analysis of oxygen controls.

Region	Latitude	Longitude	Depth range
North Atlantic	40°N-70°N	70°W-10°W	<1,000 m and >1,000 m
Equatorial Pacific	15°S-15°N	110°W-70°W	<300 m and 300-1,000 m

defined geographical regions, namely the North Atlantic and the equatorial Pacific Ocean. The specific area boundaries are detailed in Table 3. Also, the global ocean heat content was computed by integrating the three dimensional product of annually-averaged potential temperature, seawater density, and specific heat capacity in ORCA025-MOPS HIND. Incorporating the depth dimension, global horizontal integrals were calculated for annually-averaged O_2 inventory anomalies and explanatory variables in $HIND_{ns}$, $BUOY_{ns}$, and $WIND_{ns}$. Finally, to estimate regional differences in the magnitude of the influence of solubility, respiration, and ventilation on oxygen, the Pearson correlation coefficient between oxygen anomalies and explanatory variables was calculated for each gridpoint along the time dimension using the function `corr` from the Python package `xarray`. Significance was tested by calculating the 2-tailed p-value associated with the Pearson correlation coefficient using the function `pearson_r_p_value` from the Python package `xskillscore`. Note that for the presentation of the CFC-12 inventory anomalies, as well as for the regression and correlation analyses, the yearly CFC-12 inventory anomalies were always converted to anomalies in percent relative to the CFC-12 inventory of the corresponding year as $HIND_{ns} \div CLIM \times 100$. This conversion was used to adjust for the increase in CFC-12 inventory over the period 1958 to 2018 and the inherently smaller absolute anomalies in CFC-12 inventory (HIND-CLIM) at the beginning of the simulation period.

As noted earlier, the analyses were based on three different model runs and a total of eight experiments (Table 2). For technical reasons, the output variables that were stored differ slightly across the model runs, resulting in different experiments being used across analyses (and corresponding figures). For all oxygen-only analyses and figures (Section 3.1: assessment of the performance of ORCA025-MOPS for oxygen climatology and Section 4.1: assessment of non-steady-state changes in O_2), the mean of all three runs has been used in all cases: the climatological mean O_2 spatial distribution was calculated as the mean of all available HIND runs, and the O_2 inventory anomalies and standard deviations were calculated from the mean of all CLIM-HIND-twin ($HIND_{ns}$) runs. In Section 3.2: assessment of climatological mean states for variables other than oxygen, Run 2 provided the outputs for sea surface temperature, AOU, salinity, MLD, and wind speed, while Run 3 provided the outputs for phytoplankton and zooplankton biomass. And finally, when comparisons or calculations were made with the main explanatory variables, or when the WIND or BUOY experiments were involved (Section 4.3: assessment of controls underlying oxygen trends and variability), Run 2 was used for oxygen, O_2^{sat}, CFC-12, and the calculation of the global ocean heat content, while the remineralisation rate output was drawn from Run 3. For CFC-12 the CLIM experiment from Run 3 was used. This should not affect the results as Runs 2 and 3 have the same physical configuration and differ only in the O_2:P ratio, which should not affect the non-reactive tracer CFC-12. Note that for the calculation of the correlation between oxygen and remineralisation rate, the oxygen output of Run 3 was used instead of Run 2.

2.4 Observational data sets

To assess the performance of the ORCA025-MOPS model, comparisons were made between model out-

puts and a range of observational data sets. Namely, observational climatological distributions of dissolved oxygen (Garcia et al. 2013; Garcia et al. 2019), sea surface temperature (Locarnini et al. 2019), salinity (Zweng et al. 2019), MLD (Holte et al. 2017), sea surface chlorophyll-a (Melin 2013), mesozooplankton (O'Brien & Moriarty 2012), and AOU (Garcia et al. 2019) were compared against the corresponding model outputs simulated by the ORCA025-MOPS hindcast simulations. The model geometry is based on a curvilinear grid, impeding a direct comparison against observations, most of which are available on regular rectangular grids. Therefore, for spatial distribution comparisons, model output was mapped onto a horizontal grid of 0.25° x 0.25° by bilinear interpolation. The vertical grid was retained. In addition, time-resolved observational data developed by Ito et al. (2017) and Sharp et al. (2022) were used to assess the accuracy of simulated oxygen trends and variability in $\mathrm{HIND_{ns}}$.

2.4.1 Oxygen, oxygen saturation concentration, and AOU

Spatial distribution comparisons of dissolved oxygen were made using the global dissolved oxygen climatology from the World Ocean Atlas 2018, which provides data at 1° x 1° spatial resolution interpolated on 102 depth levels (Garcia et al. 2019). For comparison against model results, the climatological oxygen field was interpolated onto the remapped ORCA025-MOPS grid. In addition, to assess the global vertical profile of oxygen, the dissolved oxygen climatologies from both the World Ocean Atlas 2018 and 2013 were used, latter employing the same grid as the World Ocean Atlas 2018 (Garcia et al. 2013). For comparison against simulations, model outputs were averaged over the full simulation period. This introduces a degree of uncertainty as the World Ocean Atlas 2013 and 2018 climatologies cover the periods 1955-2012 and 1955-2017 respectively, whereas ORCA025-MOPS outputs are provided between 1958 and 2018. For the assessment of trends and variability in dissolved oxygen inventories, gridded data products of observation-based oxygen concentrations, GOBAI-O_2 (Sharp et al. 2022a; Sharp et al. 2022b), and oxygen concentration anomalies developed by Ito et al. (2017), hereafter referred to as Ito-17, were used. GOBAI-O_2 covers the period 2004-2022 at a monthly resolution and is available at a spatial resolution of 1° x 1° (coverage: -179.5° to 179.5° longitude; -64.5° to 79.5° latitude) interpolated on 58 depth levels (coverage: 2.5 to 1975 dbar). Ito-17 covers the period 1950-2015 at an annual resolution and is available at a spatial resolution of 1° x 1° (coverage: -179.5° to 179.5° longitude; -89.5° to 89.5° latitude) interpolated on 47 depth levels (coverage: 0 -1,000 m depth). Due to relatively low sampling density in Ito-17 before 1960 and after 2010 (Ito et al. 2017), only data from 1960-2010 were used. Prior to comparison with simulations, GOBAI-O_2 was averaged to annual resolution and converted to oxygen anomalies by subtracting the long-term climatological mean. Both the model results and the observational data sets were then reduced to match horizontal and vertical coverage (-179.5° to 179.5° longitude; -89.5° to 89.5° latitude; 0-1,000 m depth) for direct comparisons.

For all observational data products, observed oxygen concentrations have been converted from µmol kg^{-1} to mmol m^{-3} using a fixed conversion factor of 1.024 (for approximate seawater density of 1024 kg m^{-3}) and from ml l^{-1} to mmol m^{-3} using a fixed conversion factor of 44.661.

In addition, from the model output O_2^{sat} was calculated from potential temperature and salinity (Garcia & Gordon 1992). AOU was then calculated as the difference between O_2^{sat} and O_2, as AOU = $O_2^{sat} - O_2$. The AOU for a parcel of water represents an approximation of the accumulated oxygen consumption since the parcel left the surface, assuming that O_2 was saturated at the time of the parcel's last contact with the atmosphere.

For the spatial distribution comparisons of AOU, the AOU (µmol kg^{-1}) climatology (1955–2017) provided by the the World Ocean Atlas 2018 was used, available at a spatial resolution of 1° x 1° interpolated on 102 depth levels (Garcia et al. 2019). AOU has been converted from µmol kg^{-1} to mmol m^{-3} using a fixed conversion factor of 1.024 (for approximate seawater density of 1024 kg m^{-3}). Observational O_2^{sat} was calculated as the sum of AOU (World Ocean Atlas 2018; Garcia et al. 2019) and measured dissolved O_2^{obs} (World Ocean Atlas 2018; Garcia et al. 2019), as O_2^{sat} = AOU + O_2. For comparison against model results, the climatological fields were interpolated onto the remapped ORCA025-MOPS grid and model outputs were averaged over the full simulation period.

2.4.2 Temperature and salinity

For the spatial distribution comparisons of temperature and salinity, temperature and salinity climatologies (1955-2017) from the World Ocean Atlas 2018 were used, available at 1° x 1° spatial resolution and interpolated on 102 depth levels (Locarnini et al. 2019; Zweng et al. 2019). For comparison against model results, the climatological fields were interpolated onto the remapped ORCA025-MOPS grid and model outputs were averaged over the full simulation period.

2.4.3 Mixed layer depth

To assess simulated MLDs, monthly climatology (2000-2021) MLD data (m) calculated from Argo profiles were used, available on a 1° x 1° grid (Holte et al. 2017). The climatology is calculated using a hybrid algorithm for the determination of MLDs described in Holte & Talley (2009). After averaging to annual mean MLDs, a total of 34,887 data points were obtained. For comparison against model results, the climatological field was interpolated onto the remapped ORCA025-MOPS grid and model results were averaged over 2000-2018. In the model, the MLD is defined as the ocean depth at which sigma-theta has increased by 0.01 kg m^{-3} relative to the near-surface value at 10 m depth.

2.4.4 Phytoplankton

For the assessment of simulated phytoplankton distribution, monthly climatology (2002-2017) sea surface chlorophyll-a data (mg Chl-a m^{-3}) available at 9 kilometre resolution derived from satellite remote sensing (MODIS-Aqua; Melin 2013) were used. After averaging to annual mean, chlorophyll-a was converted to carbon using the algorithm derived by Sathyendranath et al. (2009) and to phosphorus assuming a C:P ratio of 117 mol C : 1 mol P. For comparison against simulations, model outputs were averaged over 2002-2017.

2.4.5 Zooplankton

To assess the simulated zooplankton distribution, quasi-climatological (including data points between 1932-2010) mesozooplankton biomass data (MAREDAT; O'Brien & Moriarty 2012) were used, comprising 42,245 data points of monthly mean mesozooplankton biomass (µg C L^{-1}) on a 1° x 1° grid. After averaging to annual mean mesozooplankton biomass, a total of 23,533 data points were obtained for the upper 200 m. Carbon was converted to phosphorus assuming a C:P ratio of 117 mol C : 1 mol P. For comparison against simulations, model outputs were averaged over 1958-2010.

It should be noted that some zooplankton species perform diel vertical migrations, so that they are more abundant near the surface at night and in mid-water depths ($\sim$ 200-600 m) during the day (e.g., Bianchi et al. 2013; Bianchi & Mislan 2015). This process is not included in the model and may cause an overestimation of the simulated zooplankton biomass in the upper 200 m. Furthermore, the biogeochemical model does not differentiate between micro- and mesozooplankton, but aggregates both types into a single component. Due to sparse data for micro-

zooplankton biomass, and following the approach adopted by Chien et al. (2022), a fixed approximate micro-to-mesozooplankton ratio of one was assumed, thus doubling the observed concentrations of mesozooplankton biomass for comparison with model results.

Box 3 Section 2: Key takeaways

1. A global configuration of the ocean-sea ice model NEMO version 3.6 was used (Madec & the NEMO team 2016), coupled to the marine biogeochemical model MOPS (Kriest & Oschlies 2015), which simulates the lower trophic levels of the marine ecosystem and associated nutrient cycles. [Section 2.1]
2. Four experiments were performed to analyse oxygen dynamics [Section 2.2]:
   - 2.1 A hindcast experiment (HIND) was performed under interannual forcing (1958-2018) of JRA55-do (Tsujino et al. 2018).
   - 2.2 A climatological experiment (CLIM) was performed suppressing the interannual variability of all atmospheric variables needed to force the ocean model.
   - 2.3 Two sensitivity experiments were performed to isolate the effects of the interannual variability in wind stress (WIND) and buoyancy forcing (BUOY) on oxygen dynamics.
3. This study separates steady-state components of O_2 fluxes (i.e., those that exist under the suppression of interannual variability; O_2^{ss}) and non-steady-state components of O_2 fluxes (i.e., those that arise *solely* because of year-to-year atmospheric variability; O_2^{ns}). To obtain an estimate of O_2^{ns}, the oxygen inventories in CLIM were gridpoint-wise removed from those in the hindcast and sensitivity experiments, resulting in $HIND_{ns}$, $WIND_{ns}$, and $BUOY_{ns}$. [Box 1; Fig. 1; Section 2.2]
4. A 3-member ensemble of HIND-CLIM twins was used to investigate the influence of the choice of different physical and biogeochemical parameterisations on O_2^{ss} and O_2^{ns}. [Fig. A.1; Section 2.2; Table 2]
   - 4.1 Different biogeochemical parameters and physical boundary conditions led to different O_2^{ss} mean inventories and long-term trends, with a small drift present throughout the simulations.
   - 4.2 This study, however, focuses on O_2^{ns}, and despite different parameter choices, the global oxygen inventory in $HIND_{ns}$ followed a similar trajectory across all ensemble members, affirming robustness of the projected oxygen trends.
5. The non-steady-state oxygen changes in the hindcast ($HIND_{ns}$) and sensitivity experiments ($WIND_{ns}$ and $BUOY_{ns}$) were separated into solubility, respiration, and ventilation-induced components. Different variables, namely O_2^{sat}, remineralisation rate, and CFC-12 respectively, were used for the assessment of the contribution of each control to oxygen change. The same steady-state and non-steady-state separation approach was used for the explanatory variables. [Section 2.3]

3 Model Performance

3.1 Climatological mean state of oxygen

The climatology of oceanic O_2 concentration simulated by the ORCA025-MOPS hindcast ensemble (containing both steady and non-steady-state components) is evaluated using the observational data product World Ocean Atlas 2018 (Garcia et al. 2019). As shown in Figures 2 and 3, ORCA025-MOPS simulates a reasonable mean state compared to the World Ocean Atlas 2018. It reproduces the observed pattern of sea surface O_2 concentration, indicating lower oxygen levels in tropical areas gradually increasing towards the South and North Poles (Fig. 2a). This pattern arises because, in regions where surface waters can freely equilibrate with the O_2 partial pressure of the atmosphere, the prevailing O_2 concentration is highly correlated with O_2^{sat} (Fig. A.4), with waters close to or even slightly above the O_2 saturation concentration ($\mathrm{AOU} \approx 0$; Fig. A.5a). By this relationship, the O_2 concentration in the surface ocean is thus mainly determined by temperature and clearly follows the latitudinal temperature gradient (Fig. A.6a); salinity is of secondary importance. Although this relationship holds true in most regions of the Earth, deviations may occur in areas with seasonal or permanent ice cover or in regions where equilibration times are limited by rapid water transport processes (Fig. A.4).

In contrast to the broad agreement at the sea surface, discrepancies between simulated and observed O_2 concentrations become more pronounced in the subsurface and deep ocean (Fig. 4). In the ocean interior, the origin of the model bias is more complex, with contributions from both ocean circulation and the particulate organic carbon (POC) flux (Bao & Li 2016). While the observed globally averaged O_2 concentration reaches its well-simulated maximum at the sea surface due to air-sea gas exchange and marine primary production, the lowest O_2 concentrations are observed on average at about 1,000 m depth (Fig. 4). In the model ensemble, the simulated profile instead shows a shallower concentration minimum at about 500 m depth. This behaviour has been noted in other models (e.g., Bao & Li 2016) and may be attributed to a misrepresentation of remineralisation processes with overly high vertical attenuation of the POC flux. From a depth of 1,000 m, the O_2 concentration gradually increases with depth due to deep-water ventilation, both in the observations and in the model results. Overall, the model on average underestimates oxygen concentrations from the subsurface to a depth of about 1,500 m, while overestimating O_2 concentrations below that (Figs. 4 and 3d-f).

The vertical profile of oxygen concentration, however, varies greatly with geographical location (see e.g., Fig. 3a-c), with marked intermediate-depth low-oxygen zones developing wherever respiratory O_2 consumption exceeds physical replenishment. These OMZs are located at depths of approximately 100-1,500 m, typically along the eastern margins of the tropical and subtropical Atlantic and Pacific Oceans and in the northern Indian Ocean (Figs. 2b, 3a-c, and A.5b). At a depth of 300 m, transecting the largest OMZs, the model shows a tendency to underestimate O_2 levels in low and mid-latitudes. Conversely, the model overestimates O_2 levels at high latitudes, particularly in the Southern Ocean and Canada Basin (Fig. 2e). This bias in O_2 concentration also propagates to the model estimate of AOU at 300 m depth (Fig. A.5d).

Figure 3a shows a vertical section of O_2 concentrations at 20°W in the Atlantic Ocean. Over a broad spectrum of latitudes, O_2 concentrations decrease from the surface to a minimum at 300 to 1,000 m, and then increase to a maximum at about 2,000 m, caused by the formation of NADW and its southward propagation within the southward branch of the Atlantic Meridional Overturning Circulation (AMOC). Below, oxygen concentrations slightly decrease towards the seafloor. Analogously, Figure 3b and Figure 3c show

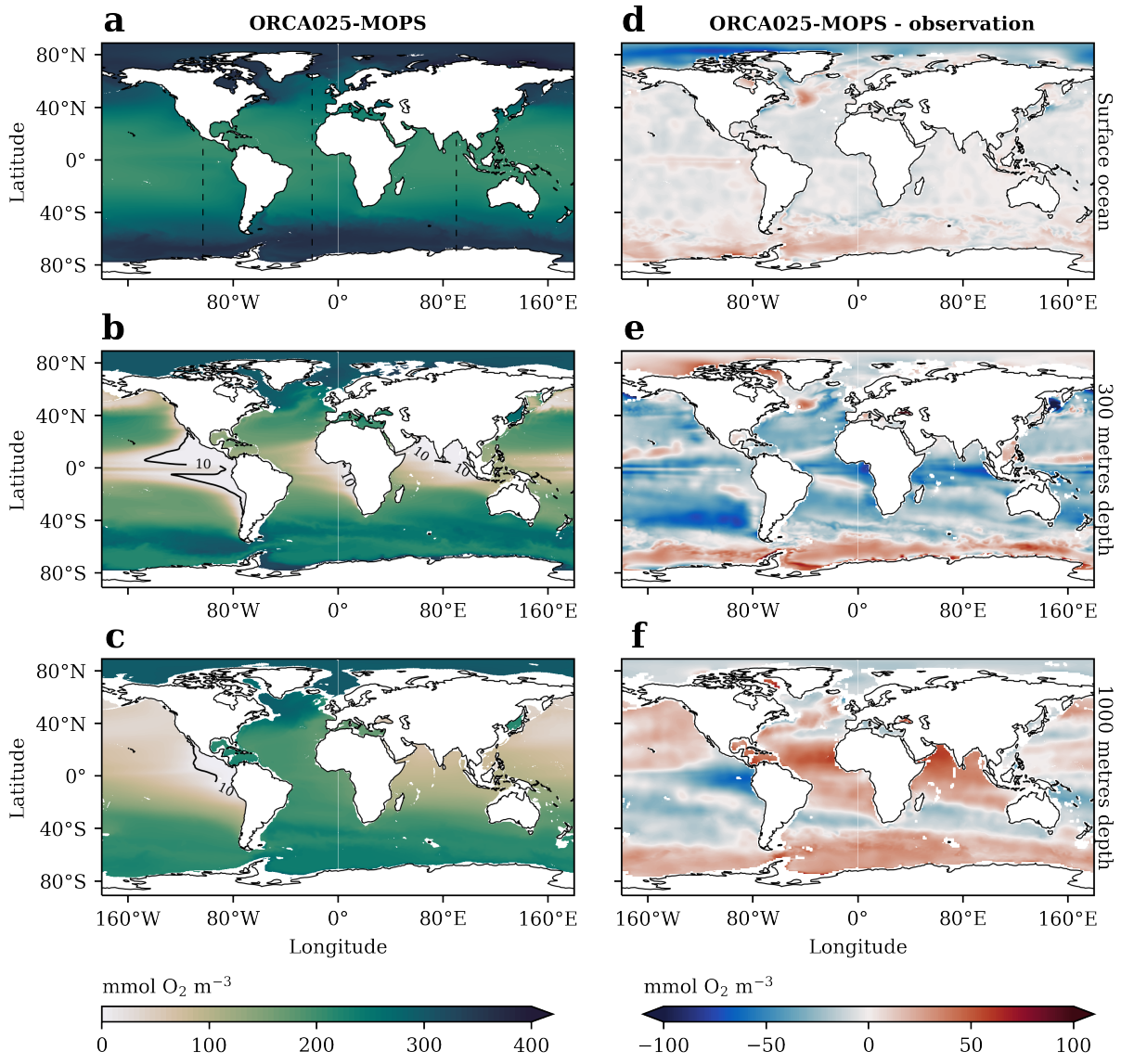

Figure 2: O_2 climatology from 1958-2018 in the ORCA025-MOPS hindcast simulations (ensemble mean) for **(a)** the surface ocean, and **(b)** at 300 m and **(c)** at 1,000 m depth. The corresponding differences between model and observations are shown in **(d)-(f)**, respectively. The observational data used are from the World Ocean Atlas 2018 (Garcia et al. 2019). For details of the observations, refer to Section 2.4. Contour lines in **(a)-(c)** correspond to an O_2 concentration of 10 mmol m^{-3}. The dashed lines in **(a)** indicate the sections shown in Figure 3 below.

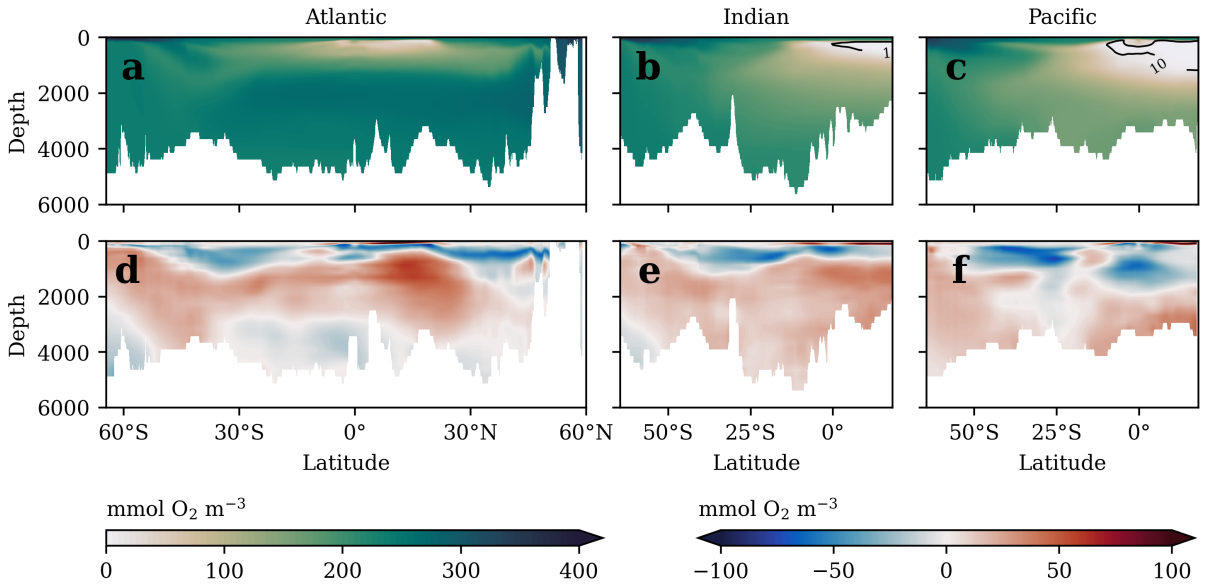

Figure 3: O_2 climatology from 1958-2018 in the ORCA025-MOPS hindcast simulations (ensemble mean) across the **(a)** Atlantic (20°W), **(b)** Indian (90°E), and **(c)** Pacific (103°W) Oceans. The corresponding differences between model and observations are shown in **(d)-(f)**, respectively. The observational data used are from the World Ocean Atlas 2018 (Garcia et al. 2019). For details of the observations, refer to Section 2.4. Contour lines in **(a)-(c)** correspond to an O_2 concentration of 10 mmol m^{-3}.

vertical sections of dissolved oxygen in the Indian Ocean at 90°E and the Pacific Ocean at 103°W, respectively. As there is no deep water formation in either basin to supply oxygen to deeper layers, O_2 concentrations generally decrease from the surface, reach a minimum at about 300-1,500 m depth and then increase towards the bottom. Although the general characteristics are reproduced by the model, there are some discrepancies as compared against observations: In the Pacific, the tropical hypoxia reaches overly deep in the water column. At depths below 1,000 and 2,000 m in the Indian and Pacific Oceans, respectively, there is a positive O_2 bias (Fig. 3e-f), likely due to imperfect physics and remineralisation settings. In the Southern Ocean, the subsurface has higher oxygen concentrations due to the presence of Antarctic Intermediate Water (AAIW), which is evident in the Atlantic (Fig. 3a) and Indo-Pacific sections of the model (Fig. 3b-c) and appears to be underestimated by the model (Fig. 3d-f). Along the Antarctic continent, oxygen-rich water flows downwards and northwards as a result of the formation of AABW.

3.2 Climatological mean state of controls

In the following, potential causes for the O_2 biases are inspected, with emphasis on the representation of factors influencing O_2 concentrations. The factors under consideration are: (i) oxygen saturation concentration at the surface; (ii) remineralisation; and (iii) ventilation.

3.2.1 Oxygen saturation concentration

In the surface ocean, the prevailing O_2 concentration is largely dependent on O_2^{sat}, such that the O_2 concentration in the surface ocean is primarily determined by temperature and secondarily by salinity. In ORCA025-MOPS, the climatological sea surface

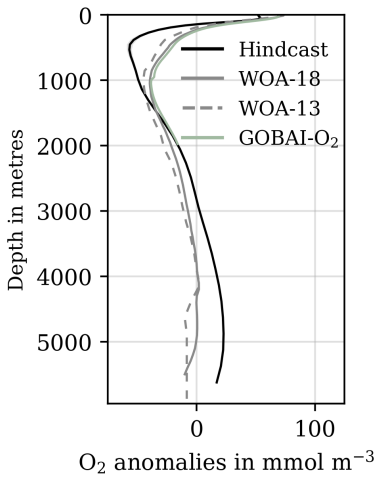

Figure 4: Global vertical profile of O_2 simulated by ORCA025-MOPS (black; ensemble mean) with standard deviations indicated by grey shading, and O_2 observational data from the World Ocean Atlas 2013 (dashed grey; Garcia et al. 2013) and 2018 (solid grey; Garcia et al. 2019), and the GOBAI-O_2 data product (green; Sharp et al. 2022a). For details of the observations, refer to Section 2.4. All data are mean centred.

temperature agrees well with the observational estimates, albeit with a tendency towards a cold bias at low and mid-latitudes and a warm bias at high latitudes (Fig. A.6a-b). Further, there is a substantial warm bias off the eastern North American coast and a cold bias to the east in the central subpolar region, attributable to the Gulf Stream separation being too far north and the North Atlantic Current being too zonal, respectively (Moreno-Chamarro et al. 2022).

While the misrepresentation of the northward turn of the Gulf Stream is also reflected in the salinity distribution, the bias in sea surface salinity falls mostly (∼73%) below ±0.5 psu (Fig. A.6c-d). A notable exception is the Arctic Ocean, specifically the Canada Basin, where the model simulates a surface layer that is >2 psu saltier than observed in places. This is a widespread bias in state-of-the-art ice-ocean models and may be due to unrealistically deep vertical mixing in the model in recent years (Ilıcak et al. 2016; Rosenblum et al. 2021).

The mismatches in temperature and salinity transfer directly to the model estimates of sea surface O_2^{sat}, with close agreement in low and mid-latitudes, overestimates in the Southern Ocean and northern Atlantic mostly due to the temperature bias, and underestimates in the Arctic Ocean due to the strong salinity bias (Fig. A.6e-f). These biases also align with the mismatches in simulated sea surface O_2 concentrations (Fig. 2d), which are of special interest as they determine the initial O_2 concentrations prior to transport into the ocean interior. It is worth noting that while regions with high O_2 concentrations might exhibit a high absolute bias, the corresponding relative bias (i.e., relative to the prevailing climatological mean oxygen concentration) might be low.

3.2.2 Controls of remineralisation

Remineralisation and its representation in the model is inherently dependent on the representation of phytoplankton biomass (see Section 1.1), limited in most ocean regions by the availability of inorganic forms of nitrogen, phosphorus, iron, and silica (Bristow et al. 2017; Browning & Moore 2023). Specifically, ∼75% of the ocean is limited by the availability of inorganic nitrogen (Bristow et al. 2017), while in high-nutrient, low-chlorophyll areas (i.e., areas where chlorophyll remains low despite plentiful supply of macronutrients) other factors such as grazing pressure, low irradiance, or silica or iron limitation contribute to persistently low chlorophyll levels (Basterretxea et al. 2022). As a result of the ubiquitous limitation of phytoplankton growth by nutrient availability, the climatology of chlorophyll-a concentration clearly maps the global distribution of nutrients and largely reflects the large-scale patterns of wind-driven vertical nutrient transport (Siegel et al. 2013). Particularly prominent regions of low chlorophyll-a are found in the subtropical gyres, where Ekman transport forces waters to downwell, while regions of deep seasonal mixing (e.g., at high latitudes; Fig. A.7) or persistent

upwelling (e.g., along the equator, in the Arabian Sea, or in the eastern tropics) show elevated chlorophyll-a levels (Fig. A.8b).

In ORCA025-MOPS, the distribution of phytoplankton in the surface layer (∼6 m) matches the observational estimates[6] reasonably well (Fig. A.8a-b). The strongest mismatches are found in the coastal regions, where the observed phytoplankton concentrations commonly exceed the modelled concentrations and may be related to simplifications in the representation of terrestrial nutrient runoff (e.g., the absence of additional nutrient runoff from anthropogenic sources) in the model (see Section 2.1). In addition, these mismatches may originate from the conversion of chlorophyll-a to phosphate, for example by assuming a fixed C:P ratio (see Section 2.4). This assumption fails to take into account the considerable (and non-random) variability in phytoplankton stoichiometry on a global scale, for example resulting from its dependence on nutrient availability (Martiny et al. 2013) or temperature (Garcia et al. 2018). In contrast, in the pelagic ocean, modelled phytoplankton biomass is generally higher than the observations, which, as noted by Chien et al. (2022), may be due to the lack of iron limitation in the model, for example in the eastern equatorial Pacific or Southern Ocean, where iron is a limiting nutrient (Bristow et al. 2017; Basterretxea et al. 2022; Browning et al. 2023).

The biomass of zooplankton is generally closely tied to the presence of phytoplankton through trophic interactions (Fig. A.8c). In addition, they provide organic carbon that is supplied as substrate to the process of remineralisation. And because the rate of remineralisation is largely substrate limited, also the spatial distribution of remineralisation is closely linked to that of phytoplankton and zooplankton (Fig. A.9a). While zooplankton is less homogeneously distributed than phytoplankton, differences from observational estimates are spatially similar: both modelled zooplankton and phytoplankton are overestimated around the equator and in the Southern Ocean at 40°S, although the sparse data on zooplankton biomass complicates a robust reading (Fig. A.8d).

Particularly in the Pacific, the overestimation of phytoplankton biomass in equatorial regions, likely to result in a too high particle export from the euphotic layer (Fig. A.8), may be responsible for the overly deep tropical hypoxia seen in Figure 3c. Other potential causes include insufficient equatorial ventilation in the upper ocean and insufficient remineralisation in the upper ocean; or their combined effects (Cabré et al. 2015; Bao & Li 2016). Insufficient remineralisation in the upper ocean may be due to the neglect of temperature sensitivity of remineralisation processes in the model, and an implicit underestimation of the higher vertical attenuation of POC flux in equatorial high-temperature regimes (Marsay et al. 2015). However, it should be noted that the globally averaged vertical profile of oxygen concentrations has a lower than observed minimum, suggesting an overestimation of the POC flux vertical attenuation on a global scale. This bias is independent of the parameter chosen for the oxygen-to-phosphorus ratio (Fig. A.10).

3.2.3 Ocean ventilation

While the remineralisation rate closely follows chlorophyll-a concentration and is higher in regions with deep seasonal mixing or persistent upwelling (Fig. A.9a), effectively, OMZs are shaped by ocean circulation, constituting the second key control of interior oxygen concentrations (Brandt et al. 2015).

The biases in interior O_2 concentration, featuring an underestimation in mode and intermediate water masses, an overestimation in deep water masses, and an underestimation in bottom waters (especially in the Atlantic Basin), are indicative of biases in

[6] Observational phytoplankton biomass was estimated from chlorophyll-a satellite data and converted to carbon using an algorithm derived by Sathyendranath et al. 2009 and to phosphorus assuming a fixed C:P ratio.

ocean circulation. The positive bias in deep waters, dominated by NADW formed by convection in the North Atlantic Basin, is consistent with an overestimation of the ventilation of these water masses. The main processes affecting the ventilation are the depth of the winter mixed layer and the transport out of the mixed layer, connected to the MOC. At about 13 Sv, the AMOC transport at 26°N is not overestimated with respect to the RAPID observational array (Rayner et al. 2011). The inspection of the MLD biases compared to the ARGO observations indicates that the model ensemble significantly overestimates the MLD at subpolar latitudes of the North Atlantic. It can be hypothesised that these overestimated and poleward shifted MLDs may increase the injection of O_2 into the deep ocean and shift its distribution towards denser and deeper varieties of NADW. It should be noted, however, that MLDs are computed differently between the model and observations, using a threshold method and a hybrid algorithm, respectively (see Section 2.4). In Holte et al. (2017), MLDs computed by the hybrid algorithm were generally shallower than those computed by the threshold method, especially in regions with deep winter mixed layers. Thus, the bias in MLDs shown in Figure A.7c may also be partly due to the different methods employed to determine MLDs.

As shown in Figure 3, the Southern Ocean is characterised by overestimated O_2 concentrations in deep water masses and underestimated concentrations in intermediate water masses. Possible explanations for these biases are: (i) the positive O_2 anomaly in NADW propagates into the Southern Ocean and is upwelled at the subpolar divergence and (ii) the upper cell of the MOC is too sluggish compared to reality. As O_2 decreases with depth, this would result in overestimates in subpolar upwelling regions and underestimates in recently ventilated and intermediate waters. Conversely, the MLD is generally overestimated, especially in the southeast Pacific, and thus cannot explain the underestimated O_2 concentrations along the AAIW path.

Box 4 Section 3: Key takeaways

1. The surface ocean is well-simulated due to well-simulated O_2^{sat} (i.e., temperature and salinity). Exceptions are overestimates in the Southern Ocean and North Atlantic, and underestimates in the Arctic Ocean, possibly due to upwelling of unrealistically oxygen-rich deep waters, errors in the representation of Gulf Stream dynamics, and too deep vertical mixing resulting in overly high Arctic Ocean surface salinity, respectively. [Sections 3.1 and 3.2.1]
2. The simulated O_2 concentration minimum in the globally averaged vertical O_2 profile is shallower than observed and may result from unrealistically high vertical attenuation of the POC flux [Sections 3.1 and 3.2.2].
3. Generally, in the ocean interior, simulated O_2 is underestimated in mode and intermediate water masses, overestimated in deep water masses, and underestimated in the bottom waters of the Atlantic Basin, further indicating misrepresentations in ocean circulation [Sections 3.1 and 3.2.3].
    - 3.1 The negative bias in intermediate waters, especially in the Southern Ocean, may be due to an overly sluggish upper cell of the MOC.
    - 3.2 The positive bias in deep waters, dominated by NADW, may be due to misrepresented MLDs in the North Atlantic, increasing the injection of O_2 into the deep ocean. This bias may also propagate into the Southern Ocean.
4. In the Pacific Ocean, the tropical hypoxia reaches overly deep in the model. This may be due to overestimated phytoplankton biomass in the equatorial Pacific and an overly high POC flux, insufficient equatorial ventilation, insufficient upper ocean remineralisation, or their combination. [Sections 3.1, 3.2.2, and 3.2.3]

4 Results

4.1 Oxygen inventory from 1958-2018

4.1.1 Globally integrated oxygen change

The global trend in oceanic oxygen inventory from 1958 to 2018 simulated by the ORCA025-MOPS ensemble is shown in Figure 5 and evaluated by comparing the simulated trend with the observational data products Ito-17 and GOBAI-O_2 which are available only for the upper 1,000 m (Fig. 6). Global changes in oxygen concentrations in ORCA025-MOPS and observations are summarised in Table 4.

The simulated global oceanic oxygen inventory from 1958 to 2018 shows four clearly discernible periods (Fig. 5; Table 4): In the first period (i), from 1958 to 1967, the O_2 inventory increases at a rate of about 218.69 $\pm$ 33.9 teramoles per decade (corresponding to an 0.09% increase), while Period ii, from 1967 to 1994, is characterised by a gradual decrease of about -46.6 $\pm$ 4.53 teramoles per decade (corresponding to a 0.02% decrease). From 1994 to 2002 (Period iii), the simulated trend in O_2 inventory departs from the long-term expected trend: an anomalous decline until 1998 is followed by a rapid recovery. From 2002 to the end of the simulation period (Period iv), the global oceanic oxygen inventory decreases continuously at an accelerated rate of approximately -108.61 $\pm$ 7.60 teramoles per decade (corresponding to a 0.05% decrease) as compared to Period ii.

From the surface ocean to 1,000 m depth, the model ensemble is in general agreement with Ito-17 during Periods i to iii. However, a significant discrepancy arises in Period iv. During this period, Ito-17 indicates a substantial decrease in the global oxygen inventory, strongly exceeding the rate simulated during Period ii (Fig. 6). This observation is corroborated by the GOBAI-O_2 data product, which shows a similarly sharp decrease during this period (Fig. 6; Table 4). In contrast, the model simulates a nearly stagnant global oceanic oxygen inventory for the

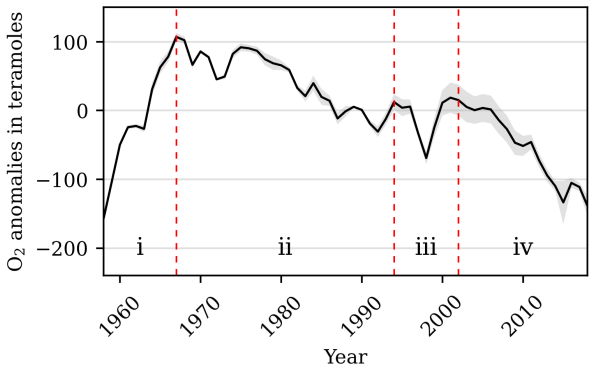

Figure 5: Annual time series of globally integrated O_2^{ns} (the non-steady component of O_2 fluxes, as described in Section 2.2) in the ORCA025-MOPS ensemble with one standard deviation over the 3-member ensemble indicated by grey shading. Red dashed lines and labels (i-iv) mark the four different periods of O_2 content evolution as described in Section 4.1.1. Data are integrated until the ocean bottom (differently with respect to Fig. 6) and shown as anomalies with respect to the 1958-2018 mean.

upper 1,000 m after 2002 (Fig. 6; Table 4). This underestimation is common across climate models and may be attributed to a spectrum of factors, including deficiencies in the representation of transport processes (e.g., due to inadequate model resolution), or the misrepresentation or neglect of critical biogeochemical mechanisms, as highlighted in Oschlies et al. (2018).

Although both model and observations indicate a decrease in oxygen content over the study period that extends throughout the upper 1,000 m of the water column, the rate of change is not uniformly distributed across the depth profile (Fig. 7). Specifically, the model simulates a maximum rate of change at about 50-200 m depth and a minimum rate of change at about 750 m depth (Fig. 7c). Ito-17 shows the largest absolute losses in the main thermocline at 100-300 m depth, in agreement with the estimates in Schmidtko et al. (2017), which is slightly deeper than modelled by ORCA025-MOPS. It should be noted that while the minimum at about 750 m agrees with

Ito-17, Schmidtko et al. (2017) found a minimum oxygen decline slightly higher in the water column at intermediate depths of 400-700 m. In summary, the rate of change simulated by the model is similar to that observed for the upper ∼200 m (∼1 mmol m^{-1} yr^{-1}), whereas the largest discrepancy between the model and the Ito-17 data set is found in the 200-500 m depth range, where the model largely underestimates the oxygen decline (Fig. 7c).

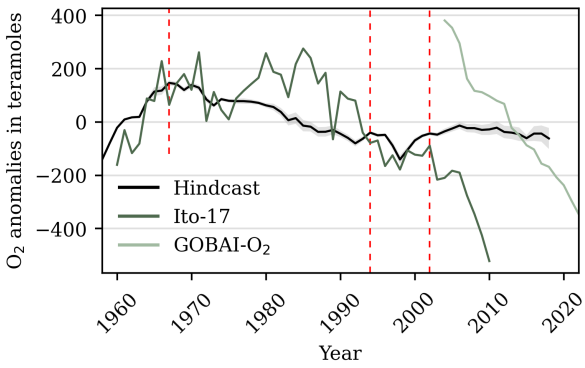

Figure 6: Annual time series of upper 1000 m O_2 inventory anomalies simulated by ORCA025-MOPS (black; ensemble mean) with one standard deviation indicated by grey shading, Ito-17 (dark green; Ito et al. 2017), and GOBAI-O_2 (light green; Sharp et al. 2022a). For details of the observations, refer to Section 2.4. Red dashed lines mark the four different periods of O_2 content evolution as described in Section 4.1.1. Please note that all data are mean centred. For mean-centering, the long-term mean calculated for the full time span of each dataset was used.

4.1.2 Regional patterns in oxygen trends

The regional structure of O_2 trends over Periods i, ii and, iv is inspected for different depth ranges in both model and observations (Figs. A.11, A.12, and A.13). Despite a high degree of patchiness, especially for the Ito-17 product, some general patterns can be discerned.

Period i: In both the model and observational data, most ocean regions are responsible for the global O_2 increase in 1960-1967 (Fig. A.11). Specifically, in the model, the equatorial Pacific, the western Indian Ocean, as well as the south-eastern Pacific are the major contributors to the rise in the oxygen inventory. However, there are also regional decreases in O_2 concentrations. Particularly noteworthy is the North Atlantic Ocean, a region central to deep water formation, where oxygen concentrations decrease throughout the water column, especially at the southern tip of Greenland. In the nearby Iceland Basin, however, oxygen concentrations increase significantly at mid-depth (Fig. A.11a-b). This mid-depth pattern is also found in the observational data (Fig. A.11e).

Period ii: From 1967-1994, the changes become more subtle (Fig. A.12; note the different colour scales in Figs. A.11 and A.12). At the southern tip of Greenland, oxygen concentrations increase throughout the depth profile; an increase that is effectively encircled by regions of decreasing oxygen concentrations (Fig. A.12a-c). This structure is similarly observed in Ito-17, although here the regions of decrease are more concentrated (Fig. A.12d-e). Strong trends are also observed in the equatorial Pacific, where opposing trends lie very close together in both modelled estimates and observations.

Period iv: The period from the early 2000s to 2018 is of particular interest, as this is the period in which the trends in the model and observations are most divergent. From Figure A.13 it is clear that the model is unable to reproduce the strong negative trends observed across several oceanic regions, including the North Pacific Ocean, the tropical Atlantic and Pacific Oceans, and the Southern Ocean. In contrast, the model is able to reproduce the increasing trend observed in the convection regions of the North Atlantic, extending from the surface to a depth of 1,000 m. Below this layer, there is a decrease in oxygen concentrations in the North Atlantic; the only site to show a clear trend in oxygen concentrations at this depth.

Table 4: Ocean volume in m^3, oxygen inventory (Inv.) in petamoles per decade, oxygen inventory change in teramoles per decade and percentage of inventory per decade over the Periods i, ii, and, iv described in Section 4.1.1.

Data	Volume (m^3)	Inv. (Pmol)	Oxygen inventory change	
			Tmol dec^{-1}	percent dec^{-1}
Period i (1960-1967)				
Model: full column	1.334×10^{18}	243.73	218.69 $\pm$ 33.9	0.09 $\pm$ 0.013
Model: 0-1,000 m	3.395×10^{17}	53.17	245.58 $\pm$ 30.76	0.462 $\pm$ 0.058
Observations: Ito-17	4.723×10^{17}	(53.17)	568.12 $\pm$ 127.44	1.068 $\pm$ 0.24
Period ii (1967-1994)				
Model: full column	1.334×10^{18}	243.86	-46.6 $\pm$ 4.53	-0.019 $\pm$ 0.002
Model: 0-1,000 m	3.395×10^{17}	53.32	-85.12 $\pm$ 3.86	-0.16 $\pm$ 0.007
Observations: Ito-17	4.723×10^{17}	(53.32)	-8.84 $\pm$ 22.26	-0.017 $\pm$ 0.041
Period iv (2002-2018)				
Model: full column	1.334×10^{18}	243.81	-108.61 $\pm$ 7.60	-0.045 $\pm$ 0.003
Model: 0-1,000 m	3.395×10^{17}	53.21	-24.95 $\pm$ 5.37	-0.047 $\pm$ 0.01
Observations: GOBAI-O_2	4.944×10^{17}	52.1	-381.83 $\pm$ 22.47	-0.733 $\pm$ 0.043

Note: (1) The inventory used to derive the percentage change for Ito-17 is from the model estimate, as Ito-17 is anomaly data. (2) Each inventory is calculated as an average over the period in question. (3) The results for the observational data can be compared with the model results for the upper 1,000 m as they share the same horizontal and vertical extent (see section 2.4). For details on the linear regression results see Table A.1.

Across all time periods, the North Atlantic and the equatorial Pacific consistently emerge as highly dynamic areas with strong trends, and thus demand a more extensive analysis. This in-depth analysis is revisited in Section 4.3.3, where the changes and contributing factors are comprehensively described for the North Atlantic and equatorial Pacific Oceans.

4.2 Interannual and decadal variability

The prevailing long-term trends are superimposed by strong interannual and decadal variability in O_2 inventories; the magnitude, time scale, and phase of which considerably varying across ocean regions and are clearly dependent on water depth. This can be seen, for example, when considering O_2 trajectories for different sub-regions and depth ranges (see in the Appendix A, Figs. A.23 [black lines] to A.25 [black lines]). To get a more integrated picture of which regions are characterised by the strongest interannual and decadal variability, fluctuations were separated according to the time scales of their periodicity[7], as described in Section 2.3.

The highest levels of O_2 interannual and decadal variability are manifested in strongly dynamic regions of water mass formation, frontal dynamics, and ocean-sea ice interaction (Fig. 8a-b). Instead, there is little variability in the centre of the subtropical gyres and in the Weddell and Ross gyres. Further, variability is low within the OMZs due to their inherently low oxygen concentrations. Decadal variability is typically higher in magnitude and, especially in the South Pacific, penetrates more deeply into the water col-

[7]To isolate the decadal variability, the data were smoothed using a Hanning window (filter length = 7). To isolate the interannual variability, the smoothed data were subtracted from the original signal.

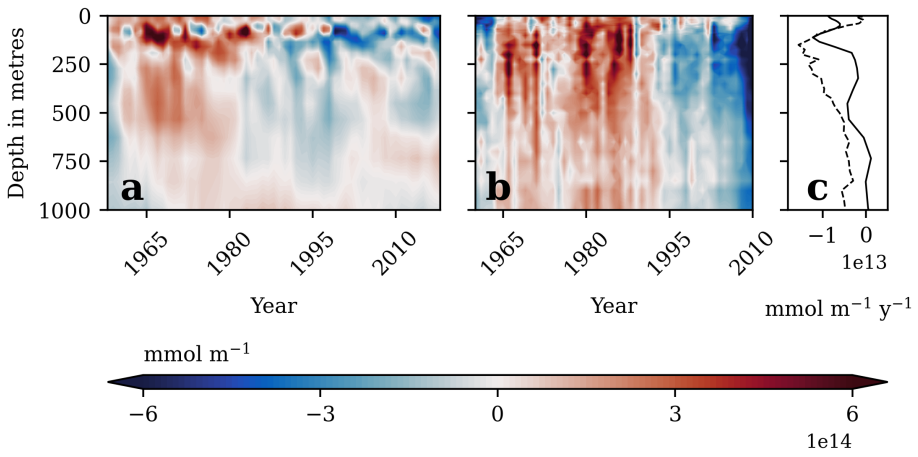

Figure 7: Hovmöller diagrams of oxygen concentration anomalies from 0-1,000 m depth in **(a)** $HIND_{ns}$ (ensemble mean) and **(b)** Ito-17 (Ito et al. 2017). The data are mean-centred for each vertical level, using the 1958-2018 mean for the model results and the 1960-2010 mean for the Ito-17 data product as references. Linear trends in oxygen concentrations (in mmol m^{-1} y^{-1}) for each vertical level, estimated over the full period of the respective data set, are shown in **(c)**. For details of the observations, refer to Section 2.4.

umn than interannual variability (Figs. 8e and 8h). An exception is the northern Atlantic, where substantial variability on both interannual and decadal timescales reaches considerable depths (Figs. 8c and 8f). This is related to the process of deep water mass formation, which efficiently transports surface signals of interannual and decadal variability to great depths. Although the patterns of interannual and decadal variability generally align, certain deviations are discernible. Decadal variability is considerably higher than interannual variability in specific areas (compare Figs. 8a and 8b), including the equatorial Atlantic, the region of deep wintertime mixed layers north of the Antarctic Circumpolar Current in the southeast Pacific Ocean from 160°W to the Drake Passage, and the Labrador Sea, the latter indicating pronounced decadal variability of deep water formation processes in this area.

The separation between interannual and decadal variability was also performed for the Ito-17 data product. Both model and observations share a consistent pattern of increased variability in highly dynamic regions (compare Figs. 8 and A.14). Some discrepancies exist, however. (1) The observational data show higher variability encircling the Antarctic continent (where AABW is formed) compared to the model, especially on decadal time scales; (2) the observations do not show the area of heightened variability in the southeast Pacific associated with deep mixed layers north of the Antarctic Circumpolar Current; (3) the model shows substantially higher decadal variability in the North Atlantic than the Ito-17 data product. Some of these biases might be related to the non-uniform spatial coverage of the observations, which are notoriously sparse in the SH.

As noted above, the standard deviations within OMZs are low due to their inherently low mean oxygen concentrations. Considering the standard deviation relative to the mean oxygen concentration, a different pattern emerges (Fig. A.15): The edges of the OMZs show substantial variability on both interannual and decadal time scales, forming a band of increased variability that delineates the cores of the prevailing OMZs (approximately following the 10 mmol m^{-3} climatological mean concentration of oxygen) and indicates considerable variation in the

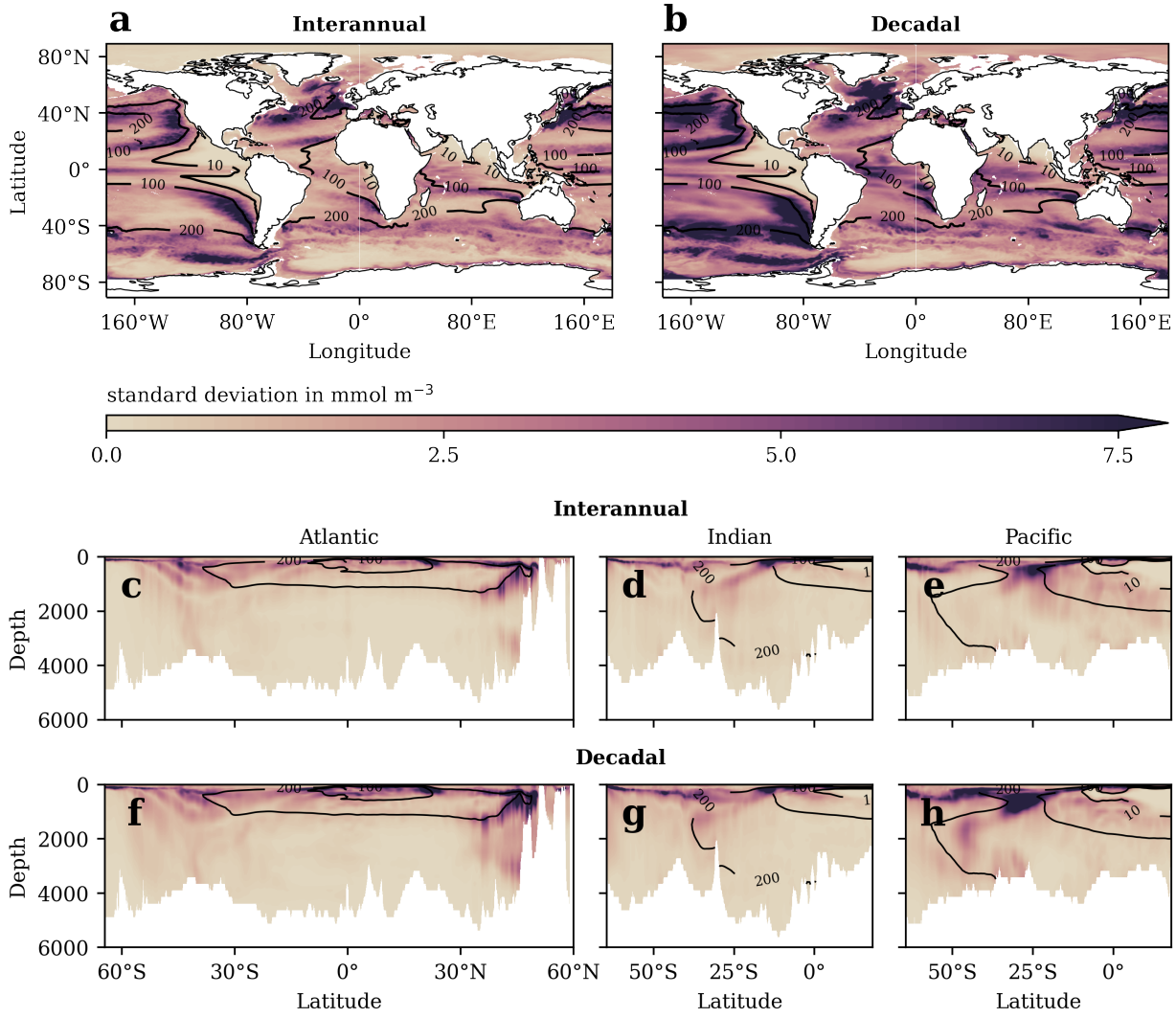

Figure 8: Standard deviations of **(a) & (c)-(e)** high-pass-filtered and **(b) & (f)-(h)** low-pass-filtered annual O_2 anomaly data from 1958-2018 simulated by ORCA025-MOPS $HIND_{ns}$ (ensemble mean) at **(a)-(b)** 300 m depth and along vertical sections across the **(c) & (f)** Atlantic (20°W), **(d) & (g)** Indian (90°E), and **(e) & (h)** Pacific (103°W) Oceans. High-pass-filtered data are considered to capture interannual variability and low-pass-filtered data are considered to capture decadal variability. Contour lines correspond to climatological mean O_2 concentrations (i.e., corresponding to Figure 2) of 10, 100, and 200 mmol m^{-3}.

Note: The approach for the high and low-pass filtering is described in Section 2.3.

extent of the OMZs. By contrast, the cores of the Pacific and Indian Oceans OMZs themselves show minimal variability, even after normalisation to mean concentration. This indicates that these areas have consistent and stable low oxygen levels with limited fluctuations over the simulated period.

4.3 Controls underlying oxygen trends

4.3.1 Global scale controls

To identify the underlying forcing factors behind the non-steady-state changes in global oceanic O_2 inventory (O_2^{ns}), the trajectories of its main drivers, namely solubility, ventilation, and remineralisation (estimated by analysing non-steady-state changes in O_2^{sat}, CFC-12 inventory, and remineralisation rate, respectively) are inspected first at a global scale (Fig. 9). For O_2^{sat}, which is defined in the same units as O_2, the share of O_2 changes due to O_2^{sat} changes can be calculated. For CFC-12 and remineralisation, which are defined in different units, this attribution cannot be made. Instead, the role of these processes is inferred by juxtaposing their temporal evolution with the trajectory of O_2.

The model simulations indicate that the global O_2 increase until the end of the 1960s (Fig. 9a [black line]) is primarily driven by increasing oxygen solubility (Fig. 9d [black line]). Specifically, almost half of the increase can be attributed to solubility (Table 5). Subsequently, until the end of the 1990s, oxygen solubility does not show a significant trend and its contribution to the O_2 trend falls to about 4% (Tables 5 and A.3). On the contrary, ventilation (Fig. 9c [black line]) decreases significantly by nearly 1% globally (Table A.3) and can be argued to be an important contributor to the concomitant global oxygen decline of about -45.72 $\pm$ 5.02 teramoles per decade (Table 5).

Since the mid-2000s, both reduced ventilation and reduced solubility contribute to the simulated increased decline, with solubility changes explaining

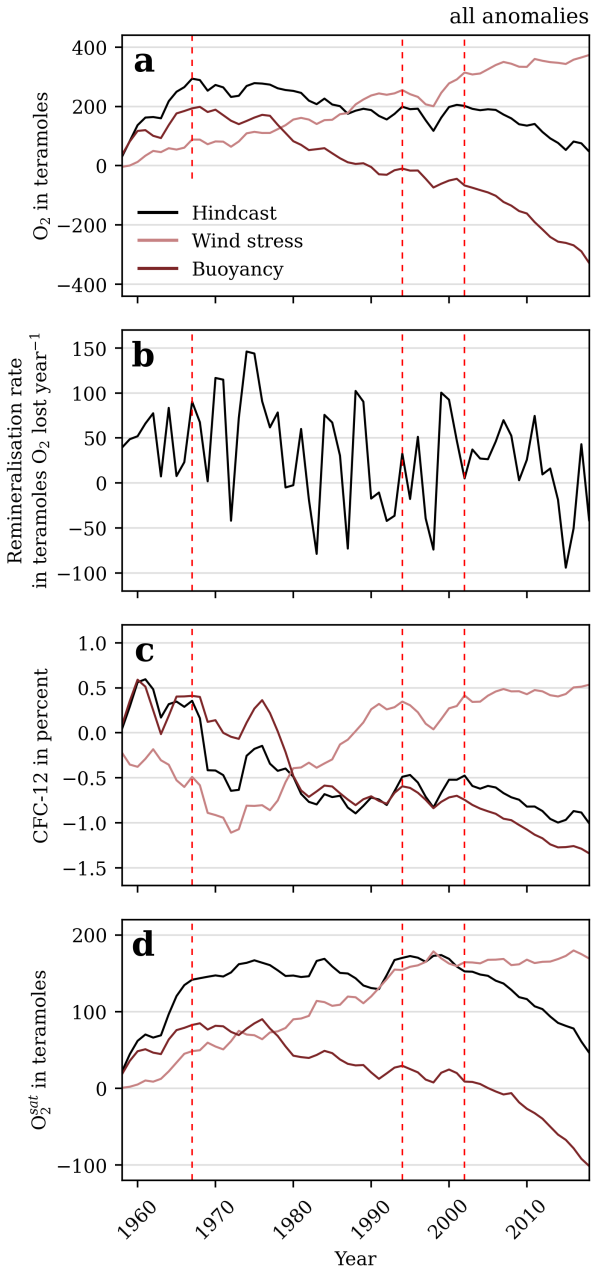

Figure 9: Time series of globally integrated **(a)** O_2 inventory, **(b)** remineralisation rate, **(c)** CFC-12 inventory, and **(d)** O_2^{sat} anomalies in ORCA025-MOPS $HIND_{ns}$ (black), $WIND_{ns}$ (rose), and $BUOY_{ns}$ (purple). Red dashed lines mark the four different periods of O_2 content evolution (Section 4.1.1). For CFC-12 inventory anomalies, percentages are computed relative to the CFC-12 inventory of the respective year as $HIND_{ns} \div CLIM \times 100$.

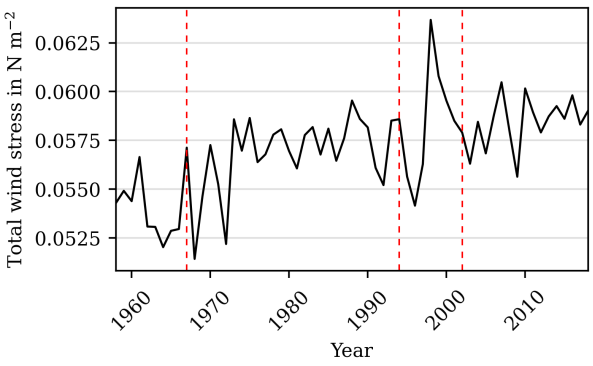

Figure 10: Annual time series of globally averaged total wind stress (vector sum) in the model. Red dashed lines mark the four different periods of O_2 content evolution as described in Section 4.1.1.

approximately 64% (Fig. 9, Table 5). Remineralisation rate shows a gradual yet consistent decline throughout the entire simulation period, superimposed to a high amplitude variability relative to the long-term decrease (Fig. 9b). The decline corresponds to a decline in respiratory oxygen consumption and acts to mitigate the deoxygenation trend posed by ventilation and solubility reductions.

In order to isolate the relative roles of year-to-year variability[8] in the wind stress versus air-sea buoyancy fluxes (hereafter 'buoyancy forcing') on oxygen inventory changes and its controls, the two sensitivity experiments ('wind stress' and 'buoyancy') are analysed in conjunction with the hindcast experiment. As detailed in Section 2.2, in the wind stress experiment, the year-to-year variability in wind stress is maintained (the annual time series of globally integrated wind stress shown in Figure 10), while the atmospheric variables needed to compute the air-sea fluxes of heat, freshwater, oxygen, and CFC-12 are in steady state. The buoyancy experiment maintains the year-to-year variability in the atmospheric variables needed to compute the air-sea fluxes of heat, freshwater, oxygen, and CFC-12, while the wind stress is in steady state.

In considering the sensitivity experiments, both wind stress (Fig. 10) and buoyancy forcing are found to be determining agents for the oxygen dynamics in the hindcast experiment, albeit with opposing effects on global oxygen inventory evolution (Fig. 9a). If the year-to-year variability of buoyancy forcing is suppressed, the model predicts a gradual and continuous increase in global oceanic oxygen inventory of about 64.18 $\pm$ 1.85 teramoles (0.026 $\pm$ 0.001% of global oxygen inventory) per decade throughout the simulation period (Fig. 9a [rose line]; Table 5). The regions most affected by the suppression of the year-to-year variability in buoyancy forcing (i.e., responding most strongly to the year-to-year variability in wind stress) are the equatorial regions (>1000 m), as well as the southern Indian and Atlantic Oceans and, since the late 1990s, the southern Pacific Ocean (Section 5.2.2). Conversely, suppressing the year-to-year variability in wind stress produces a consistent reduction in oceanic oxygen inventory from the late 1960s onwards, quantified as -92.23 $\pm$ 2.62 teramoles per decade. This corresponds to an oxygen depletion rate of -0.038% of the global oxygen inventory per decade, instead of -0.014 $\pm$ 0.001% simulated under retained wind stress variability (Fig. 9a [purple line]; Table 5). The regions most strongly responding to the year-to-year variability in buoyancy forcing (i.e., decreasing O_2 concentrations) are the deep Atlantic and deep Indian Oceans and, since the late 1990s, the >1000 m Southern Ocean (Section 5.2.1). Slight but steady declines are also simulated in all deep ocean basins except the deep equatorial Pacific and the Arctic Ocean.

A more detailed analysis of the changes in solubility and ventilation in the sensitivity experiments indicates that in Period i, both year-to-year variability in buoyancy forcing and wind stress promote increased oxygen solubility on a global scale, and thus lead to the rise in oxygen inventory (Table 5). In the following periods ii-iv, however, the dynamics change and

[8] year-to-year here refers to *all* variability *longer* than sub-annual

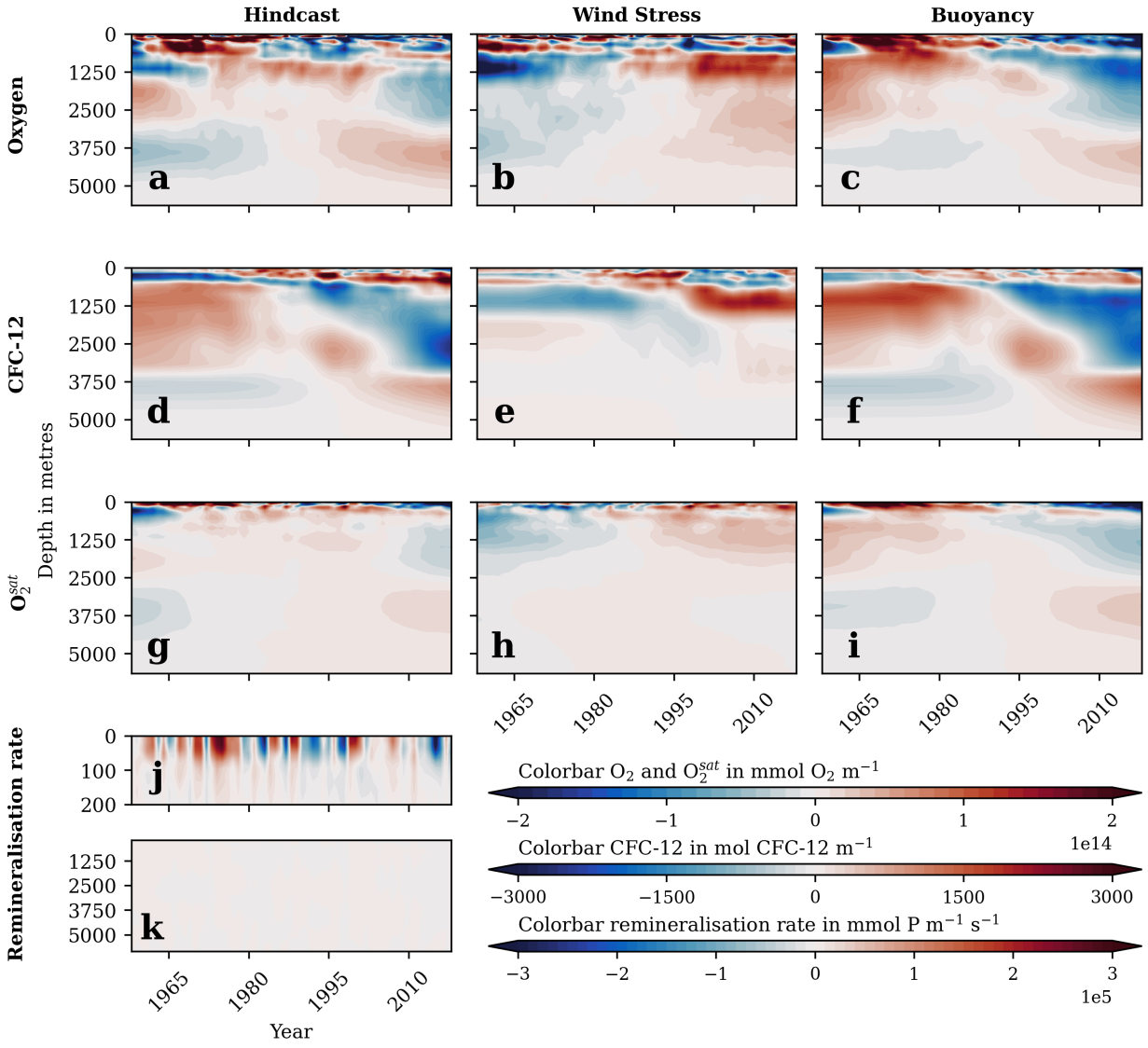

Figure 11: Hovmöller diagrams of **(a)-(c)** O_2 concentrations, **(d)-(f)** CFC-12 concentrations, **(g)-(i)** O_2^{sat}, and **(j)-(k)** remineralisation rate anomalies in HINDns, WINDns, and BUOYns. The data are mean-centred for each vertical level, using the 1958-2018 mean as reference.

Table 5: Change in globally integrated oxygen inventory and O_2^{sat} in teramoles per decade (and percentage of inventory per decade for oxygen inventory change) over the Periods i, ii, iv, and ii-iv described in Section 4.1.1, together with the respective percentage of oxygen inventory change explained by changes in O_2^{sat} (also volume integrated).

Experiment	Oxygen inventory change		O_2^{sat} change	O_2^{sat} rel. O_2 chg. in %
	Tmol dec^{-1}	percent dec^{-1}	Tmol dec^{-1}	
Period i (1960-1967)				
Hindcast	257.11 ± 26.67	0.105 ± 0.011	124.38 ± 14.01	48.38
Wind stress	87.54 ± 11.49	0.036 ± 0.005	51.40 ± 7.75	58.72
Buoyancy	148.1 ± 30.4	0.061 ± 0.012	64.34 ± 10.08	43.44
Period ii (1967-1994)				
Hindcast	-45.72 ± 5.02	-0.019 ± 0.002	-1.89 ± 2.77	4.13
Wind stress	69.07 ± 4.08	0.028 ± 0.002	36.86 ± 1.86	53.37
Buoyancy	-95.18 ± 4.56	-0.039 ± 0.002	-28.46 ± 2.24	29.9
Period iv (2002-2018)				
Hindcast	-109.18 ± 6.39	-0.045 ± 0.003	-69.75 ± 2.72	63.89
Wind stress	28.53 ± 5.9	0.012 ± 0.002	6.86 ± 2.54	24.04
Buoyancy	-174.8 ± 5.53	-0.072 ± 0.002	-76.66 ± 3.79	43.86
Period ii-iv (1967-2018)				
Hindcast	-34.23 ± 2.7	-0.014 ± 0.001	-11.96 ± 2.19	34.94
Wind stress	64.18 ± 1.85	0.026 ± 0.001	27.39 ± 1.35	42.68
Buoyancy	-92.23 ± 2.62	-0.038 ± 0.001	-29.86 ± 1.43	32.37

Note: (1) For details on the linear regression results see Tables A.2, A.3, A.4, and A.5 for periods i, ii, iv, and ii-iv respectively. (2) The oxygen inventory used to derive the percentage change is calculated as an average over the period in question.

the year-to-year variability of wind stress and buoyancy forcing determine changes in O_2 solubility and ventilation that mostly oppose each other, especially since the 1980s. While the year-to-year variability in buoyancy forcing dampens both oxygen solubility and ventilation, the year-to-year variability in wind stress continues to increase solubility and, since the early 1970s, also ventilation (Fig. 9). Since the mid-2000s, the counterforce of the wind stress-induced increases in ventilation and solubility is diminishing, the latter from about 36.86 ± 1.86 to about 6.86 ± 2.54 teramoles per decade. Conversely, the oxygen decrease imposed by buoyancy forcing nearly doubles, together contributing to the slightly faster decline in oxygen inventory since the 2000s (Table 5). Furthermore, the model simulations provide insight into the origin of the oxygen trough in 1998 (Fig. 5, Period iii). Interestingly, this transient low is suggested by the model to be driven by both wind stress and buoyancy forcing, and is primarily attributed to a reduction in ventilation, with O_2^{sat} contributing comparatively little.

In summary, the year-to-year variability in wind stress, which increases steadily from an average of about 0.053 N m^{-2} in 1958 to about 0.059 N m^{-2} in 2018 (Fig. 10), is responsible for a sustained increase in O_2 of about 64.18 ± 1.85 teramoles per decade, or about 0.026 ± 0.001% of the global oxygen inventory

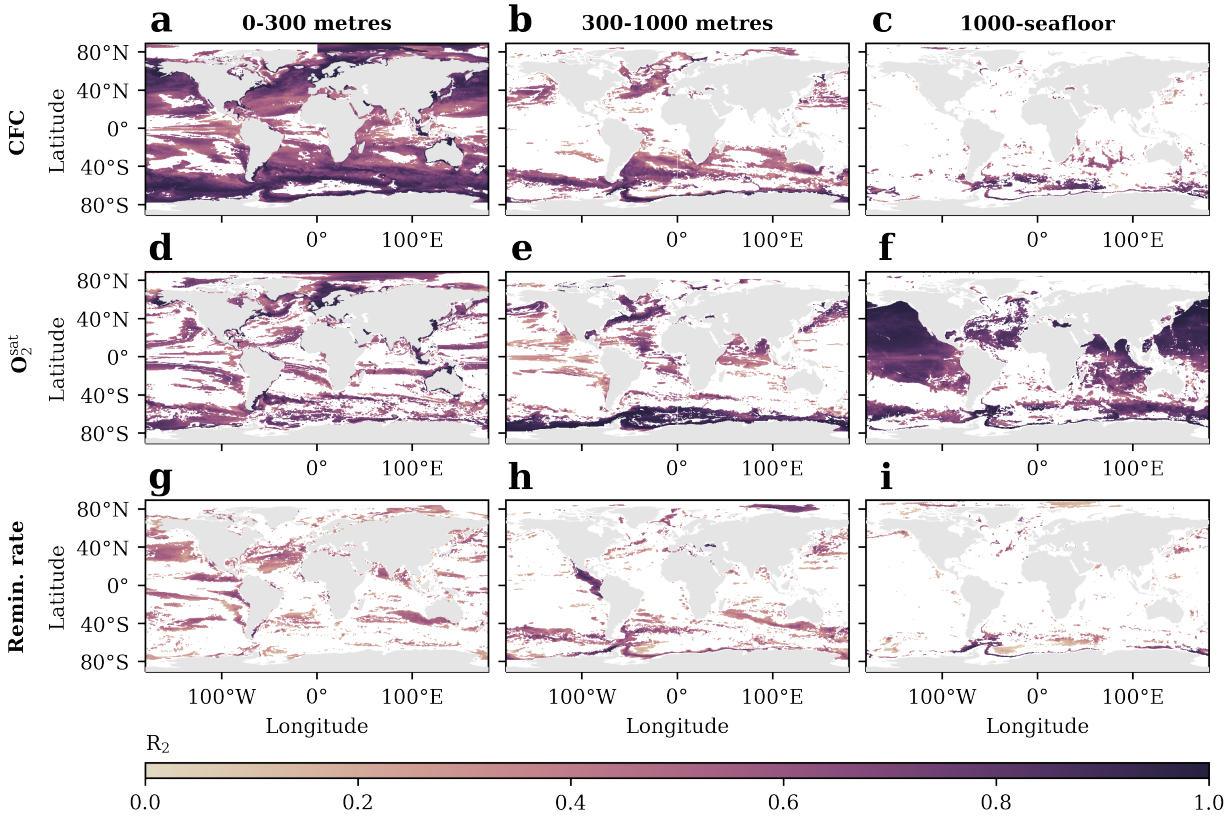

Figure 12: Coefficient of determination R^2 for simulated ($HIND_{ns}$) O_2 versus **(a)-(c)** CFC-12, **(d)-(f)** O_2^{sat}, and **(g)-(i)** remineralisation rate over 1958-2018 for three different depth horizons (columns). Regions with p>0.05 are shown in white, denoting non-significance.

per decade. It is clearly the changes in buoyancy forcing, dominated by changes in air temperature and precipitation, that have led to the decline in oxygen over the past decades in the model.

Incorporating the depth dimension yields a more thorough understanding of the simulated global scale trajectories (Fig. 11). In general terms, changes in oxygen content and oxygen solubility arise mainly in the upper 2,500 m of the water column, whilst there are limited shifts at depth. Changes in ventilation penetrate deeper into the water column mainly due to buoyancy forcing changes, and in contrast the considerable amplitude of variability in remineralisation rate is largely generated above a threshold depth of 100 m.

As shown in Figure 11a, the increase in oxygen up to the late 1960s is mainly concentrated in the upper 1,000 m of the water column. This increase is primarily due to increased oxygen solubility, largely determined by buoyancy forcing in the 0-500 m depth range (Fig. 11i). In addition, modest wind stress-induced changes in solubility in the 500-1,000 m depth range contribute to this increase (Fig. 11h). Thereafter, the decline in oxygen inventory since the 1960s extends to about 3,000 m and is particularly pronounced above 250 m as well as at depths below 1,000 m (Fig. 11a). While the decline above 250 m, including the increased downward trend after the 2000s, is mainly the result of an buoyancy-induced decrease in both solubility and ventilation in this depth range, below 250 m the buoyancy-induced drop in ventilation becomes the dominant contribu-

tor to the decline (Figs. 11f and 11i). Notably, in the depth range from 250 to 1,000 m, wind stress acts to mitigate the decline (Fig. 11b). Its influence is manifested in increased ventilation, especially between 500 and 1,300 m (particularly from 1980 to 1995), and increased solubility in the upper 2,000 m, resulting in minor oxygen changes in the 250-1,000 m depth range (Figs. 7b and 11a).

4.3.2 Regional scale controls

While the trends identified hold true in a global context, it is important to recognise that the influence of the controlling factors is distinctly heterogeneous across regions. To further explore this regional variation in the strength of the influence of solubility, respiration, and ventilation on oxygen levels, correlation analyses were performed with the resultant R^2 values presented in Figure 12.

Ventilation is most strongly correlated with oxygen in the upper ocean (<300 m) at high and mid-latitudes (Fig. 12a-c). At intermediate depths (300-1,000 m), however, this close association fades. Here, significant correlations are found mainly in regions closely tied to water mass formation, namely the Southern Ocean and the North Atlantic. Below 1,000 m, a significant correlation between oxygen and ventilation is found only in the Southern Ocean.

The impact of remineralisation is mainly concentrated above 1,000 m, with robust correlations particularly above 300 m depth (Fig. 12g-i). These correlations are most prominent adjacent to the eastern boundary upwelling zones, in the Arabian Sea, Gulf of Bengal, and along the 40° latitude bands in both hemispheres. At intermediate depths (300-1,000 m), the influence of remineralisation in controlling oxygen levels decreases, although sporadic strong correlations persist, particularly in the eastern equatorial Pacific. Other significant correlations are found in the Arctic Ocean in the Laptev and Kara Seas, in the western North Pacific, and in the Southern Ocean,

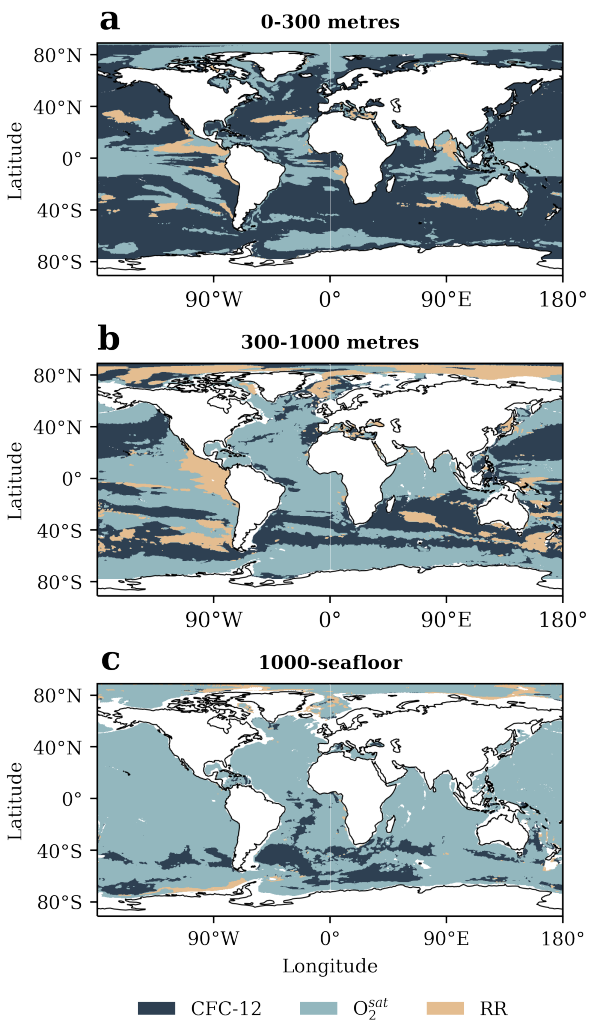

Figure 13: Global map of regionally highest coefficient of determination R^2 for simulated ($HIND_{ns}$) O_2 versus CFC-12, O_2^{sat}, and remineralisation rate over 1958-2018 for the **(a)** upper, **(b)** intermediate, and **(c)** deep ocean.

especially near the Antarctic continent in the Weddell and Scotia Seas. In the Southern Ocean, this correlation extends in places into the deeper ocean layers.

Solubility shows consistent and strong correlations with oxygen throughout the water column (Fig. 12d-f). Within the upper 1,000 m, these correlations are most evident along the eastern boundary currents, equatorial currents, and in the Southern Ocean. However, with increasing depth, the pattern changes con-

siderably. O_2^{sat} forms a particularly tight link with oxygen from 1,000 m depth to the seafloor, most strongly in the Pacific Ocean. This close correlation is interrupted sporadically by non-significant patches along the 40th parallel south, as well as in the Arctic Ocean and SH Atlantic Ocean.

In summary (Fig. 13), the influence of remineralisation is geographically localised and predominantly operates above 1,000 m depth. Oxygen dynamics in the 0-300 m range are mainly influenced by remineralisation near major upwelling systems and along the 40th parallel north and south. This influence continues to greater depths in the eastern equatorial Pacific and along the 40th parallel south, and is particularly important in controlling oxygen dynamics in the Arctic Ocean. Ventilation exerts its greatest influence from the surface to about 1,000 m, mainly in the mid-latitudes. However, its influence decreases sharply with depth and extends into the intermediate and deep ocean only in regions associated with water mass formation. Solubility, in contrast, remains an important factor throughout the depth profile. At 0-1,000 m its influence dominates patches mainly at low and high latitudes in both hemispheres, while in the deep ocean oxygen concentrations are most closely correlated with O_2^{sat} in nearly all ocean basins, apart from few regions in the Southern Ocean.

4.3.3 Regional in-depth analysis

Special emphasis is placed on two specific regions: (1) the North Atlantic Ocean, of major importance for deep ocean oxygenation due to its prominent role in deep-water formation (Koelling et al. 2022), with far-reaching implications also for distant ocean basins (Schmittner et al. 2007), and (2) the equatorial Pacific, which, despite hosting an intense OMZ, is commonly poorly modelled regarding oxygen trends (Oschlies et al. 2017). The area boundaries are specified in Table 3 and shown in Figure A.16.

As shown in Figure A.17e-h, in the deep North Atlantic (>1,000 m) the model simulates a decline in oxygen concentrations during Period i, followed by an increase during Period ii, spanning a small local maximum in oxygen concentrations in the mid-1970s. Subsequently, from the beginning of Period iii, oxygen concentrations decline at a similar rate to Period i. Towards the end of the simulation period, oxygen levels stabilise. Throughout the simulation period, the model suggests that changes in oxygen are primarily due to buoyancy-induced changes in both solubility and ventilation. Changes in remineralisation rates, although minor, are generally positively correlated with oxygen concentrations, implying that any trend in oxygen concentrations would be attenuated by remineralisation dynamics. Compared to changes in oxygen concentration, changes in solubility are of lesser magnitude, typically accounting for less than a third of the simulated oxygen trends, pointing to ventilation as the dominant driver. In the overlying strata (<1000 m) the modelled oxygen concentrations are more variable (Fig. A.17a-d). A slight decrease in oxygen content spans Periods i-iii and is followed by an increase from the mid-2000s. This trend is simulated to result from buoyancy-induced changes in both ventilation and solubility, with solubility contributing about half. A clear link to remineralisation is absent. Strikingly, changes in the North Atlantic are predominantly determined by shifts in buoyancy forcing; its year-to-year variability suppressed, changes in solubility, CFC-12, and oxygen are minor, indicating a limited influence of the year-to-year variability in wind stress to local oxygen dynamics.

The modelled trend in oxygen for the eastern equatorial Pacific is shown in Figure A.18. Above 300 m, oxygen concentrations do not follow any significant long-term trend, but are characterised by a high degree of variability, negatively correlated with strong fluctuations in remineralisation rate. Interestingly, oxygen solubility is also modelled to fluctuate in antiphase with oxygen concentrations, with changes

driven primarily by year-to-year variability in wind stress. Conversly, changes in ventilation show a positive correlation with oxygen concentration. Between 300 and 1,000 m depth, the model indicates an increase in oxygen concentrations in Periods i and ii and a subsequent decrease from Period iv onwards. The clear relationship with remineralisation weakens and changes in remineralisation rate decrease by a factor of about 10. While the 1958-2018 oxygen trajectory modelled for the mid-depth equatorial Pacific is clearly due to the year-to-year variability in wind stress and the recent decrease clearly attenuated by the year-to-year variability in buoyancy forcing, a distinct linkage to all three drivers analysed is absent.

In summary, the simulated oxygen trend for the North Atlantic Ocean largely reflects buoyancy-driven changes in both solubility and ventilation; the influence of year-to-year variability in wind stress is negligible. Remineralisation acts to moderate any trend, especially below 1000 m (although the small magnitude of its shifts suggests a limited influence on oxygen trends). In the eastern equatorial Pacific, strong surface variability is related to remineralisation and wind-induced changes in ventilation. While between 300 and 1,000 m the recent decline is also clearly related to year-to-year variability in wind stress, a particular driver remains unidentified.

Box 5 Section 4: Key takeaways

1. Changes in the global oxygen inventory from 1958-2018 are clustered into four periods (i-iv) and evaluated against observations [Figs. 5, 6, 7, 9, and 11; Sections 4.1.1 and 4.3.1]:
   - 1.1 1958-1967: Increasing inventory due to enhanced solubility from buoyancy forcing (0-500 m) and wind-stress-induced changes (500-1,000 m); consistent with observations.
   - 1.2 1967-1994: Gradual decrease mostly at <3,000 m depth due to a buoyancy-induced decrease in solubility and ventilation; consistent with observations.
   - 1.3 1994-2002: Anomalous decline, followed by rapid recovery; consistent with observations.
   - 1.4 2002 onwards: Continued but accelerated decline (see 1.2 above), with emerging model-observation mismatch (<1,000 m): severity of the decline is not captured by the model.
2. The largest variability in oxygen concentrations is found in highly dynamic ocean regions, e.g. regions of water mass formation, frontal shifts, and ocean-sea ice interaction. The highest *relative* variability (i.e., relative to the mean oxygen concentration) is found at the edges of the OMZs. [Figs. 8 and A.15; Section 4.2]
3. At a global scale, while the year-to-year variability in wind stress is responsible for a sustained increase in O_2 over the last 60 years, it is clearly the changes in buoyancy forcing that have caused the decrease in oxygen inventory in the model. [Fig. 9; Section 4.3.1]
4. At a regional scale the influence of controlling factors is heterogeneous and has been estimated using the coefficient of determination R^2 [Figs. 12 and 13; Section 4.3.2]:
   - 4.1 Remineralisation: Strong correlations mainly <1,000 m and geographically localised, e.g. near upwelling systems, along the 40^{th} parallel N and S, and in the mid-depth Arctic Ocean.
   - 4.2 Ventilation: Dominant influence <1,000 m, especially at mid-latitudes.
   - 4.3 Solubility: Strongest correlations at low and high latitudes. In the deep ocean, O_2^{sat} dominates R^2 in most ocean basins. Only in the Southern Ocean does ventilation dominate in places.
5. Regional in-depth analyses [Figs. A.17 and A.18; Section 4.3.3]:
   - 5.1 North Atlantic: Generally, changes in the North Atlantic are primarily controlled by buoyancy forcing rather than wind stress, with the strong decrease since the 1990s (>1,000 m) mainly attributed to buoyancy-driven changes in both solubility and ventilation.
   - 5.2 Eastern equatorial Pacific: Large variability <300 m mostly related to remineralisation and ventilation changes. Recent mid-depth decline (300-1,000 m) attributed to year-to-year variability in wind stress, but no clear driver identified.

5 Discussion

In this study, a global ocean biogeochemical model was used to analyse the temporal evolution and regional patterns of oxygen trends and variability to gain a better mechanistic understanding of their drivers.

The analysis identified four key periods in the time series of simulated global oceanic oxygen content (Fig. 5): (i) From 1958 to 1967, global oceanic O_2 increased by 218.7 $\pm$ 33.9 teramoles per decade; (ii) From 1967 to 1994, O_2 gradually decreased by -46.6 $\pm$ 4.5 teramoles per decade; (iii) Between 1994 and 2002, O_2 declined sharply until 1998, followed by a rapid recovery; (iv) Afterwards, O_2 continued to decline at an accelerated rate of -108.6 $\pm$ 7.6 teramoles per decade. While the model was in line with observations until the early 2000s, a significant discrepancy emerged thereafter, with the model simulating a rate of decline around three times lower than that observed over the same period (Fig. 6).

Changes in buoyancy forcing, mainly influenced by shifts in air temperature and precipitation, were identified as the primary driver of the recent decline, with increasing wind stress acting as a consistent counterforce (Fig. 9a). Regionally, there is strong variability in oxygen concentrations, the magnitude of which is usually well above the prevailing long-term trends. The greatest variability in oxygen concentrations was found in highly dynamic oceanic regions, such as those characterised by water mass formation, frontal shifts and ocean-sea ice interactions (Fig. 8), and matched observations reasonably well in terms of both spatial distribution and magnitude. Significant and structural differences were found in the drivers of variability and long-term oxygen trends between regions, revealing high complexity of regional oxygen dynamics and the need for a more differentiated understanding of the underlying mechanisms.

Below I discuss these results and identify key areas for future research. Before doing so, however, I address the major limitations of this study and discuss their potential impact on the robustness of the results presented.

5.1 Limitations

A significant limitation arises from the inherent uncertainty associated with the observational data used in ocean reanalysis product. In JRA55-do, before 1979, the precipitation dataset is missing interannual variability (Tsujino et al. 2018), which introduces uncertainty that particularly affects the hindcast and buoyancy forcing experiments. Furthermore, while the JRA55-do dataset provides high-quality and realistic spatial wind patterns, regional-scale inconsistencies with observations have been found, particularly in coastal, equatorial, and (sub)polar regions (Taboada et al. 2019). Taboada et al. (2019) caution that the significant mismatches in high latitudes, which are particularly strong in areas of deep convection and along the path of the Antarctic Circumpolar Current, may affect the rate of deep water formation and upwelling, and in coastal regions, may impede the correct reproduction of transport patterns, leading to biases in the model's heat and nutrient fluxes.

Uncertainties also arise from biases associated with errors in the representation of biogeochemical and physical processes in the model. For example, it has been suggested that the temperature dependence of remineralisation may impact on O_2 concentrations through shoaling of remineralisation profiles (Segschneider & Bendtsen 2013; Oschlies 2019). In MOPS, remineralisation is temperature-independent and these effects are not considered. Currently, ORCA025-MOPS also neglects iron limitation of primary productivity. In regions where iron is the limiting factor for phytoplankton growth, such as the Southern Ocean, but also in upwelling regions (Basterretxea et al. 2022; Browning et al. 2023), this omission may lead to an overestimation of primary production and the substrate available for remineralisation. Conversely, the absence of additional and in-

creasing anthropogenic nutrient inputs from coastal runoff, a major cause of coastal deoxygenation (Rabalais 2019), and atmospheric nutrient deposition may lead to an underestimation of net primary productivity. It has also been suggested that phytoplankton growth in surface waters often approaches nutrient co-limitation (Browning & Moore 2023). In ORCA025-MOPS such processes are not accounted for and thus may introduce additional bias into the surface biogeochemical dynamics.

A note of caution is also in order regarding the approach to estimating ocean ventilation. Although by calculating anomalies as (HIND−CLIM) ÷ CLIM×100 the approach effectively accounts for the non-linear increase in atmospheric CFC-12, the analysis is limited to regions where CFC-12 is present. CFC-12 was first produced in the early 20^{th} century and has been accumulating in the atmosphere mainly since the mid-20^{th} century (Walker et al. 2000). Therefore, a water parcel can only carry the atmospheric CFC-12 imprint if it has equilibrated with the atmosphere during the time CFC-12 was already present. However, the timescales associated with ventilation, particularly in the deep ocean, are slow and the average age of a water parcel (i.e., the time elapsed since its last contact and equilibration with the atmosphere) increases rapidly with depth, especially in the upper 1,000 m of the water column (England & Rahmstorf 1999). In this study, while CFC-12 eventually reaches all sub-regions and depth ranges considered, concentrations in the deep ocean are significantly lower, often by several orders of magnitude compared to the upper 1,000 m of the water column (Figs. A.19, A.20, and A.21).

This situation has several important implications:

1. The methodology for estimating ventilation anomalies introduces non-homogeneous uncertainties in the time dimension.
2. The uncertainty increases non-linearly with depth, with large uncertainties especially below 1,000 m.
3. The approach may introduce a disproportionate influence of younger water masses. If CFC-12 concentrations in the deep ocean are zero, both in the climatological and in the hindcast or sensitivity experiments, then any changes in ventilation are invisible to the approach applied and may thus be underrepresented in the integrated estimates.

In summary, whilst the ventilation estimation approach applied here is valuable, it is imperative to recognise its limitations, particularly when considering the sluggish dynamics of deep ocean ventilation and the resulting spatial and temporal variability in CFC-12 concentrations. The validity of ventilation estimates at the beginning of the simulation period as well as for old water masses is debatable and should be treated and interpreted with caution.

In addition to the uncertainties that affect this study's analysis and results, the observational data products used to evaluate model performance are themselves subject to uncertainty. Observational gridded datasets have three major sources of representational uncertainty (Zumwald et al. 2020): (1) the uncertainty inherent in the imprecision of the measurements and observations themselves; (2) the uncertainty associated with any further processing of the measurement results, including the interpolation and synthesis of the observations into continuous spatial fields; and (3) the uncertainty introduced by a biased sample, which arises because measurements are usually not homogeneously or randomly distributed in space (e.g, remote regions are often undersampled; but coverage may change over time), and may also be biased in time (e.g., if the accuracy of measurements changes or if measurements are confounded by other time-varying factors). For GOBAI-O_2 in particular, Sharp et al. (2022) additionally decompose (2a) the uncertainty associated with the gridding process, and (2b) the uncertainty introduced by the applied

machine-learning algorithm. This machine-learning-introduced error is the largest component of the total uncertainty in their dataset and is unevenly distributed across space, with the largest uncertainties found in the major upwelling regions. For more information on the dataset-specific uncertainties and their assessment, the reader is referred to Ito et al. (2017) for Ito-17, Sharp et al. (2022) for GOBAI-O_2, and Garcia et al. (2013) and Garcia et al. (2019) for the World Ocean Atlas 2013 and 2018 respectively.

Nonetheless, despite these uncertainties inherent to observational data, it is now clear that a consistent and alarming trend has emerged, with the global oceanic oxygen content declining at a concerning rate (Schmidtko et al. 2017). This decline was significantly underestimated by the model, as is common in current state-of-the-art models (Oschlies et al. 2017), and is addressed in Section 5.5.

5.2 Past oxygen trends

While acknowledging these limitations, this study provides important insights into the changes of global and regional oceanic oxygen levels as well as its driving forces. In brief, two main trends have been identified throughout the time span analysed (Fig. 5): Initially, during the first 10 years of the simulation period, the oceanic oxygen inventory increased. It then declined persistently (with a short discontinuity around the 2000s) until the end of the simulation period, with the rate of change accelerating after the early 2000s. This recent decline was clearly set by changes in buoyancy forcing, while the year-to-year variability in wind stress served to modulate and mitigate this decline (Fig. 9a), particularly in intermediate waters (Fig. 11b).

Interestingly, prior to the onset of the buoyancy forcing-induced oxygen decrease starting in the 1970s, the year-to-year variability in buoyancy forcing also contributed to the increase in oxygen inventory, thus strengthening the wind stress-induced increase in this early period (Fig. 9a). This implies that in some episodes wind stress and buoyancy forcing reinforce each other (Periods i and iii), while in others they counteract and cancel each other out (Periods ii and iv), pointing to a (partial) independence of their variability.

5.2.1 Buoyancy forcing-induced changes

However, despite both of these factors being key determinants of oxygen dynamics, as well as their ability to vary independently, the trajectory of the global oxygen inventory in the hindcast scenario (i.e., retaining the year-to-year variability of both the wind stress and the buoyancy forcing) closely parallels that of the global ocean heat content (OHC), with a strong negative correlation of r = -0.85 and r = -0.80 for the 0-700 m and 0-2,000 m layers, respectively (Fig. 14). This is consistent with the results of Ito et al. (2017), who found a strong negative correlation of r = -0.86 between the O_2 inventory and OHC for the 0-1,000 m layer, and Bopp et al. (2013), who found that changes in OHC explain >99% of the variation in O_2 content between 200 and 600 m. This agreement between the O_2 and OHC trajectories[9] strongly suggests that the major contributors to oxygen dynamics within the year-to-year variability in buoyancy forcing are well associated with the global OHC.

However, while the most immediate influence in this relationship arises from the direct thermally induced solubility effect - the alteration of oxygen solubility due to temperature changes in seawater - its contribution to total oxygen changes is relatively modest on a global scale (Ito et al. 2017; Couespel et al. 2019) and mainly confined to the uppermost 1,000 m of the water column (Schmidtko et al. 2017). This sug-

[9] considering that the year-to-year variability in wind stress produces a strongly linear O_2 long-term trend (63.54 ± 1.38, F-statistic = 2126(1,59), p = 0.000, R^2 = 0.973) throughout the study period, and thus rather than modifying the fundamental shape of the global O_2 inventory trajectory, mainly changes its steepness

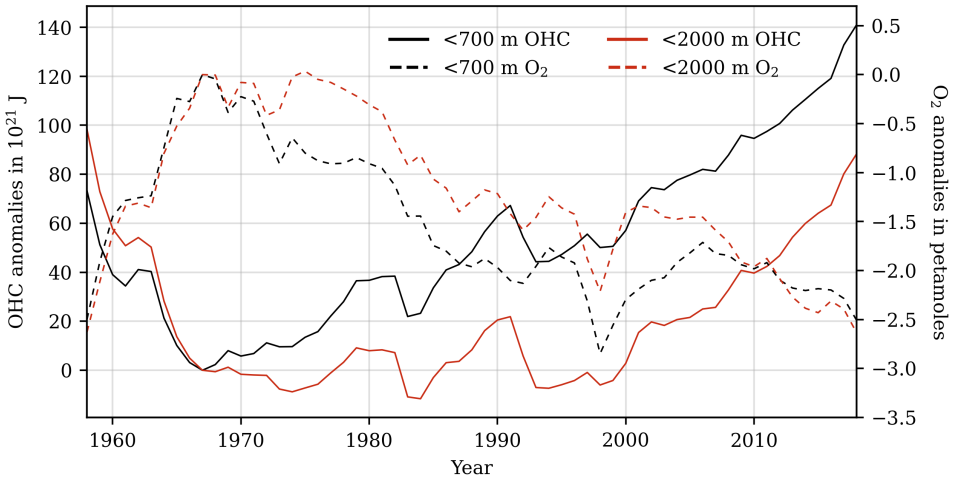

Figure 14: Time series of global ocean heat content anomalies (solid lines) and O_2 inventory anomalies (dashed lines) for the 0-700 m (black) and 0-2,000 m (red) layers in ORCA025-MOPS $HIND_{ns}$. Reference year is 1967.

gests that the remaining key factors underlying oxygen changes (i.e., ventilation and biological consumption) are also sensitive to changes in global OHC, and thereby strengthen the global oxygen-OHC coupling.

In addition to the direct thermally induced solubility effect, ocean warming sets in motion a cascade of responses throughout the ocean. Ocean warming directly alters biochemical cycles, for example by modulating metabolic rates (Brewer & Peltzer 2017), but also alters ocean dynamics - the motion of water in the ocean - by changing ocean stratification and mixing patterns, and shifting ocean currents (Fox-Kemper et al. 2021; Johnson & Lumpkin 2022). These changes in ocean dynamics may again directly or indirectly affect all three major causes of oxygen change (i.e., solubility, ventilation, and remineralisation). In the case of remineralisation, for example, the global strengthening of near-surface stratification reduces the supply of inorganic nutrients from the subsurface to the sunlit surface ocean, which is considered the primary reason for the decline in global net primary production and subsequent remineralisation with ocean warming, as both observed (Moore et al. 2018; Bindoff et al. 2019) and simulated by the model. Regionally, however, changes in vertical mixing and sea ice dynamics may potentially increase local primary production by altering light availability and conditions for primary production, particularly in the polar regions (Arrigo et al. 2008; Llort et al. 2019; Kim & Kim 2021), and may account for the strong simulated increase in remineralisation in the Arctic Ocean since 1970 (Fig. A.23i). Further, ocean warming affects the Earth's cryosphere, causing changes in freshwater fluxes that feed back into ocean dynamics with the implications outlined above.

I emphasise that due to the complexity of the mechanisms operating, the correlation between O_2 and OHC may vary regionally and vertically, despite being robust on a global scale. Two important mechanisms may contribute to this:

1. Regions with significant increases in OHC often signal the presence of water mass formation processes (Bronselaer et al. 2020; Fox-Kemper et al. 2021). However, as the surface ocean warms and ice sheets melt, near-surface stratification increases and inhibits the sinking of surface waters. This potentially slows down the rate of water mass formation (Cheng et al.

2022; Lee et al. 2023) and the injection of oxygen into the interior, reinforcing the negative correlation between OHC and oxygen inventory. However, when ocean circulation and mixing processes are considered, this relationship becomes more complex at depth. Ocean currents transport water masses and properties away from their source regions, initiating mixing within the ocean interior. As reduced water mass formation slows the penetration of warm water to greater depths and simultaneously reduces the introduction of oxygen, smaller temperature changes may potentially be associated with larger oxygen inventory changes at depth.

2. Ocean warming also has the potential to reduce the large-scale overturning circulation (Bakker et al. 2016; Caesar et al. 2018). While this leads to a global and immediate decrease in oxygen concentrations in the ocean interior, as less oxygen-rich water is pushed into oxygen-poor regions (Visbeck 2007), this reduction will not be immediately reflected in temperature changes within the ocean - basically because there is no 'sink' for temperature in the ocean interior, as there is for oxygen - and implies the transport of less (anomalously warm) surface water into the interior.

The oxygen inventory is shown to be less sensitive to changes in OHC in shallower waters (Fig. A.22). This is consistent with the findings of Ito et al. (2017), who found that while above 100 m the regression coefficient of O_2 inventory and OHC was consistent with the expected relationship based on O_2 solubility, below the thermocline O_2 levels were significantly more sensitive to changes in OHC. I hypothesise that the effects outlined above may contribute to this heightened sensitivity of oxygen inventory to changes in OHC at depth.

However, there is a further layer of complexity to the relationship between oceanic oxygen and OHC. Changes in OHC in recent decades have been dominated by greenhouse gas (GHG) emissions from human activities, which have altered the atmospheric composition to cause an energy imbalance in the Earth's climate system (von Schuckmann et al. 2020). While about 90% of the Earth's energy imbalance (1971-2018) is stored in the oceans, 4% and 1% have been absorbed by the Earth's cryosphere and atmosphere, respectively (von Schuckmann et al. 2020). Accordingly, by all responding to the growing energy imbalance, the heat gain in these compartments is indirectly related, and thereby may produce a (partly) spurious correlation between OHC and oxygen. This is because heat gain in the Earth's cryosphere and atmosphere can, for example, cause changes in the Earth's freshwater fluxes (e.g., by shifting precipitation patterns and the melting of grounded and floating ice), which may similarly affect the ocean system and oxygen inventory by altering ocean dynamics, but are separate in cause from OHC-induced changes.

Fluctuations in freshwater fluxes act on oxygen mainly by changing the salinity and density of seawater, which in turn modifies ocean stratification. This effect is particularly important in regions characterised by deep-water formation, where the combined effects of temperature and salinity are critical in shaping the properties of surface waters and their ability to sink. Although estimating precise long-term trends in precipitation, especially in distant historical periods, remains challenging, general trends have been identified. These trends suggest that regional differences in sea surface salinity have increased since the 1950s. Specifically, evaporation-dominated mid-latitudes have become more saline, while precipitation-dominated tropical and polar regions have become fresher (Fox-Kemper et al. 2021, Sun et al. 2021).

I conclude that the relationship between O_2 and OHC emerges as a composite result of a range of climatic

changes that collectively affect oxygen dynamics - in this study largely isolated by the buoyancy forcing sensitivity experiment.

Over the past decade, increases in the 0-2,000 m OHC have been observed throughout the global ocean (Levitus et al. 2012; Garcia-Soto et al. 2021). Almost half of this warming has been concentrated in the Southern Ocean, where warming is assumed to also extend into the deeper ocean, mainly due to warming of the AABW (Fox-Kemper et al. 2021). However, while the modelled ventilation in the deep Southern Ocean has been decreasing since about 1970 (Fig. A.24j), as would be expected from a continuous buoyancy gain, oxygen solubility instead introduces large, low-frequency variability into the oxygen trend instead of an expected decrease (Fig. A.25j), thereby introducing large uncertainties into any long-term trend. This suggests (1) possible biases in the representation of ocean heat uptake and storage (discussed in 5.5) and (2) changes in freshwater forcing as the primary driver of the simulated decrease in ventilation. The latter is supported by the results of Lee et al. (2023), who attributed the 10-20% weakening of the lower Southern Ocean circulation cell observed since the mid-1970s to increased outflow of Antarctic meltwater from the Amundsen-Bellingshausen Sea into the Ross Sea and a subsequent reduction in the formation of the AABW.

In addition, a significant increase in the OHC has been observed between 50°S and 30°S, particularly in the southern Indian Ocean and the southern Atlantic Ocean (Levitus et al. 2012). These trends are consistent with the notion of efficient transport of temperature signals to greater depths by water mass formation processes, namely AAIW and Subantarctic Mode Water (SAMW). This study's analysis generally supports this idea. A decrease in oxygen content due to year-to-year variability in buoyancy forcing has been simulated at intermediate depths in the southern Indian Ocean since the late 1960s (Fig. 14h [purple lines]), and in the South Atlantic and South Pacific since the mid-1970s (Fig. 14c,f [purple lines]). However, the hindcast simulation shows a net zero change in the O_2 inventory in the southern Indian Ocean and an increase in the O_2 inventory in the Pacific since the mid-1990s, which is the result of a strong counterbalance from changes in wind stress (Fig. 14c,f,h [rose lines]), as discussed in more detail in Section 5.2.2 below.

In the NH, the increase in OHC is disproportionately small (Fox-Kemper et al. 2021), and while significant cooling trends are largely absent, the subpolar Atlantic is an important exception (Caesar et al. 2018). This local cooling coincides with warming in the Gulf Stream region and partly reflects the slowdown of the AMOC, reduced northward heat transport, and a northward shift of the Gulf Stream (Caesar et al. 2018). The slowdown of the AMOC is likely to contribute to the simulated buoyancy-driven oxygen decrease in the deep ocean on a global scale (Fig. 14.3 [purple lines]). The strength of the AMOC is associated with the formation of NADW (Fox-Kemper et al. 2021), likely contributing to the simulated, mostly ventilation-driven decrease in oxygen in the deep North Atlantic Ocean (Fig. A.17). However, oxygen levels in the North Atlantic are strongly modulated by the variability induced by the North Atlantic Oscillation and Atlantic Multidecadal Oscillation, which are the dominant climate controls over the North Atlantic Ocean (Montes et al. 2016) and impose uncertainty on the interpretation of prevailing long-term trends.

5.2.2 Wind stress-induced changes

In tropical regions, by contrast, the year-to-year variability in buoyancy forcing is of minor importance in determining oxygen dynamics in the model. Instead, in the equatorial regions across all ocean basins, a complex interplay of multiple factors comes to the fore, all seemingly coordinated by the year-to-year variability in wind stress, especially in the upper 300 m of the water column (Fig. 14b,e,g [rose lines]).

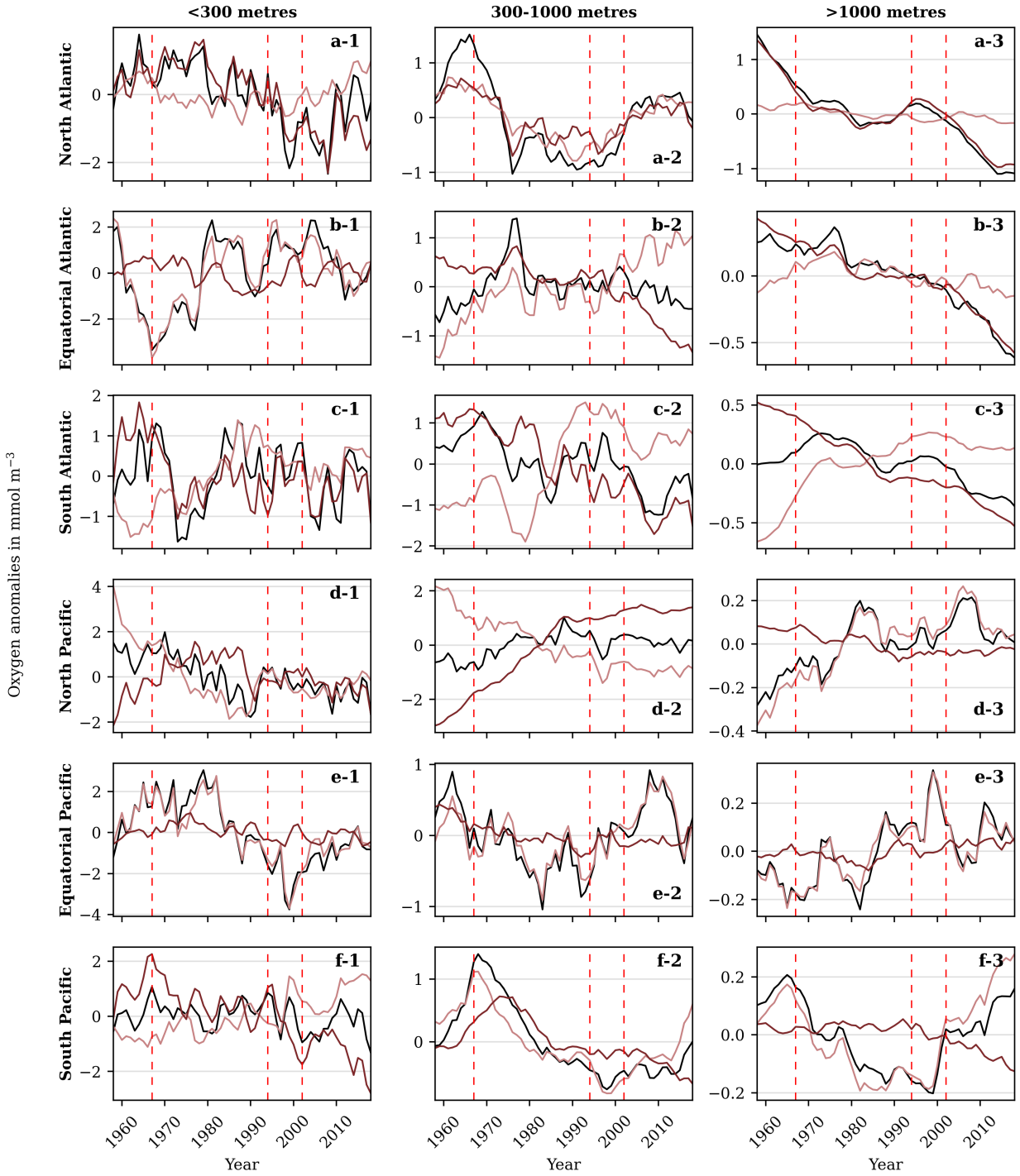

Figure continues on the next page.

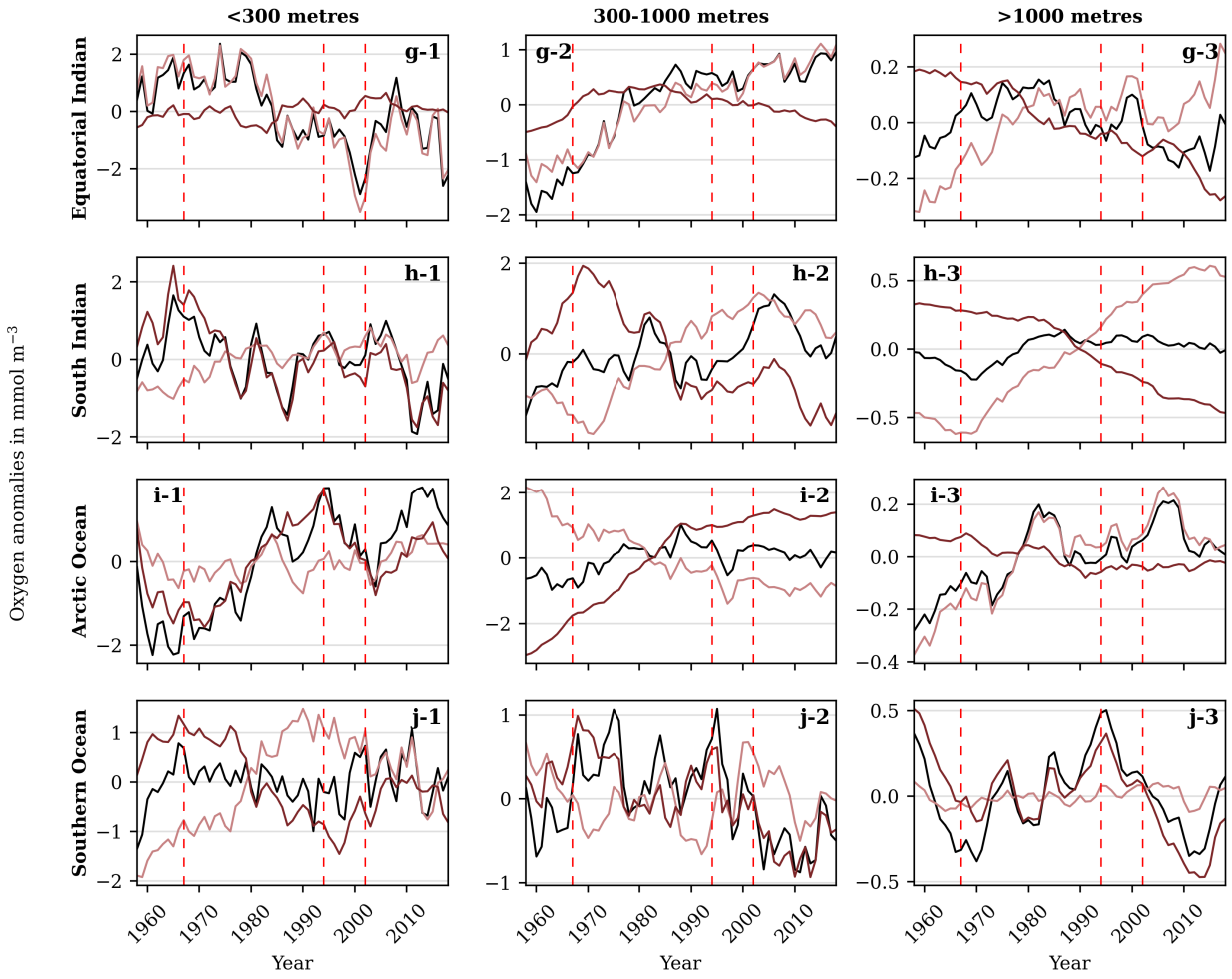

Figure 14: Time series of O_2 concentration anomalies in ORCA025-MOPS $HIND_{ns}$ (black), $WIND_{ns}$ (rose), and $BUOY_{ns}$ (purple) for 10 different ocean regions (rows) over 3 different depth ranges (columns). An overview of the area boundaries for the sub-regions is shown in Figure A.16. Red dashed lines mark the four different periods of O_2 content evolution as described in Section 4.1.1.

Here, in the upper 300 m of the water column, the oxygen inventory is dominated by two key determinants (Figs. A.23 and A.24b,e,g): ventilation and remineralisation. Yet an inverse relationship is found with oxygen solubility (Fig. A.25b,e,g). This pattern changes at greater depths where, counter-intuitively, higher oxygen concentrations often coincide with higher respiration rates.

While in the tropical Pacific the El Niño-Southern Oscillation (ENSO) generates complex physical and biogeochemical dynamics that are discussed in more detail in Section 5.3, as general mechanisms, mostly in the eastern Atlantic and Pacific basins, I posit the operation of the following mechanisms: Increased wind stress may lead to increased upwelling of nutrient-rich cold waters, thereby increasing oxygen solubility. However, nutrient upwelling may simultaneously increase primary production and respiration rates, leading to oxygen depletion that outweighs the increase in oxygen solubility. Particularly in the tropics, strong stratification and relatively shallow MLDs effectively decouple surface waters from subsurface waters and limit the impact of solubility on oxygen inventory changes. This is consistent with the findings of Ridder & England (2014), who showed that the extent of global low-oxygen volume is positively correlated with the magnitude of tropical zonal wind stress. Beyond 300 m, the effect of respiration diminishes and is no longer able to cause significant changes in oxygen levels. While increased remineralisation due to increased wind stress forcing may continue to greater depths, this effect may be overshadowed by the more dominant influences of solubility in the equatorial Atlantic and Indian Oceans, and ventilation in the equatorial Pacific Ocean.

By contrast, Ridder & England (2014) showed that an increase in zonal wind stress in the equatorial Indian Ocean leads to a reduction in low-oxygen water masses. This reduction was closely linked to the Indonesian throughflow, which intensified in response to the stronger wind stress and compensated for the nutrient upwelling and increased respiration in the region. However, if this were the primary control of oxygen changes in the equatorial Pacific, an increased mean remineralisation rate would be accompanied by an increased oxygen inventory. Instead, the model simulated the opposite, which may be related to a high sensitivity of the low-oxygen zones in the Arabian Sea to fluctuations in the Indian monsoon winds (Lachkar et al. 2018). Specifically, the Arabian Sea OMZ grows under - especially summer - monsoon wind intensification, mainly ascribed to increased productivity and biological consumption (Lachkar et al. 2018). Therefore, year-to-year variability in monsoon wind strength may account for the simulated dynamics in the equatorial Indian Ocean.

However, while oxygen variability in equatorial regions is strongly influenced by year-to-year variability in wind stress, strong long-term trends remain largely absent and thus cannot explain the aforementioned, simulated increase in global oceanic oxygen inventory when the year-to-year variability in buoyancy forcing is suppressed.

Observational data show that the present-day pattern of wind stress anomalies, relative to the 1988-2015 climatology, is dominated by changes at mid to high latitudes (Johnson & Lumpkin 2022). Specifically in the SH, the westerlies - the strongest time-mean near-surface winds over the open ocean (Yu & Jin 2012) - have strengthened significantly over the Antarctic Circumpolar Current region since the 1970s (Arblaster & Meehl 2006, Thompson et al. 2011, Goyal et al. 2021, Johnson & Lumpkin 2022). A study by Getzlaff et al. (2016) investigated the consequences of these changes in wind stress on the oceanic oxygen content. They established that the strengthening of the southern westerlies corresponds to increased water formation rates for oxygen-rich deep and intermediate water masses, ultimately increasing global oxygen supply.

It can be speculated that this is the major contributor to the simulated wind stress-induced increase in oxygen in the model. The simulated spatial distribution of oxygen changes resulting from the year-to-year variability in wind stress is consistent with this notion. Specifically, the model indicates that intermediate waters (300-1000 m) between 50°S and 15°N undergo the largest wind stress-induced increases in oxygen over the period analysed (Fig. 14 [rose lines]), as anticipated from the enhanced formation rates of intermediate water masses, and subsequent equatorward transport. However, as noted in Section 5.2.1, oxygen levels in the Southern Ocean intermediate and deep water masses (south of 50°S) are only minimally affected by changes in wind stress, suggesting a low sensitivity of AABW formation to the recent strengthening of westerly winds. Furthermore, atmospheric reanalysis products indicate a poleward shift of the southern westerlies since the 1970s (Thompson & Solomon 2002; Goyal et al. 2021). This shift, which implies the movement of the sinking branch of intermediate water masses into denser waters, may have further intensified intermediate water mass formation (Lee et al. 2023), simultaneously increasing the oxygen solubility in subducted waters.

However, the anticipated increase in solubility is not simulated in the hindcast experiment (Fig. 14 [black lines]) and may have been masked by natural climate variability or changes in buoyancy forcing that generated a larger signal. As noted in section 5.2.1, in the mid-latitudes of the SH, year-to-year changes in buoyancy forcing also significantly affect local oxygen dynamics by ocean warming and freshening associated with anthropogenic climate change. In the two sensitivity experiments, this results in clearly divergent oxygen trends in the intermediate layer (Fig. 14 [rose and purple lines]), especially in the southern and equatorial Atlantic and Indian Oceans, while in the southern Pacific, wind-stress-induced O_2 increases first appear in the mid-1990s. Changes in oxygen and their underlying drivers thus constitute the balance between the two competing forcings.

5.3 Oxygen dynamics related to the El Niño-Southern Oscillation

Understanding regional oxygen dynamics in the oceans necessitates the consideration of the influence of natural climate variability. While trends in the global oxygen inventory tend to be smoothed when averaged over large spatial scales, Period iii stands out as an outlier. From 1994 to 2002, an anomalous decline in the global oxygen inventory until 1998 was followed by a rapid recovery. Consideration of oxygen trends at smaller spatial scales shows that this transient oxygen low originated mainly in the upper equatorial Pacific, with a change in mean oxygen concentration of about -3 mmol O_2 m^{-3} within a few years (Fig. 14e-1). This localised signature points to the strong El Niño conditions in the equatorial Pacific in 1997-98 as the primary trigger (Wolter & Timlin 2011), with fluctuations in wind stress found to be the main driver of this transient low.

Specifically, in the equatorial Pacific the decline was associated with a decrease in ventilation and an increase in oxygen lost by remineralisation, with an increase in the rate of remineralisation by more than 20% within 2 years (Figs. A.23 and A.24e-1). Oxygen solubility varied inversely with the oxygen inventory (Fig. A.25e-1). However, when focusing only on the eastern equatorial Pacific, this dynamic is reversed (Fig. A.18). In 1998, the eastern tropical Pacific was characterised by relatively high oxygen levels, increased ventilation, low respiratory losses, and high oxygen solubility. This reversal indicates a prevailing dipole and highlights that the dominant changes in the Pacific Ocean oxygen inventory between 15°S and 15°N are defined away from the eastern boundary.

The El Niño-Southern Oscillation (ENSO), which represents the primary mode of year-to-year climate variability, plays a central role in shaping oxygen

dynamics in the tropical Pacific (Eddebbar et al. 2017; Leung et al. 2019). During La Niña, easterly winds intensify, and sea surface temperatures in the central and eastern tropical Pacific Ocean are below average. Conversely, during El Niño, there is a weakening of the easterlies and a reduction in westward flow of warm sea surface waters, causing above-average sea surface temperatures in the central and eastern tropical Pacific (Timmermann et al. 2018). This creates a shallower thermocline in the east and a deeper thermocline in the west, establishing a zonal gradient in thermocline depth that is significantly flattened compared to neutral or La Niña conditions (Leung et al. 2019).

Leung et al. (2019) showed that this ENSO-related shift in thermocline depth (TCD) significantly influences the vertical distribution of low-oxygen layers, mainly through the vertical motion of water masses separated by well-defined thermo- and oxyclines. They find that on average, in the western basin, the TCD is about 31.5 m shallower during El Niño relative to La Niña, whilst in the eastern basin, the TCD is about 18.5 m shallower during La Niña relative to El Niño. The authors propose that as the thermocline deepens, hypoxic waters beneath the thermocline are forced downward, thereby increasing the well-oxygenated surface ocean layer. Conversely, as the thermocline shoals, hypoxic waters below the thermocline are pulled upward, compressing the oxygenated vertical space in the upper water column. This study's model results are consistent with this concept. Particularly the increase in oxygen at depths deeper than 1,000 m (Fig. 14e-3) supports the notion that during El Niño in the western Pacific, a shallower thermocline leads to the upward movement of oxygen-poor waters from deeper layers into the upper ocean.

Nonetheless, the manifestation of El Niño conditions as a global oxygen inventory low implies that there is not only a redistribution of oxygen in the ocean, but also a net loss, and the involvement of other mechanisms.

Eddebbar et al. (2017) additionally link the TCD-related oxygen redistribution to concomitant changes in air-sea oxygen exchange, showing that there is a net loss of oxygen to the atmosphere during El Niño and a net gain during La Niña, with significant accompanying changes in subsurface oxygen concentrations to depths of 400 m. The authors propose that shallower and weaker upwelling during El Niño leads to lowered O_2 under-saturation in the eastern tropical Pacific and anomalous O_2 outgassing, whereas deeper and strengthened upwelling during La Niña leads to anomalous O_2 uptake. They show that these O_2 flux anomalies are strongly localised along the eastern and central equatorial Pacific and are partly counterbalanced by a weaker response of opposite sign in the western tropical Pacific. In the west, high precipitation maintains an effective barrier through haline stratification, which typically inhibits upwelling. However, during El Niño, the shoaling of the western equatorial Pacific thermocline erodes this barrier and allows oxygen-poor water to be upwelled.

Concurrent changes in primary production further intensify oxygen depletion in the upper ocean of the western equatorial Pacific (Lehodey 2001): In these oligotrophic waters, the erosion of the barrier layer during El Niño and the entrainment of deeper waters to the surface additionally causes nutrients to be upwelled. This in turn triggers an increase in primary production and may account for the substantial increase in respiration rates simulated by the model. Conversely, in the eastern Pacific, the thickened layer of warm water and shallow upwelling disrupts the supply of nutrient-rich water to the surface, leading to reduced biological productivity and respiration (Eddebbar et al. 2017). In addition, the supply of oxygen to the eastern basin may be increased by the equatorward propagation of subtropical oxygen-rich waters that are blocked during La Niña, contributing to the increased oxygen inventory in the eastern

basin, lowered O_2 under-saturation, and anomalous O_2 outgassing (José et al. 2019).

Eddebbar et al. (2017) further show that the net surface warming of the tropical Pacific during El Niño, which suggests reduced surface oxygen solubility and hence thermal oxygen outgassing, paradoxically results in widespread anomalous oxygen uptake during El Niño. They suggest that this is due to reduced equatorial heat uptake and positive heat flux anomalies, which therefore slightly moderate the net O_2 flux.

In summary, during El Niño there is a weakening of the easterly winds and a reduction in the westward flow of warm sea surface water (Timmermann et al. 2018). The thermocline in the east deepens and shallows in the west, likely causing a vertical displacement of the closely coupled oxycline (Leung et al. 2019). In the western Pacific, the upward pull and re-entrainment of oxygen-depleted, nutrient-rich waters causes surface oxygen undersaturation (Eddebbar et al. 2017). This state is intensified by enhanced primary production and respiration (Lehodey 2001), resulting in an anomalous influx of O_2 from the atmosphere. However, this is countered by a greater oxygen outflow from the ocean to the atmosphere in the eastern and central Pacific (Eddebbar et al. 2017). Here, oxygen-depleted, nutrient-rich waters are thought to be pushed downwards (Leung et al. 2019), beyond the reach of the shallower and weaker upwelling during El Niño. Primary production and respiration are reduced, and the lowered O_2 undersaturation in the eastern tropical Pacific intensifies (Eddebbar et al. 2017). Ultimately, during El Niño, the oxygen inventory is reduced. During La Niña, the mechanisms are reversed.

5.4 Implications for future O_2 changes

Understanding past changes in the oceanic oxygen inventory is central to more reliable projections of its future fate. The analysis of hindcast simulations has provided a more detailed understanding of the forces that have shaped oceanic oxygen dynamics over the past six decades, laying the groundwork for more informed predictions of future changes. Here I discuss some of the most likely large-scale changes in buoyancy forcing and wind stress over the course of the 21st century, and their potential implications for future oxygen dynamics.

5.4.1 Trends in buoyancy forcing

As global warming continues, the changes described in more detail above - including increases in surface air temperature and ocean heat content, shifts in precipitation patterns, and changes in the Earth's cryosphere - will persist; the magnitude and duration of these ongoing changes contingent upon the specific Shared Socio-economic Pathway (SSP) scenario considered (Lee et al. 2021, and references therein).

With respect to the oceans, the concept of 'committed change' is particularly important. Because of its inherent inertia, even if global mean surface temperatures stabilise after CO_2 emissions cease, the ocean will continue to respond for centuries, producing the changes that are committed today (Plattner et al. 2008; Frölicher & Joos 2010; Gillett et al. 2011; Oschlies 2021). This is because once GHG emissions are halted, global mean surface temperatures will be largely stabilised by a balance between oceanic uptake of atmospheric CO_2 and oceanic uptake of heat, yet accompanied by increasing ocean acidification and warming (Oschlies 2021). These ongoing changes will also continue to influence related metrics such as precipitation, glacial melt, and oceanic oxygen (Marzeion et al. 2018; Douville et al. 2021; Oschlies 2021).

5.4.2 Trends in wind stress forcing

In recent decades, the most dominant change in wind stress has been recorded for the southern westerlies, which have intensified and shifted poleward,

driven by the combined effects of GHG emissions and stratospheric ozone depletion (Thompson & Solomon 2002; Arblaster & Meehl 2006; Thompson et al. 2011). While the recovery of stratospheric ozone is expected in the future by around 2060 (Dhomse et al. 2018), the poleward shift and intensification of westerly winds are projected to continue under high GHG emission scenarios (Goyal et al. 2021). However, under moderate (low) emission scenarios, GHG forcing stabilises at much lower levels and stratospheric ozone recovery is projected to largely compensate for GHG-induced changes, potentially leading to a stabilisation (weakening) of the SH surface westerlies (Goyal et al. 2021; Deng et al. 2022).

Large uncertainties remain in projections of long-term changes in the tropical Pacific under global warming. For example, greater warming in the eastern Pacific than in the western Pacific (i.e., an El Niño-like pattern) has been proposed as a result of weakened atmospheric zonal overturning circulation and trade winds under continued warming (Meehl & Washington 1996), or as a result of reduced incoming solar radiation due to stronger cloud shielding in the eastern Pacific (Vecchi et al. 2006). Alternatively, a La Niña-like pattern has been proposed in response to anthropogenic climate change, with greater warming in the western Pacific than in the eastern Pacific, and may arise from a strengthened Walker circulation (L'Heureux et al. 2013) or as an ocean dynamical feedback (Li et al. 2015), both of which are associated with enhanced upwelling of cold water in the eastern equatorial region, resulting in slower warming in the eastern compared to the western basin (L'Heureux et al. 2013). Today, there is growing evidence of long-term cooling in the eastern equatorial Pacific and warming elsewhere in the tropical Pacific (e.g., Zhang et al. 2010; Li et al. 2015; Li et al. 2019; Jiang & Zhu 2020).

The projected changes in buoyancy and wind stress forcing outlined here will translate into changes in oxygen dynamics. Potential outcomes are as follows:

1. **NADW and AMOC:** Climate models now consistently project a slowdown of the AMOC over the 21st century, with CIMP6 model projections indicating a decline that continues until about 2060, followed by stabilisation under low emissions scenarios (Weijer et al. 2020; Lee et al. 2021; Fox-Kemper et al. 2021). In the 21st century, faster warming of subpolar regions and freshening due to shifted precipitation patterns are expected to lead to more buoyant and stable water masses in subpolar latitudes and a decrease in the north-south pressure gradient; closely tied to NADW formation and AMOC strength (Fox-Kemper et al. 2021). Freshwater input from the Greenland Ice Sheet may further promote AMOC weakening in the 21st century by lowering deep winter convection and NADW formation in the Labrador Sea (Böning et al. 2016; Golledge et al. 2019). This is likely to cause an immediate, global-scale decrease in subsurface oxygen, independent of the timescales of internal transport, which would continue the buoyancy forcing-induced oxygen decrease simulated at depth. A continued reduction in NADW formation is expected to maintain the pronounced, mainly ventilation-induced decline simulated in the deep North Atlantic. In addition, the projected weakening of the AMOC is anticipated to cause a redistribution of Atlantic Ocean heat content from northern to lower latitudes (Caesar et al. 2018). Thus, while the redistribution of heat in the Atlantic may mitigate the reduction in NADW formation and the injection of newly ventilated water masses into the deep North Atlantic by slowing the warming-induced buoyancy loss (Oldenburg et al. 2021), it may lead to additional oxygen depletion in the subtropics due to faster heating and reduced oxygen solubility.
2. **AAIW and SAMW:** AAIW and SAMW ven-

tilate the upper 1,000 m of the SH subtropics and are predicted to be the largest contributors to the increase in subsurface temperatures of the SH oceans in the 21st century (Fox-Kemper et al. 2021). Since the mid-1970s, the strength of the Southern Ocean upper overturning cell has roughly doubled, mainly due to a strengthening of the SH westerlies (Lee et al. 2023), providing an important counterforce to the consequences of the changes in buoyancy forcing (Section 5.2.2). While Lee et al. (2023) projects this strengthening to continue, the attenuation of wind stress intensification by ozone recovery may mediate the strengthening of the upper Southern Ocean cell in the coming decades (Goyal et al. 2021; Deng et al. 2022). This may weaken the critical counterforce, potentially accelerating subsurface oxygen loss, mostly <1,000 m. It is also important to consider that the AAIW and SAMW are important oxygen suppliers to the equatorial OMZs (Davila et al. 2023), raising concerns about their potential to accelerate the expansion of these low-oxygen zones as formation rates slow. At the same time, however, the SAMW in particular acts as an important distributor of nutrients, especially to the low-latitude upwelling regions (Sarmiento et al. 2004), thereby inducing a negative feedback by altering net primary productivity and subsequent respiration, which may be particularly important at the respiration-sensitive low latitudes.

3. **AABW:** Instead, the lower Southern Ocean overturning cell has been weakening since the mid-1970s due to a reduction in AABW formation (Section 5.2.1). Models indicate that this decline in AABW formation is set to persist with continued warming, and may approach near-total cessation by the middle (Lago & England 2019), or end of this century (Chamberlain et al. 2019; Holzer et al. 2020) under the high emissions scenario (RCP8.5). This suggests a continued decline in ventilation and a buoyancy forcing-induced decrease in oxygen in the lower Southern Ocean overturning cell, the magnitude of which is strongly dependent on the emissions scenario.

4. **Tropical Pacific:** The greater warming in the western tropical Pacific than in the eastern tropical Pacific may lead to a sustained shift towards conditions closer to the La Niña state (L'Heureux et al. 2013; Li et al. 2019). While, by the dynamics described in Section 5.3, this could lead to additional oxygen losses in the eastern Pacific upwelling regions, on a global scale a net increase in oxygen inventory is expected due to the simulated dominance of western basin oxygen changes over zonally averaged oxygen trends in response to an ENSO phase shift in the model. However, the future development of El Niño or La Niña-like conditions under global warming, and particularly the consequences for oxygen levels, remains subject of ongoing debate (Li et al. 2019; Jiang & Zhu 2020). Although historical patterns and mechanisms provide valuable insights, the interplay of natural variability and anthropogenic influences on tropical Pacific climate and oxygen dynamics requires further study to better understand and predict future climate trends.

5. **Subtropical gyres:** A recent study by Yang et al. (2016) has identified a consistent poleward migration of the major subtropical gyres, possibly driven by the poleward shift of the extratropical atmospheric circulation attributed to global warming. It is suggested that this ocean gyre migration is likely to persist in the face of ongoing climate warming (Fox-Kemper et al. 2021). This shift has the potential to increase the transit time of water parcels, potentially increasing the net loss of oxygen before

being re-entrained into the surface mixed layer. This effect is expected to be most pronounced in the low- to mid-latitude subsurface ocean.

5.5 Model-observation mismatch since the early 2000s

It must be cautioned that ORCA025-MOPS, like most state-of-the-art models, underestimates the severity of deoxygenation in recent years (Oschlies et al. 2017). While the trends up to the early 2000s are reasonably well captured by the model, it significantly underestimates the subsequent acceleration of oxygen depletion, by a factor of about three compared to both Ito-17 and GOBAI-O_2. The model performs reasonably well in reproducing patterns of variability on both interannual and decadal (to multidecadal) time scales, both in magnitude and spatial distribution. However, it fails to reproduce the magnitude and spatial distribution of observed long-term trends, suggesting that the model may be proficient in simulating short-term processes, but lacks accuracy in capturing longer-term changes.

Figure A.13 shows that the model is unable to reproduce the strong negative trends observed in many oceanic regions, including the North Pacific, the tropical Atlantic and Pacific Oceans, and the Southern Ocean. This underestimation may be attributed to a spectrum of factors, including deficiencies in the representation of mixing and transport processes (e.g., due to inadequate model resolution), model stoichiometry, or the misrepresentation or neglect of critical biogeochemical mechanisms and feedbacks (Oschlies et al. 2018). Additional anthropogenic forcings may also be important but are neglected in the model, including increasing atmospheric nutrient deposition and the effects of industrial fishery, which may affect marine biogeochemistry through additional nutrient fluxes, and perturbations of the higher trophic level structure with potential downstream effects on lower trophic level organisms (Oschlies et al. 2018). While the sensitivity of oxygen in the tropical thermocline to changes in many of these factors was found to be relatively small compared to the model-data mismatch, differences in wind forcing were found to produce the largest shifts in simulated oxygen trends (Oschlies et al. 2018).

This raises the question of whether the (model response to) strengthened wind forcing is overly strong. However, even the complete cancellation of changes in wind stress does not bring the simulated trends significantly closer to the observational estimates (Fig. 15). Only at the very end of the simulation does the oxygen inventory simulated by the buoyancy forcing experiment (i.e., no wind stress strengthening) approach a rate of change similar to that estimated by GOBAI-O_2. However, clearly this rate acceleration towards the end of the simulation may be a short-lived phase induced, for example, by natural climate variability, as has been repeatedly simulated throughout the period analysed. Thus, while the potential impact of overestimated (model response to) wind stress intensification on oxygen levels is suspected to be several orders of magnitude too small to account for the underestimated O_2 decrease, it must be acknowledged that misrepresentations in wind stress forcing may still generate *spatial* discrepancies between modelled and observed trends.

For example, in the tropical Pacific, where a strong relationship between wind stress forcing and oxygen trends has been found, easterly winds have intensified over the past two decades in association with La Niña-like cooling in the eastern Pacific (L'Heureux et al. 2013; Takahashi & Watanabe 2016). This study's results, consistent with Ridder & England (2014), indicate a dipole-like signature of changes in wind forcing on oxygen levels in the eastern versus western parts of tropical ocean basins, with the La Niña phase accompanied by increased O_2 loss in the eastern Pacific basin (Section 5.3). Thus, a misrepresented strengthening of easterly winds and the cold tongue

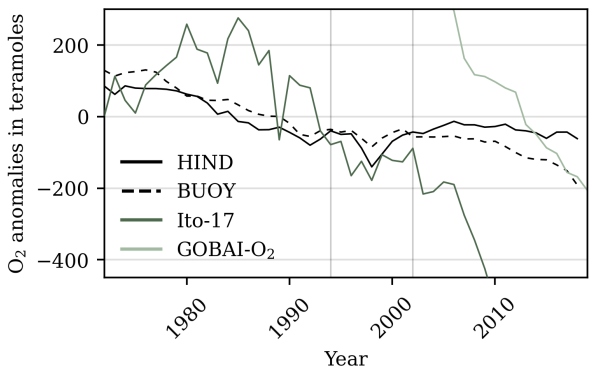

Figure 15: Annual time series of upper 1,000 m O_2 inventory anomalies in ORCA025-MOPS $HIND_{ns}$ (solid black) and $BUOY_{ns}$ (dashed black), Ito-17 (dark green; Ito et al. 2017), and GOBAI-O_2 (light green; Sharp et al. 2022a). For details of the observations, refer to Section 2.4. Grey vertical lines mark the four different periods of O_2 content evolution as described in Section 4.1.1. Please note that all data are mean centred. For mean-centering, the long-term mean calculated for the full time span of each dataset was used.

mode could explain the neglected additional O_2 loss in the eastern tropical Pacific in the model, especially given the inconsistencies in wind patterns between JRA55-do and observations in the tropical oceans (Taboada et al. 2019). Globally, in contrast, this is unlikely to explain the underestimation of deoxygenation, as extreme events such as the 1997-1998 El Niño have demonstrated the dominance of western basin oxygen changes over zonally averaged oxygen trends in response to wind forcing in the model (Section 5.3). This hypothesis, however, is largely based on the interpretation of a single extreme event and requires further investigation.

In the Southern Ocean, ORCA025-MOPS shows relatively little influence of wind stress on local oxygen dynamics. Instead, the Southern Ocean is largely influenced by meltwater dynamics (Lee et al. 2023). While Bronselaer et al. (2020) demonstrated the importance of accurately integrating meltwater forcing to adequately model the observed large-scale deoxygenation in the Southern Ocean, models commonly fail to incorporate changes in meltwater inflow from the Antarctic ice sheet with sufficient accuracy (Bronselaer et al. 2018). The meltwater influx has accelerated in recent decades (Bronselaer et al. 2020; Lee et al. 2023), and its misrepresentation may also contribute to the underestimation of oxygen depletion in ORCA025-MOPS. It should also be noted that in the Southern Ocean the *variability* of oxygen changes is underestimated by the model, suggesting that important dynamical processes have been omitted. For example, eddies play a particularly important role in the Southern Ocean (Rintoul & Naveira Garabato 2013). While a horizontal resolution of 0.25° x 0.25° is sufficient to resolve the mesoscale eddy field in most parts of the lower and mid-latitudes, mesoscale eddies at high latitudes can be up to 10 km in size, allowing only the larger eddies to be explicitly resolved (Chelton et al. 2011; Hallberg 2013). This can lead to additional uncertainties and unresolved processes that may contribute significantly to the oxygen dynamics in the Southern Ocean.

The central role of eddies in modulating oxygen dynamics has also been demonstrated for the northern Pacific. Specifically, for the Gulf of Alaska (where the largest model-observation discrepancy was found within the Pacific [<300 m]), Crawford et al. (2007) show that eddies dominate the distribution of phytoplankton in the surface pelagic waters. The authors demonstrate that while primary productivity in the HNLC waters of the Gulf of Alaska is typically highly iron-limited, eddies near the continental margin entrain nutrient-rich coastal waters into their outer rings, carrying them into the basin interior where these iron-rich waters directly increase primary production. As these eddies decay after propagating into the pelagic regions, they also transport nutrients and iron into the surface mixed layer, making them available for wind-driven mixing (Crawford et al. 2007). The importance of resolving eddies for the accurate simulation of phytoplankton is not unique to the

Gulf of Alaska, but is also evident in other parts of the North Pacific Basin (Mizobata & Saitoh 2004; Xiu & Chai 2020), and may contribute to the mismatches evident in the northern Pacific.

At coarser scales, there are additionally indications of overly high ventilation in the model. Inspection of MLD biases compared to ARGO observations suggested significant overestimation of MLDs in subpolar latitudes of the North Atlantic. This overestimation may intensify the injection of oxygen into the deep ocean, leading to overestimated O_2 concentrations, particularly at depth. Furthermore, a robust relationship between OHC and oxygen content was found (Fig. 14), as has been shown by Bopp et al. (2013) and Ito et al. (2017). However, compared to observation-based estimates (e.g., Levitus et al. 2012; Cheng et al. 2017), ORCA025-MOPS only simulates about ¾ of the recent rise in global OHC, which most likely contributes significantly to the observed discrepancy by the mechanisms outlined above.

The model-observation mismatch underscores the need for improvements in ocean biogeochemical models. Key areas for improvement include better representation of ocean heat uptake and storage, wind stress and meltwater forcing, stratification, and overturning processes. Beyond this, an eddy-resolving model resolution, which also explicitly resolves the smaller scale eddies at higher latitudes, may contribute to a more accurate representation of both oxygen variability and long-term trends. Unfortunately, for many of these metrics, including oxygen itself, only sparse observations with large uncertainties are presently available (e.g., Cheng et al. 2017; Long et al. 2016; Ito et al. 2017). Continuous measurements of these metrics will therefore be crucial for validating and improving the accuracy of models and reanalyses, ultimately contributing to a more accurate understanding of oxygen dynamics in the ocean.

6 Conclusions

This study demonstrates the complexity of mechanisms that underlie the global and regional dynamics of oxygen change. Analysing six decades of simulated global oceanic oxygen content, a negative trend in the global oceanic oxygen inventory was found that began in the 1970s and intensified in the early 2000s (Fig. 5). This trend is primarily attributed to changes in buoyancy forcing in the model, driven by shifts in air temperature and precipitation (Fig. 9 [purple lines]). However, over the past five decades, changes in wind stress have acted continuously to mitigate the dominant buoyancy-driven decline in oceanic O_2 content on a global scale (Fig. 9 [rose lines]). Yet the specific regions in which these forces induce changes in oxygen, and the pathways through which they operate, vary considerably (Fig. 14).

In equatorial regions, especially in the upper ocean, wind stress is shown to be the primary driver of oxygen dynamics. In contrast, in the deep-water formation regions of NADW and AABW, year-to-year variability in buoyancy forcing is the key driver of local, especially deep ocean oxygen variability and long-term trends, and is suspected to be related to the widespread buoyancy-induced oxygen loss in the deep ocean, likely in connection with a weakening in NADW formation and AMOC strength. In the mid-latitudes of the SH, both year-to-year changes in buoyancy forcing and wind stress contribute to changes in oxygen content, although with offsetting effects. Here, surface warming and freshening over the past decades likely have increased stratification, reduced oxygen solubility, and slowed the rate of water mass formation. This decline in oxygen inventory due to year-to-year variability in buoyancy forcing has been simulated at intermediate depths in the South Indian Ocean since the late 1960s, and in the South Atlantic and Pacific Oceans since the mid-1970s. However, these changes have been partially offset by the intensification and poleward shift

of westerly winds due to the combined effects of greenhouse gas emissions and stratospheric ozone depletion (Arblaster & Meehl 2006; Thompson et al. 2011; Goyal et al. 2021). While the strengthening of the winds is likely to be responsible for mitigating any ventilation-induced oxygen depletion by promoting water mass formation, the northward shift is likely to have displaced the sinking branch into colder waters (Lee et al. 2023), additionally counteracting the solubility effect of anthropogenic climate warming.

As stratospheric ozone is projected to recover around 2060 (Dhomse et al. 2018), the trend in wind intensification may weaken. Under moderate to low emissions scenarios, ozone recovery may compensate for GHG-induced changes, potentially stabilising or weakening the SH surface westerlies that currently counteract the simulated declining oxygen trend due to changes in buoyancy forcing (Goyal et al. 2021; Deng et al. 2022). This scenario is a cause for concern because even if greenhouse gas emissions cease and surface temperatures stabilise, the ocean will continue to warm for centuries, interacting with parameters such as precipitation, glacial melt, and ultimately ocean dynamics (Plattner et al. 2008; Frölicher & Joos 2010; Gillett et al. 2011; Oschlies 2021). Consequently, it is expected that as wind stress intensification diminishes in the future, oxygen loss may accelerate, particularly in intermediate waters.

In addition, these intermediate waters are important oxygen suppliers to the equatorial OMZs (Davila et al. 2023). This raises concerns about their potential to accelerate the expansion of these low-oxygen zones, with far-reaching ecological consequences. However, it is important to recognise that these intermediate waters also deliver nutrients to the low latitudes (Sarmiento et al. 2004), and any reduction in their formation may interfere with nutrient supply, affecting primary production and respiration. Thus, these regions are expected to undergo significant changes in the future, although the precise mechanisms require further study, emphasising the need for continued and accessible O_2 observations.

Importantly, this analysis highlights the key role of year-to-year variability in wind stress during the study period in counteracting the buoyancy-induced oxygen depletion especially at mid-depth, and underlines the need for accurate representation of wind stress changes in climate models when assessing past and future deoxygenation and its ecological consequences. By identifying regional structures of dominant influences, this analysis contributes to a much-needed improved mechanistic understanding of O_2 changes, and emphasises the complexity of our changing oceans that must be recognised when anticipating future global and regional O_2 inventory changes, and the potential consequences for marine ecosystems.

Box 6 Sections 5 and 6: Key takeaways

1. A global ocean biogeochemical model was used to understand the temporal and regional patterns of oxygen dynamics and drivers over the period 1958-2018. [Section 1.2]
2. In the first decade of the simulation period, the global oceanic O_2 inventory increased. After the 1970s, a global decline in the O_2 inventory was simulated, which intensified in the early 2000s. [Fig. 5; Section 4.1]
3. The model agreed with observations until the early 2000s, but thereafter showed a three-fold lower rate of decline. To address the mismatch, improvements in ocean biogeochemical models are needed, specifically [Section 5.5]:
    - 3.1 Improved representation of ocean heat uptake and storage, wind stress and meltwater forcing, stratification and overturning processes.
    - 3.2 Continuous measurements of these parameters to validate and improve the accuracy of models and reanalyses.
    - 3.3 An model resolution that explicitly resolves the smaller scale eddies at higher latitudes.
4. On a global scale, the decline was mainly attributed to changes in buoyancy forcing, but was continually mitigated by increasing wind stress, which counteracted oxygen decreases foremost at intermediate depths. The specific regions in which these forces drove oxygen changes varied, however [Figs. 9, 11, and 14; Sections 4.3.1 and 5.2]:
    - 4.1 In the equatorial regions, especially in the upper ocean, wind stress dominated oxygen dynamics but caused no clear long-term trend. [Section 5.2.2]
    - 4.2 In the deep-water formation regions of NADW and AABW, buoyancy forcing dominated deep ocean O_2 dynamics, with decreases in ventilation in the North Atlantic likely attributed to changes in freshwater fluxes and reduced formation rates of NADW. [Section 5.2.1]
    - 4.3 In the mid-latitudes of the Southern Hemisphere, both year-to-year changes in buoyancy forcing and wind stress contributed to oxygen dynamics, although with opposing effects [Sections 5.2.1 and 5.2.2]:
        - 4.3.1 Surface warming and freshening over the past decades likely increased stratification, reduced oxygen solubility, and slowed the rate of water mass formation.
        - 4.3.2 The intensification and poleward shift of westerly winds counteracted these trends.
5. Projected stratospheric ozone recovery around 2060 may weakens the wind stress intensification, potentially accelerating oxygen loss in the future, particularly in intermediate waters, with potential downstream consequences also in the tropical OMZs. [Section 5.4]
6. Accurate representation of wind stress changes is crucial when modelling past and future deoxygenation and its ecological consequences. [Section 6]

References

1. Arblaster, J. M. & Meehl, G. A. Contributions of external forcings to Southern Annular Mode trends. *Journal of Climate* **19,** 2896–2905 (2006).
2. Arrigo, K. R., van Dijken, G. & Pabi, S. Impact of a shrinking Arctic ice cover on marine primary production. *Geophysical Research Letters* **35,** L19603 (2008).
3. Bakker, P. et al. Fate of the Atlantic Meridional Overturning Circulation: Strong decline under continued warming and Greenland melting. *Geophysical Research Letters* **43,** 12, 252–12, 260 (2016).
4. Bao, Y. & Li, Y. Simulations of dissolved oxygen concentration in CMIP5 Earth system models. *Acta Oceanologica Sinica* **35,** 28–37 (2016).
5. Basterretxea, G., Font-Muñoz, J. S., Hernández-Carrasco, I. & Sañudo-Wilhelmy, S. Global variability of high nutrient low chlorophyll regions using neural networks and wavelet coherence analysis. preprint (2022).
6. Bianchi, D., Galbraith, E. D., Carozza, D. A., Mislan, K. A. S. & Stock, C. A. Intensification of open-ocean oxygen depletion by vertically migrating animals. *Nature Geoscience* **6,** 545–548 (2013).
7. Bianchi, D. & Mislan, K. A. S. Global patterns of diel vertical migration times and velocities from acoustic data. *Limnology and Oceanography* **61,** 353–364 (2015).
8. Bindoff, N. L. et al. in *IPCC Special Report on the Ocean and Cryosphere in a Changing Climate* (eds Pörtner, H. O. et al.) 447–587 (Cambridge University Press, Cambridge, UK and New York, NY, USA, 2019).
9. Bograd, S. J. et al. Climate change impacts on Eastern Boundary Upwelling Systems. *Annual Review of Marine Science* **15,** 303–328 (2023).
10. Böning, C. W., Behrens, E., Biastoch, A., Getzlaff, K. & Bamber, J. L. Emerging impact of Greenland meltwater on deepwater formation in the North Atlantic Ocean. *Nature Geoscience* **9,** 523–527 (2016).
11. Bopp, L. et al. Multiple stressors of ocean ecosystems in the 21st century: projections with CMIP5 models. *Biogeosciences* **10,** 6225–6245 (2013).
12. Bopp, L. et al. Potential impact of climate change on marine export production. *Global Biogeochemical Cycles* **15,** 81–99 (2001).
13. Brandt, P. et al. On the role of circulation and mixing in the ventilation of oxygen minimum zones with a focus on the eastern tropical North Atlantic. *Biogeosciences* **12,** 489–512 (2015).
14. Brewer, P. G. & Peltzer, E. T. Depth perception: the need to report ocean biogeochemical rates as functions of temperature, not depth. *Philosophical Transactions of the Royal Society A: Mathematical, Physical and Engineering Sciences* **375,** 20160319 (2017).
15. Bristow, L. A., Mohr, W., Ahmerkamp, S. & Kuypers, M. M. M. Nutrients that limit growth in the ocean. *Current Biology* **27,** R474–R478 (2017).
16. Bronselaer, B. et al. Change in future climate due to Antarctic meltwater. *Nature* **564,** 53–58 (2018).
17. Bronselaer, B. et al. Importance of wind and meltwater for observed chemical and physical changes in the Southern Ocean. *Nature Geoscience* **13,** 35–42 (2020).

18. Browning, T. J. & Moore, C. M. Global analysis of ocean phytoplankton nutrient limitation reveals high prevalence of co-limitation. *Nature Communications* **14** (2023).

19. Browning, T. J. et al. Persistent equatorial Pacific iron limitation under ENSO forcing. *Nature* **621,** 330–335 (Aug. 2023).

20. Burmeister, K., Lübbecke, J. F., Brandt, P. & Duteil, O. Interannual variability of the Atlantic North Equatorial Undercurrent and its impact on oxygen. *Journal of Geophysical Research: Oceans* **124,** 2348–2373 (2019).

21. Cabré, A., Marinov, I., Bernardello, R. & Bianchi, D. Oxygen minimum zones in the tropical Pacific across CMIP5 models: mean state differences and climate change trends. *Biogeosciences* **12,** 5429–5454 (2015).

22. Caesar, L., Rahmstorf, S., Robinson, A., Feulner, G. & Saba, V. Observed fingerprint of a weakening Atlantic Ocean overturning circulation. *Nature* **556,** 191–196 (2018).

23. Chamberlain, M. A., Matear, R. J., Holzer, M., Bi, D. & Marsland, S. J. Transport matrices from standard ocean-model output and quantifying circulation response to climate change. *Ocean Modelling* **135,** 1–13 (2019).

24. Chelton, D. B., Schlax, M. G. & Samelson, R. M. Global observations of nonlinear mesoscale eddies. *Progress in Oceanography* **91,** 167–216 (2011).

25. Cheng, L., Trenberth, K. E., Fasullo, J., Boyer, T., Abraham, J. & Zhu, J. Improved estimates of ocean heat content from 1960 to 2015. *Science Advances* **3,** e1601545 (2017).

26. Cheng, L. et al. Past and future ocean warming. *Nature Reviews Earth & Environment* **3,** 776–794 (2022).

27. Chien, C. et al. FOCI-MOPS v1 - integration of marine biogeochemistry within the Flexible Ocean and Climate Infrastructure version 1 (FOCI 1) earth system model. *Geoscientific Model Development* **15,** 5987–6024 (2022).

28. Cooley, S. et al. in *Climate Change 2022: Impacts, Adaptation and Vulnerability* (eds Pörtner, H. O. et al.) 379–550 (Cambridge University Press, Cambridge, UK and New York, NY, USA, 2022).

29. Couespel, D., Lévy, M. & Bopp, L. Major contribution of reduced upper ocean oxygen mixing to global ocean deoxygenation in an earth system model. *Geophysical Research Letters* **46,** 12239–12249 (2019).

30. Crawford, W. R., Brickley, P. J. & Thomas, A. C. Mesoscale eddies dominate surface phytoplankton in northern Gulf of Alaska. *Progress in Oceanography* **75,** 287–303 (2007).

31. Davila, X., Olsen, A., Lauvset, S. K., McDonagh, E. L., Brakstad, A. & Gebbie, G. On the origins of open ocean oxygen minimum zones. *Journal of Geophysical Research: Oceans* **128,** e2023JC019677 (2023).

32. Deng, K., Azorin-Molina, C., Yang, S., Hu, C., Zhang, G., Minola, L. & Chen, D. Changes of Southern Hemisphere westerlies in the future warming climate. *Atmospheric Research* **270,** 106040 (2022).

33. Dhomse, S. S. et al. Estimates of ozone return dates from Chemistry-Climate Model Initiative simulations. *Atmospheric Chemistry and Physics* **18,** 8409–8438 (2018).

34. Di Lorenzo, E. et al. North Pacific Gyre Oscillation links ocean climate and ecosystem change. *Geophysical Research Letters* **35.** L08607 (2008).

35. Douville, H. et al. in *Climate Change 2021: The Physical Science Basis. Contribution of Working Group I to the Sixth Assessment Report of the Intergovernmental Panel on Climate Change* (eds Masson-Delmotte, V. et al.) 1055–1210 (Cambridge University Press, Cambridge, United Kingdom and New York, NY, USA, 2021).

36. Durack, P. J. & Wijffels, S. E. Fifty-year trends in global ocean salinities and their relationship to broad-scale warming. *Journal of Climate* **23,** 4342–4362 (2010).

37. Duteil, O., Oschlies, A. & Böning, C. W. Pacific Decadal Oscillation and recent oxygen decline in the eastern tropical Pacific Ocean. *Biogeosciences* **15,** 7111–7126 (2018).

38. Eddebbar, Y. A., Long, M. C., Resplandy, L., Rödenbeck, C., Rodgers, K. B., Manizza, M. & Keeling, R. F. Impacts of ENSO on air-sea oxygen exchange: Observations and mechanisms. *Global Biogeochemical Cycles* **31,** 901–921 (2017).

39. England, M. H. & Rahmstorf, S. Sensitivity of ventilation rates and radiocarbon uptake to subgrid-scale mixing in ocean models. *Journal of Physical Oceanography* **29,** 2802–2828 (1999).

40. Espinoza-Morriberón, D. et al. Oxygen variability during ENSO in the tropical south eastern Pacific. *Frontiers in Marine Science* **5** (2019).

41. Fox-Kemper, B. et al. in *Climate Change 2021: The Physical Science Basis. Contribution of Working Group I to the Sixth Assessment Report of the Intergovernmental Panel on Climate Change* (eds Masson-Delmotte, V. et al.) 1211–1362 (Cambridge University Press, Cambridge, United Kingdom and New York, NY, USA, 2021).

42. Frölicher, T. L. & Joos, F. Reversible and irreversible impacts of greenhouse gas emissions in multi-century projections with the NCAR global coupled carbon cycle-climate model. *Climate Dynamics* **35,** 1439–1459 (2010).

43. Frölicher, T. L., Joos, F., Plattner, G. K., Steinacher, M. & Doney, S. C. Natural variability and anthropogenic trends in oceanic oxygen in a coupled carbon cycle-climate model ensemble. *Global Biogeochemical Cycles* **23,** GB1003 (2009).

44. Garcia, H. E. & Gordon, L. I. Oxygen solubility in seawater: Better fitting equations. *Limnology and Oceanography* **37,** 1307–1312 (1992).

45. Garcia, H. E. et al. World Ocean Atlas 2013, Volume 3: Dissolved oxygen, apparent oxygen utilization, and oxygen saturation. *NOAA Atlas NESDIS* **75** (eds Levitus, S. & Mishonov, A.) 27 pp. (2013).

46. Garcia, H. E. et al. World Ocean Atlas 2013, Volume 3: Dissolved oxygen, apparent oxygen utilization, and oxygen saturation. *NOAA Atlas NESDIS* **75.** Ed. by S. Levitus and A. Mishonov. 27 pp. (2014).

47. Garcia, H. E. et al. World Ocean Atlas 2013, Volume 4: Dissolved inorganic nutrients (phosphate, nitrate, silicate). *NOAA Atlas NESDIS* **76.** Ed. by S. Levitus and A. Mishonov. 25 pp. (2014).

48. Garcia, H. E. et al. World Ocean Atlas 2018, Volume 3: Dissolved oxygen, apparent oxygen utilization, and oxygen saturation. *NOAA Atlas NESDIS* **15** (ed Mishonov, A.) 38 pp. (2019).

49. Garcia, N. S., Sexton, J., Riggins, T., Brown, J., Lomas, M. W. & Martiny, A. C. High variability in cellular stoichiometry of carbon, nitrogen, and phosphorus within classes of marine eukaryotic phytoplankton under sufficient nutrient conditions. *Frontiers in Microbiology* **9** (2018).

50. Garcia-Soto, C. et al. An overview of ocean climate change indicators: sea surface temperature, ocean heat content, ocean pH, dissolved oxygen concentration, Arctic sea ice extent, thickness and volume, sea level and strength of the AMOC (Atlantic Meridional Overturning Circulation). *Frontiers in Marine Science* **8** (2021).

51. Getzlaff, J., Dietze, H. & Oschlies, A. Simulated effects of southern hemispheric wind changes on the Pacific oxygen minimum zone. *Geophysical Research Letters* **43,** 728–734 (2016).

52. Gillett, N. P., Arora, V. K., Zickfeld, K., Marshall, S. J. & Merryfield, W. J. Ongoing climate change following a complete cessation of carbon dioxide emissions. *Nature Geoscience* **4,** 83–87 (2011).

53. Golledge, N. R., Keller, E. D., Gomez, N., Naughten, K. A., Bernales, J., Trusel, L. D. & Edwards, T. L. Global environmental consequences of twenty-first-century ice-sheet melt. *Nature* **566,** 65–72 (2019).

54. Goyal, R., Sen Gupta, A., Jucker, M. & England, M. H. Historical and projected changes in the Southern Hemisphere surface westerlies. *Geophysical Research Letters* **48,** e2020GL090849 (2021).

55. Grégoire, M., Gilbert, D., Oschlies, A. & Rose, K. in *Ocean deoxygenation: Everyone's problem - Causes, impacts, consequences and solutions* (eds Laffoley, D. & Baxter, J. M.) 1–21 (Gland, Switzerland: IUCN, 2019).

56. Grégoire, M. et al. A global ocean oxygen database and atlas for assessing and predicting deoxygenation and ocean health in the open and coastal ocean. *Frontiers in Marine Science* **8** (2021).

57. Gruber, N. et al. Trends and variability in the ocean carbon sink. *Nature Reviews Earth & Environment* **4,** 119–134 (2023).

58. Hallberg, R. Using a resolution function to regulate parameterizations of oceanic mesoscale eddy effects. *Ocean Modelling* **72,** 92–103 (2013).

59. Hauck, J. et al. Consistency and challenges in the ocean carbon sink estimate for the global carbon budget. *Frontiers in Marine Science* **7** (2020).

60. Holling, C. S. & Buckingham, S. A behavioral model of predator-prey functional responses. *Behavioral Science* **21,** 183–195 (1976).

61. Holte, J. & Talley, L. D. A new algorithm for finding mixed layer depths with applications to Argo data and subantarctic mode water formation. *Journal of Atmospheric and Oceanic Technology* **26,** 1920–1939 (2009).

62. Holte, J., Talley, L. D., Gilson, J. & Roemmich, D. An Argo mixed layer climatology and database. *Geophysical Research Letters* **44,** 5618–5626 (2017).

63. Holzer, M., Chamberlain, M. A. & Matear, R. J. Climate-driven changes in the ocean's ventilation pathways and time scales diagnosed from transport matrices. *Journal of Geophysical Research: Oceans* **125,** e2020JC016414 (2020).

64. Ilıcak, M. et al. An assessment of the Arctic Ocean in a suite of interannual CORE-II simulations. Part III: Hydrography and fluxes. *Ocean Modelling* **100,** 141–161 (2016).

65. Ito, T., Minobe, S., Long, M. C. & Deutsch, C. Upper ocean O_2 trends: 1958-2015. *Geophysical Research Letters* **44,** 4214–4223 (2017).

66. Jiang, N. & Zhu, C. Tropical Pacific cold tongue mode triggered by enhanced warm pool convection due to global warming. *Environmental Research Letters* **15,** 054015 (2020).

67. in. *State of the Climate in 2021* (eds Johnson, G. C. & Lumpkin, R. L.) 8, S143–S191 (2022).

68. José, Y. S., Stramma, L., Schmidtko, S. & Oschlies, A. ENSO-driven fluctuations in oxygen supply and vertical extent of oxygen-poor waters in the oxygen minimum zone of the Eastern Tropical South Pacific. preprint (2019).

69. Keeling, R. F., Körtzinger, A. & Gruber, N. Ocean deoxygenation in a warming world. *Annual Review of Marine Science* **2,** 199–229 (2010).

70. Kim, S. U. & Kim, K. Y. Impact of climate change on the primary production and related biogeochemical cycles in the coastal and sea ice zone of the Southern Ocean. *Science of The Total Environment* **751,** 141678 (2021).

71. Koelling, J., Atamanchuk, D., Karstensen, J., Handmann, P. & Wallace, D. W. R. Oxygen export to the deep ocean following Labrador Sea Water formation. *Biogeosciences* **19,** 437–454 (2022).

72. Kriest, I. & Oschlies, A. MOPS-1.0: towards a model for the regulation of the global oceanic nitrogen budget by marine biogeochemical processes. *Geoscientific Model Development* **8,** 2929–2957 (2015).

73. L'Heureux, M. L., Lee, S. & Lyon, B. Recent multidecadal strengthening of the Walker circulation across the tropical Pacific. *Nature Climate Change* **3,** 571–576 (2013).

74. Lachkar, Z., Lévy, M. & Smith, S. Intensification and deepening of the Arabian Sea oxygen minimum zone in response to increase in Indian monsoon wind intensity. *Biogeosciences* **15,** 159–186 (2018).

75. Lago, V. & England, M. H. Projected slowdown of Antarctic Bottom Water formation in response to amplified meltwater contributions. *Journal of Climate* **32,** 6319–6335 (2019).

76. Lauvset, S. K. et al. A new global interior ocean mapped climatology: the 1°x1° GLODAP version 2. *Earth System Science Data* **8,** 325–340 (2016).

77. Lee, J. Y. et al. in *Climate Change 2021: The Physical Science Basis. Contribution of Working Group I to the Sixth Assessment Report of the Intergovernmental Panel on Climate Change* (eds Masson-Delmotte, V. et al.) 553–672 (Cambridge University Press, Cambridge, United Kingdom and New York, NY, USA, 2021).

78. Lee, S. K. et al. Human-induced changes in the global meridional overturning circulation are emerging from the Southern Ocean. *Communications Earth & Environment* **4** (2023).

79. Lehodey, P. The pelagic ecosystem of the tropical Pacific Ocean: dynamic spatial modelling and biological consequences of ENSO. *Progress in Oceanography* **49,** 439–468 (2001).

80. Leung, S., Thompson, L., McPhaden, M. J. & Mislan, K. A. S. ENSO drives near-surface oxygen and vertical habitat variability in the tropical Pacific. *Environmental Research Letters* **14,** 064020 (2019).

81. Levin, L. A. Manifestation, drivers, and emergence of open ocean deoxygenation. *Annual Review of Marine Science* **10,** 229–260 (2018).

82. Levitus, S. Introduction. Vol. 1, World Ocean Database 1998. *NOAA Atlas NESDIS* **18.** 346 pp. (1998).

83. Levitus, S. et al. World ocean heat content and thermosteric sea level change (0–2000 m), 1955–2010. *Geophysical Research Letters* **39,** L10603 (2012).

84. Li, Y., Li, J., Zhang, W., Zhao, X., Xie, F. & Zheng, F. Ocean dynamical processes associated with the tropical Pacific cold tongue mode. *Journal of Geophysical Research: Oceans* **120,** 6419–6435 (2015).

85. Li, Y. et al. Long-term trend of the tropical Pacific trade winds under global warming and its causes. *Journal of Geophysical Research: Oceans* **124,** 2626–2640 (2019).

86. Llort, J., Lévy, M., Sallée, J. B. & Tagliabue, A. Nonmonotonic response of primary production and export to changes in mixed-layer depth in the Southern Ocean. *Geophysical Research Letters* **46,** 3368–3377 (2019).

87. Locarnini, R. A. et al. World Ocean Atlas 2018, Volume 1: Temperature. *NOAA Atlas NESDIS* **81** (ed Mishonov, A.) 52 pp. (2019).

88. Long, M. C., Deutsch, C. & Ito, T. Finding forced trends in oceanic oxygen. *Global Biogeochemical Cycles* **30,** 381–397 (2016).

89. Madec, G. & the NEMO team. NEMO ocean engine. *Note du Pôle de modélisation de l'Institut Pierre-Simon Laplace (IPSL) No 27.* ISSN: 1288-1619 (2016).

90. Marsay, C. M., Sanders, R. J., Henson, S. A., Pabortsava, K., Achterberg, E. P. & Lampitt, R. S. Attenuation of sinking particulate organic carbon flux through the mesopelagic ocean. *Earth, Atmospheric, and Planetary Sciences* **112,** 1089–1094 (2015).

91. Martiny, A. C., Pham, C. T. A., Primeau, F. W., Vrugt, J. A., Moore, J. K., Levin, S. A. & Lomas, M. W. Strong latitudinal patterns in the elemental ratios of marine plankton and organic matter. *Nature Geoscience* **6,** 279–283 (2013).

92. Marzeion, B., Kaser, G., Maussion, F. & Champollion, N. Limited influence of climate change mitigation on short-term glacier mass loss. *Nature Climate Change* **8,** 305–308 (2018).

93. McGillicuddy, D. J. Mechanisms of physical-biological-biogeochemical interaction at the oceanic mesoscale. *Annual Review of Marine Science* **8,** 125–159 (2016).

94. Meehl, G. A. & Washington, W. M. El Niño-like climate change in a model with increased atmospheric CO_2 concentrations. *Nature* **382,** 56–60 (1996).

95. Melin, F. *GMIS - MODIS-AQUA Monthly climatology sea surface Chlorophyll-a concentration (9km) in* $mg.m^{-3}$ data set. European Commission, Joint Research Centre (JRC) (2013). `http://data.europa.eu/89h/51b9459f-aa6c-4160-9754-3e203c9c99b8`.

96. Mizobata, K. & Saitoh, S.-i. Variability of Bering Sea eddies and primary productivity along the shelf edge during 1998–2000 using satellite multisensor remote sensing. *Journal of Marine Systems* **50,** 101–111 (2004).

97. Montes, E., Muller-Karger, F. E., Cianca, A., Lomas, M. W., Lorenzoni, L. & Habtes, S. Decadal variability in the oxygen inventory of North Atlantic subtropical underwater captured by sustained, long-term oceanographic time series observations. *Global Biogeochemical Cycles* **30,** 460–478 (2016).

98. Moore, J. K. et al. Sustained climate warming drives declining marine biological productivity. *Science* **359,** 1139–1143 (2018).

99. Moreno-Chamarro, E. et al. Impact of increased resolution on long-standing biases in HighResMIP-PRIMAVERA climate models. *Geoscientific Model Development* **15,** 269–289 (2022).

100. Morrison, A. K., Waugh, D. W., Hogg, A. M., Jones, D. C. & Abernathey, R. P. Ventilation of the Southern Ocean pycnocline. *Annual Review of Marine Science* **14,** 405–430 (2022).

101. *Encyclopedia of atmospheric sciences* 2nd ed. (eds North, G. R., Pyle, J. A. & Zhang, F.) 2998 pp. ISBN: 9780123822260 (Elsevier Science & Technology, 2014).

102. O'Brien, T. D. & Moriarty, R. *Global distributions of mesozooplankton abundance and biomass - Gridded data product (NetCDF) - Contribution to the MAREDAT World Ocean Atlas of Plankton Functional Types* data set (PANGAEA, 2012). https://doi.org/10.1594/PANGAEA.785501.

103. Oldenburg, D., Wills, R. C. J., Armour, K. C., Thompson, L. & Jackson, L. C. Mechanisms of low-frequency variability in north atlantic ocean heat transport and AMOC. *Journal of Climate* **34,** 1–68 (2021).

104. Orr, J. C. et al. Biogeochemical protocols and diagnostics for the CMIP6 Ocean Model Intercomparison Project (OMIP). *Geoscientific Model Development* **10,** 2169–2199 (2017).

105. Oschlies, A. A committed fourfold increase in ocean oxygen loss. *Nature Communications* **12** (2021).

106. Oschlies, A. in *Ocean deoxygenation: Everyone's problem - Causes, impacts, consequences and solutions* (eds Laffoley, D. & Baxter, J. M.) 117–135 (Gland, Switzerland: IUCN, 2019).

107. Oschlies, A., Brandt, P., Stramma, L. & Schmidtko, S. Drivers and mechanisms of ocean deoxygenation. *Nature Geoscience* **11,** 467–473 (2018).

108. Oschlies, A., Duteil, O., Getzlaff, J., Koeve, W., Landolfi, A. & Schmidtko, S. Patterns of deoxygenation: sensitivity to natural and anthropogenic drivers. *Philosophical Transactions of the Royal Society A: Mathematical, Physical and Engineering Sciences* **375.** 20160325 (2017).

109. Patara, L., Böning, C. W. & Tanhua, T. Multidecadal changes in Southern Ocean ventilation since the 1960s driven by wind and buoyancy forcing. *Journal of Climate* **34,** 1485–1502 (2021).

110. Plattner, G. K. et al. Long-Term Climate Commitments Projected with Climate-Carbon Cycle Models. *Journal of Climate* **21,** 2721–2751 (2008).

111. Portela, E., Kolodziejczyk, N., Vic, C. & Thierry, V. Physical mechanisms driving oxygen subduction in the global ocean. *Geophysical Research Letters* **47,** e2020GL089040 (2020).

112. Rabalais, N. N. in *Ocean deoxygenation: Everyone's problem - Causes, impacts, consequences and solutions* (eds Laffoley, D. & Baxter, J. M.) 105–116 (Gland, Switzerland: IUCN, 2019).

113. Rayner, D. et al. Monitoring the Atlantic meridional overturning circulation. *Deep Sea Research Part II: Topical Studies in Oceanography* **58,** 1744–1753 (2011).

114. Ridder, N. N. & England, M. H. Sensitivity of ocean oxygenation to variations in tropical zonal wind stress magnitude. *Global Biogeochemical Cycles* **28,** 909–926 (2014).

115. Rintoul, S. R. & Naveira Garabato, A. C. in *International Geophysics* 471–492 (Elsevier, 2013).

116. Rixen, T. et al. Reviews and syntheses: Present, past, and future of the oxygen minimum zone in the northern Indian Ocean. *Biogeosciences* **17,** 6051–6080 (2020).

117. Robinson, C. Microbial respiration, the engine of ocean deoxygenation. *Frontiers in Marine Science* **5** (2019).

118. Rosenblum, E., Fajber, R., Stroeve, J. C., Gille, S. T., Tremblay, L. B. & Carmack, E. C. Surface salinity under transitioning ice cover in the Canada Basin: climate model biases linked to vertical distribution of fresh water. *Geophysical Research Letters* **48** (2021).

119. Sarmiento, J. L., Gruber, N., Brzezinski, M. A. & Dunne, J. P. High-latitude controls of thermocline nutrients and low latitude biological productivity. *Nature* **427,** 56–60 (2004).

120. Sathyendranath, S. et al. Carbon-to-chlorophyll ratio and growth rate of phytoplankton in the sea. *Marine Ecology Progress Series* **383,** 73–84 (2009).

121. Schmidtko, S., Stramma, L. & Visbeck, M. Decline in global oceanic oxygen content during the past five decades. *Nature* **542,** 335–339 (2017).

122. Schmittner, A., Galbraith, E. D., Hostetler, S. W., Pedersen, T. F. & Zhang, R. Large fluctuations of dissolved oxygen in the Indian and Pacific oceans during Dansgaard-Oeschger oscillations caused by variations of North Atlantic Deep Water subduction. *Paleoceanography* **22,** PA3207 (2007).

123. Segschneider, J. & Bendtsen, J. Temperature-dependent remineralization in a warming ocean increases surface pCO_2 through changes in marine ecosystem composition. *Global Biogeochemical Cycles* **27,** 1214–1225 (2013).

124. Sharp, J. D., Fassbender, A. J., Carter, B. R., Johnson, G. C., Schultz, C. & Dunne, J. P. *GOBAI-O_2: A Global Gridded Monthly Dataset of Ocean Interior Dissolved Oxygen Concentrations Based on Shipboard and Autonomous Observations (NCEI Accession 0259304)* 2022.

125. Sharp, J. D., Fassbender, A. J., Carter, B. R., Johnson, G. C., Schultz, C. & Dunne, J. P. GOBAI-O_2: temporally and spatially resolved fields of ocean interior dissolved oxygen over nearly two decades. *Earth System Science Data Discussions.* preprint (2022).

126. Siegel, D. A. et al. Regional to global assessments of phytoplankton dynamics from the SeaWiFS mission. *Remote Sensing of Environment* **135,** 77–91 (2013).

127. Srokosz, M. A. & Bryden, H. L. Observing the Atlantic Meridional Overturning Circulation yields a decade of inevitable surprises. *Science* **348.** 1255575 (2015).

128. Stewart, K. D. et al. JRA55-do-based repeat year forcing datasets for driving ocean-sea-ice models. *Ocean Modelling* **147.** 101557 (2020).

129. Stramma, L. & Schmidtko, S. Spatial and temporal variability of oceanic oxygen changes and underlying trends. *Atmosphere-Ocean* **59,** 122–132 (2021).

130. Sun, Q., Du, Y., Xie, S. P., Zhang, Y., Wang, M. & Kosaka, Y. Sea surface salinity change since 1950: Internal variability versus anthropogenic forcing. *Journal of Climate* **34,** 1305–1319 (2021).

131. Taboada, F. G., Stock, C. A., Griffies, S. M., Dunne, J., John, J. G., Small, R. J. & Tsujino, H. Surface winds from atmospheric reanalysis lead to contrasting oceanic forcing and coastal upwelling patterns. *Ocean Modelling* **133,** 79–111 (Jan. 2019).

132. Takahashi, C. & Watanabe, M. Pacific trade winds accelerated by aerosol forcing over the past two decades. *Nature Climate Change* **6,** 768–772 (2016).

133. Talley, L. D., Pickard, G. L., Emery, W. J. & Swift, J. H. *Descriptive physical oceanography* 6th ed. 564 pp. ISBN: 0750645520 (Elsevier Science & Technology, 2011).

134. Thompson, D. W. J. & Solomon, S. Interpretation of recent Southern Hemisphere climate change. *Science* **296,** 895–899 (2002).

135. Thompson, D. W. J., Solomon, S., Kushner, P. J., England, M. H., Grise, K. M. & Karoly, D. J. Signatures of the Antarctic ozone hole in Southern Hemisphere surface climate change. *Nature Geoscience* **4,** 741–749 (2011).

136. Timmermann, A. et al. El Niño-Southern Oscillation complexity. *Nature* **559,** 535–545 (2018).

137. Tsujino, H. et al. JRA-55 based surface dataset for driving ocean–sea-ice models (JRA55-do). *Ocean Modelling* **130,** 79–139 (2018).

138. Tuchen, F. P., Lübbecke, J. F., Schmidtko, S., Hummels, R. & Böning, C. W. The Atlantic Subtropical Cells inferred from observations. *Journal of Geophysical Research: Oceans* **124,** 7591–7605 (2019).

139. Vallivattathillam, P. et al. Positive Indian Ocean Dipole events prevent anoxia off the west coast of India. *Biogeosciences* **14,** 1541–1559 (2017).

140. Vecchi, G. A., Soden, B. J., Wittenberg, A. T., Held, I. M., Leetmaa, A. & Harrison, M. J. Weakening of tropical Pacific atmospheric circulation due to anthropogenic forcing. *Nature* **441,** 73–76 (2006).

141. Visbeck, M. Power of pull. *Nature* **447,** 383–383 (2007).

142. von Schuckmann, K. et al. Heat stored in the Earth system: where does the energy go? *Earth System Science Data* **12,** 2013–2041 (2020).

143. Walker, S. J., Weiss, R. F. & Salameh, P. K. Reconstructed histories of the annual mean atmospheric mole fractions for the halocarbons CFC-11 CFC-12, CFC-113, and carbon tetrachloride. *Journal of Geophysical Research: Oceans* **105,** 14285–14296 (June 2000).

144. Weijer, W., Cheng, W., Garuba, O. A., Hu, A. & Nadiga, B. T. CMIP6 models predict significant 21st century decline of the Atlantic Meridional Overturning Circulation. *Geophysical Research Letters* **47** (2020).

145. Weiss, R. F. The solubility of nitrogen, oxygen and argon in water and seawater. *Deep Sea Research and Oceanographic Abstracts* **17,** 721–735 (1970).

146. Wolter, K. & Timlin, M. S. El Niño/Southern Oscillation behaviour since 1871 as diagnosed in an extended multivariate ENSO index (MEI.ext). *International Journal of Climatology* **31,** 1074–1087 (2011).

147. Xiu, P. & Chai, F. Eddies affect subsurface phytoplankton and oxygen distributions in the North Pacific subtropical gyre. *Geophysical Research Letters* **47** (2020).

148. Yang, H., Lohmann, G., Wei, W., Dima, M., Ionita, M. & Liu, J. Intensification and poleward shift of subtropical western boundary currents in a warming climate. *Journal of Geophysical Research: Oceans* **121,** 4928–4945 (2016).

149. Yu, L. & Jin, X. Buoy perspective of a high-resolution global ocean vector wind analysis constructed from passive radiometers and active scatterometers (1987–present). *Journal of Geophysical Research: Oceans* **117,** C11013 (2012).

150. Zhang, W., Li, J. & Zhao, X. Sea surface temperature cooling mode in the Pacific cold tongue. *Journal of Geophysical Research: Oceans* **115** (2010).

151. Zumwald, M., Knüsel, B., Baumberger, C., Hirsch Hadorn, G., Bresch, D. N. & Knutti, R. Understanding and assessing uncertainty of observational climate datasets for model evaluation using ensembles. *WIREs Climate Change* **11,** e654 (2020).

152. Zweng, M. M. et al. World Ocean Atlas 2018, Volume 2: Salinity. *NOAA Atlas NESDIS* **82** (ed Mishonov, A.) 50 pp. (2019).

A Appendix

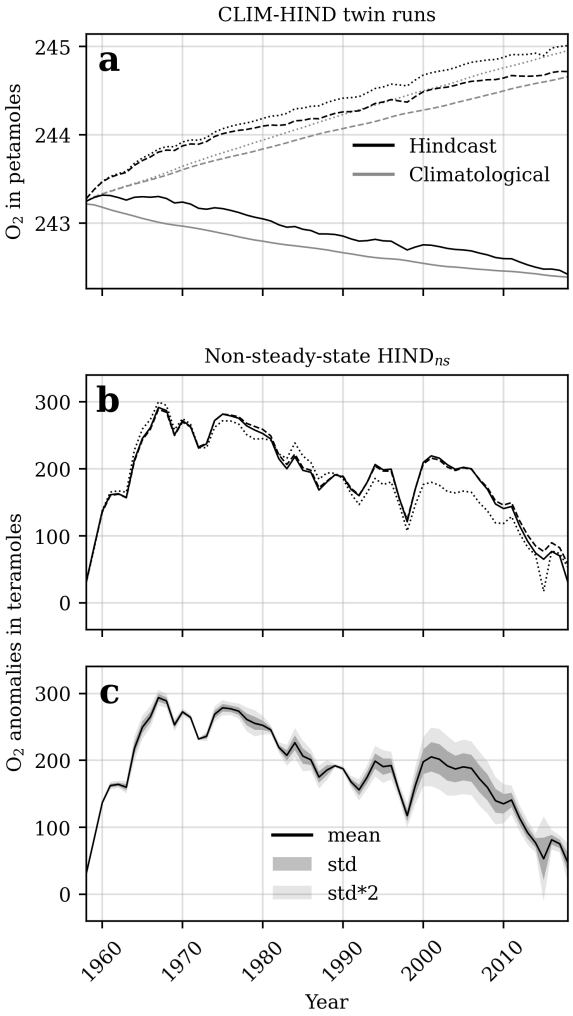

Figure A.1: **(a)** Time series of the globally integrated O_2 inventory in the ORCA025-MOPS CLIM-HIND twin runs. The HIND runs are shown in black and the CLIM runs are shown in grey. The CLIM-HIND twin runs differ in the configuration of the biogeochemical and physical parameters as described in Section 2.2. With reference to Table 2, the dotted lines correspond to Run 1, the dashed lines to Run 2, and the solid lines to Run 3. **(b)** O_2 inventory anomalies relative to CLIM, obtained by grid-point-wise subtraction of the O_2 inventory in CLIM from that in HIND for each CLIM-HIND twin. These anomalies, based on the assumption of a common steady-state between CLIM and HIND, capture the non-steady-state O_2 fluxes due solely to year-to-year atmospheric variability (Patara et al. 2021). **(c)** Mean and standard deviation (std) derived from the three $HIND_{ns}$ curves shown in **(b)**.

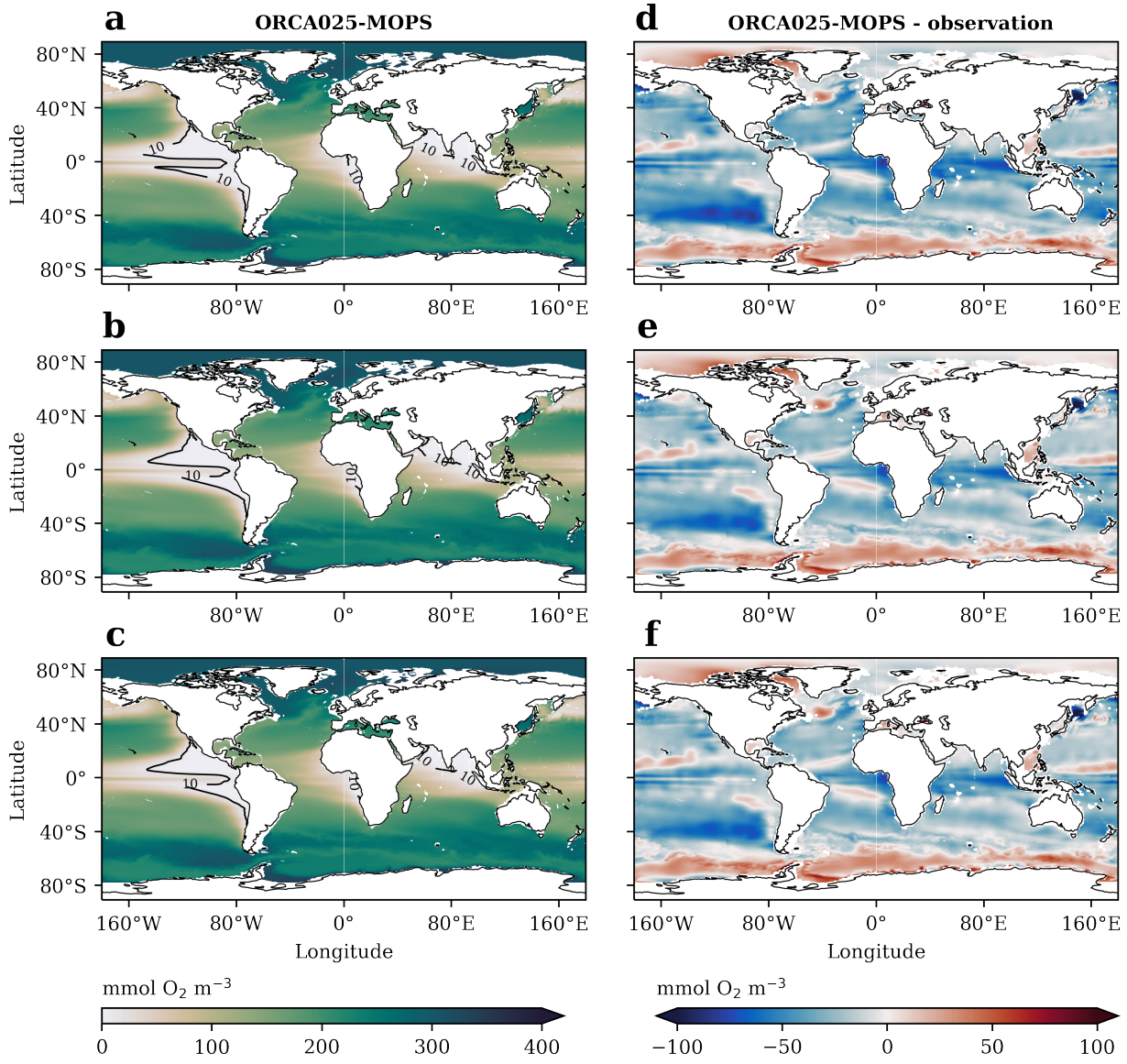

Figure A.2: O_2 climatology from 1958-2018 at 300 m depth for three hindcast runs **(a)**-**(c)** that differ in parameter configuration and are described in Section 2.2. The corresponding differences between model and observations are shown in **(d)**-**(f)**. The observational data used are from the World Ocean Atlas 2018 (Garcia et al. 2019). For details of the observations, refer to Section 2.4. Contour lines in **(a)**-**(c)** correspond to an O_2 concentration of 10 mmol O_2 m^{-3}.

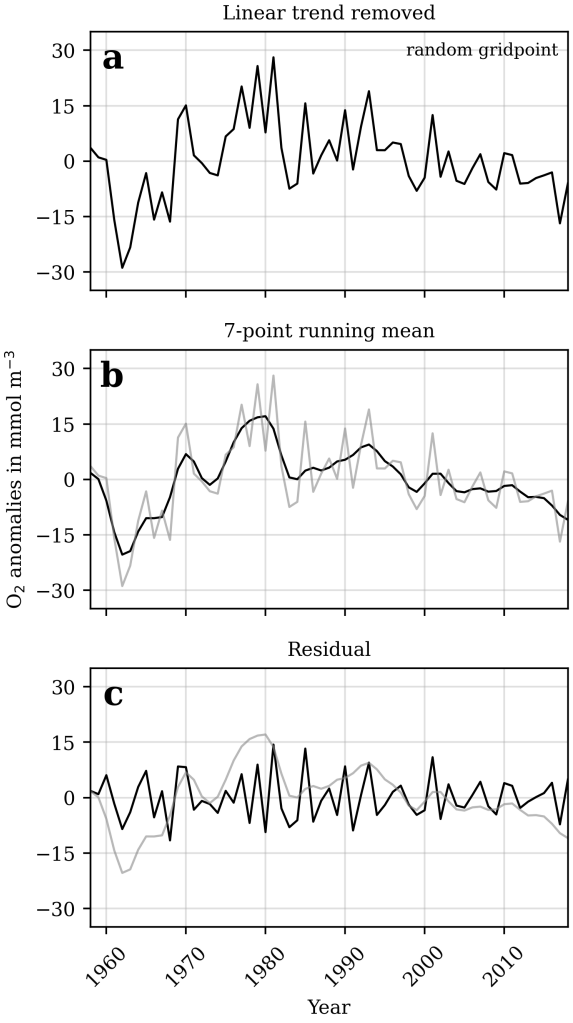

Figure A.3: Visualisation of the low and high-pass filter extraction method described in section 2.3 for a single grid point. **(a)** Time series of O_2 anomalies for a randomly selected grid point. Prior to filtering, any linear trend was removed by fitting a linear regression and detrending the data. **(b)** Low-pass filtered data (i.e., decadal variability), obtained by applying a 7-year running mean to the O_2 anomaly data in **(a)**. **(c)** High-pass filtered data (i.e., interannual variability), calculated by subtracting the low-pass filtered data in **(b)** from the corresponding points in time of the original signal in **(a)**.

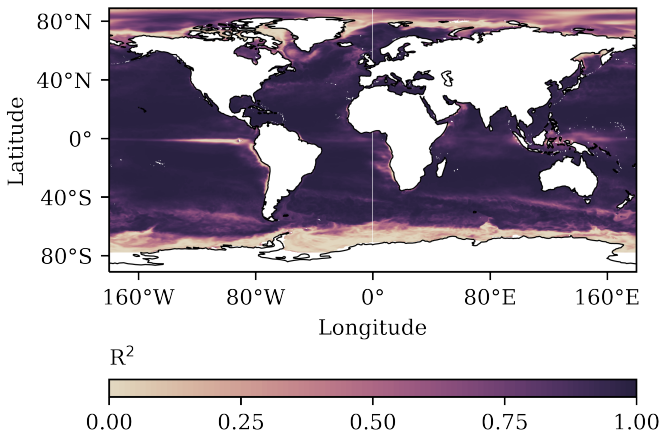

Figure A.4: Coefficient of determination R^2 for simulated O_2 and O_2^{sat} over 1958-2018 for the surface ocean.

Table A.1: Results of ordinary least squares regression analyses for change in globally integrated oxygen inventory over the Periods i, ii, and iv described in Section 4.1.1. Estimates refer to fitted slopes (teramoles O_2 per decade). Intercepts are not shown.

Data	Estimate ± se	p-value	$R^2_{adj.}$	F-statistic (df)
Period i (1960-1967)				
Model: full column	209.50 ± 33.90	.001	.871	41.62 (1, 5)
Model: 0-1,000 m	245.58 ± 30.76	.000	.913	63.74 (1, 5)
Observations: Ito-17	568.12 ± 127.44	.007	.759	19.87 (1, 5)
Period ii (1967-1994)				
Model: full column	-45.72 ± 4.53	.000	.802	106.0 (1, 25)
Model: 0-1,000 m	-85.12 ± 3.86	.000	.949	485.6 (1, 25)
Observations: Ito-17	-8.84 ± 22.26	.695	-0.033	0.1577 (1, 25)
Period iv (2002-2018)				
Model: full column	-109.18 ± 7.60	.000	.936	204.4 (1, 13)
Model: 0-1,000 m	-24.95 ± 5.37	.000	.595	21.56 (1, 13)
Observations: GOBAI-O_2	-381.83 ± 22.47	.000	.954	288.8 (1, 13)

Abbreviations: se = standard error; df = degrees of freedom.

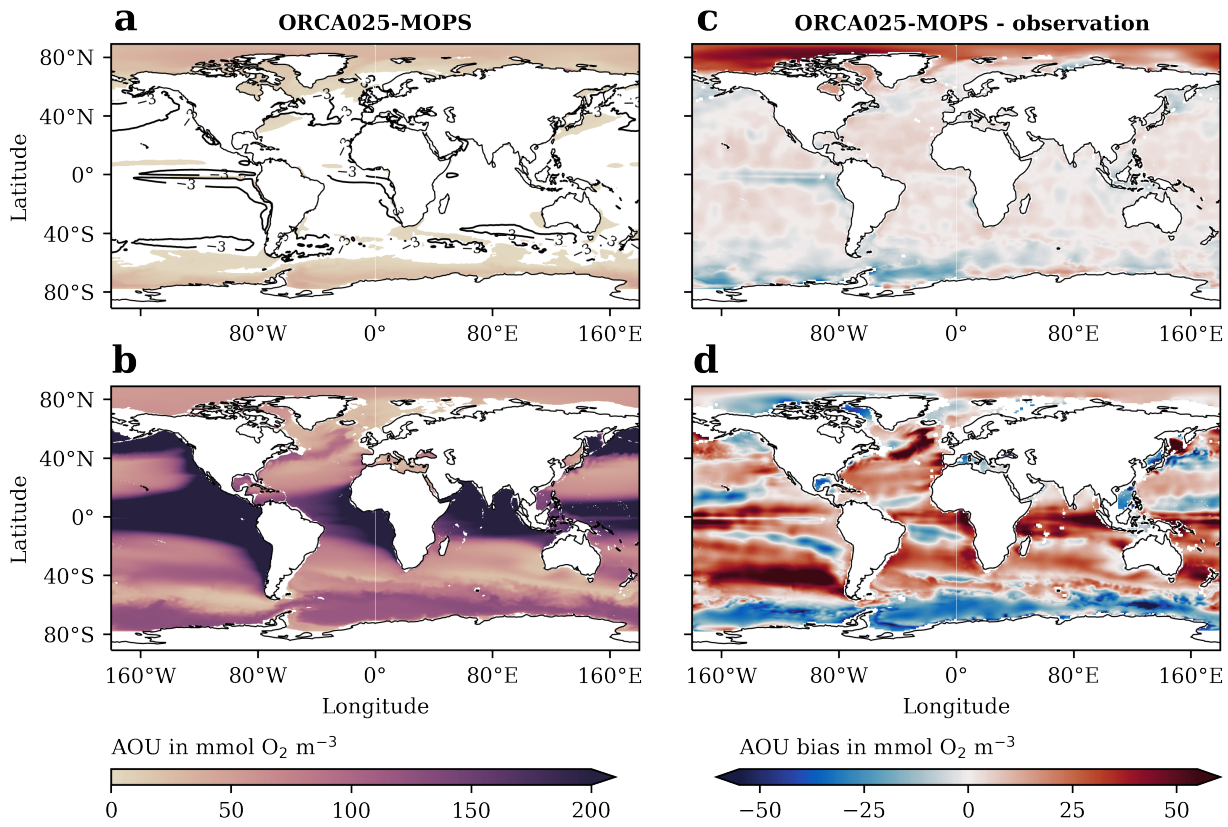

Figure A.5: AOU climatology from 1958-2018 in the ORCA025-MOPS hindcast simulation **(a)** for the surface ocean and **(b)** at 300 m depth. In **(a)**, regions of AOU<0 are shown in white, denoting O_2 oversaturation, with minimum AOU values of $\sim$ -14.2 mmol O_2 m^{-3} and -8.2 mmol O_2 m^{-3} for model results and observations (Garcia et al. 2019), respectively. Contour lines in **(a)** correspond to an AOU of -3 mmol O_2 m^{-3}. The corresponding differences between model and observations are shown in **(c)** for the surface ocean and in **(d)** at 300 m depth. The observational data used are from the World Ocean Atlas 2018 (Garcia et al. 2019). For details of the observations, refer to Section 2.4.

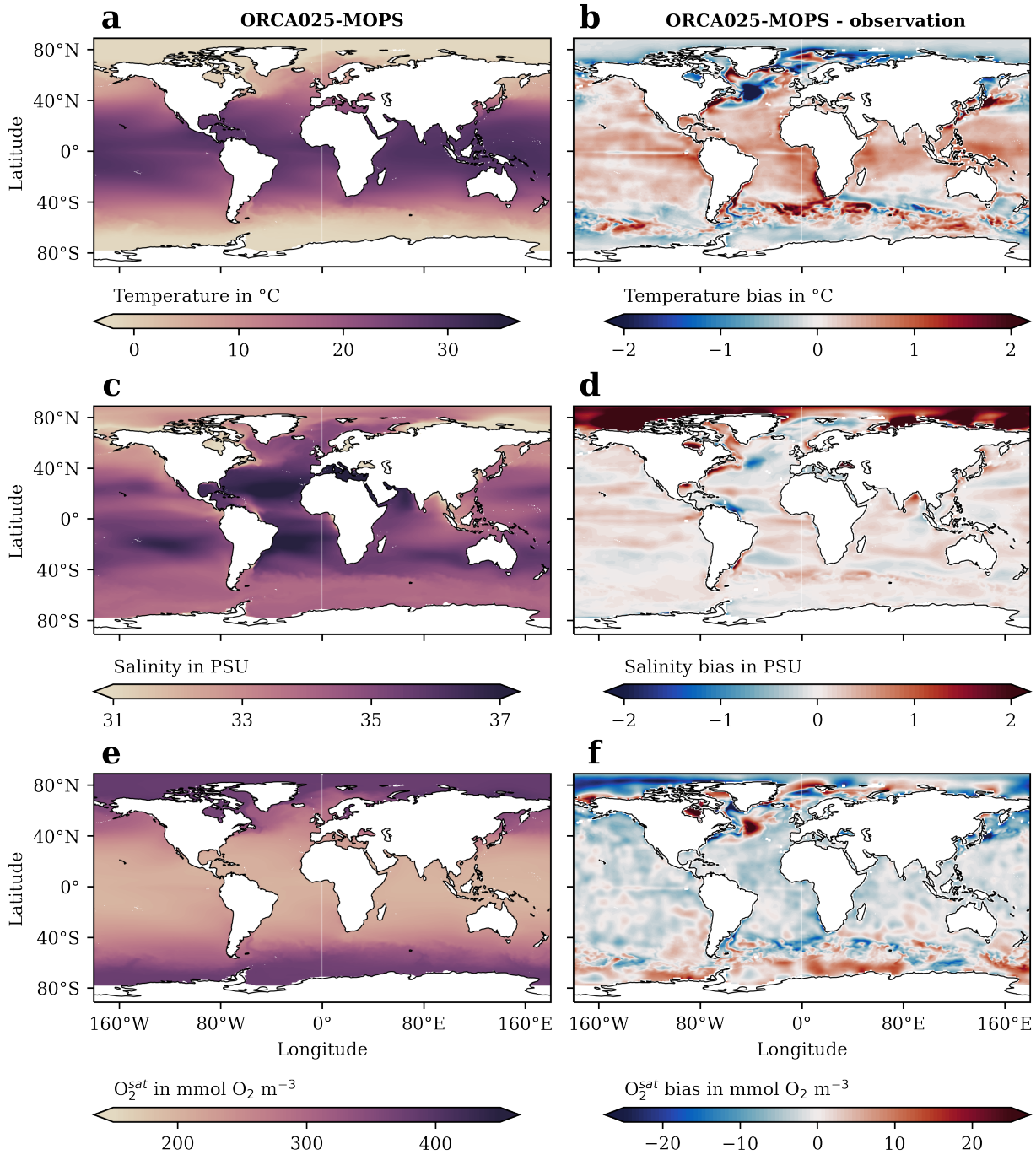

Figure A.6: Climatologies of sea surface **(a)** temperature, **(c)** salinity, and **(e)** O_2^{sat} from 1958-2018 in the ORCA025-MOPS hindcast simulation. Corresponding differences between model and observations are shown in **(b)**, **(d)**, and **(f)**, respectively. The observational data used for sea surface temperature and salinity are from the World Ocean Atlas 2018 (Locarnini et al. 2019; Zweng et al. 2019). Observational O_2^{sat} is calculated as the sum of AOU (World Ocean Atlas 2018; Garcia et al. 2019) and measured dissolved O_2^{obs} (World Ocean Atlas 2018; Garcia et al. 2019). For details of the observations, refer to Section 2.4.

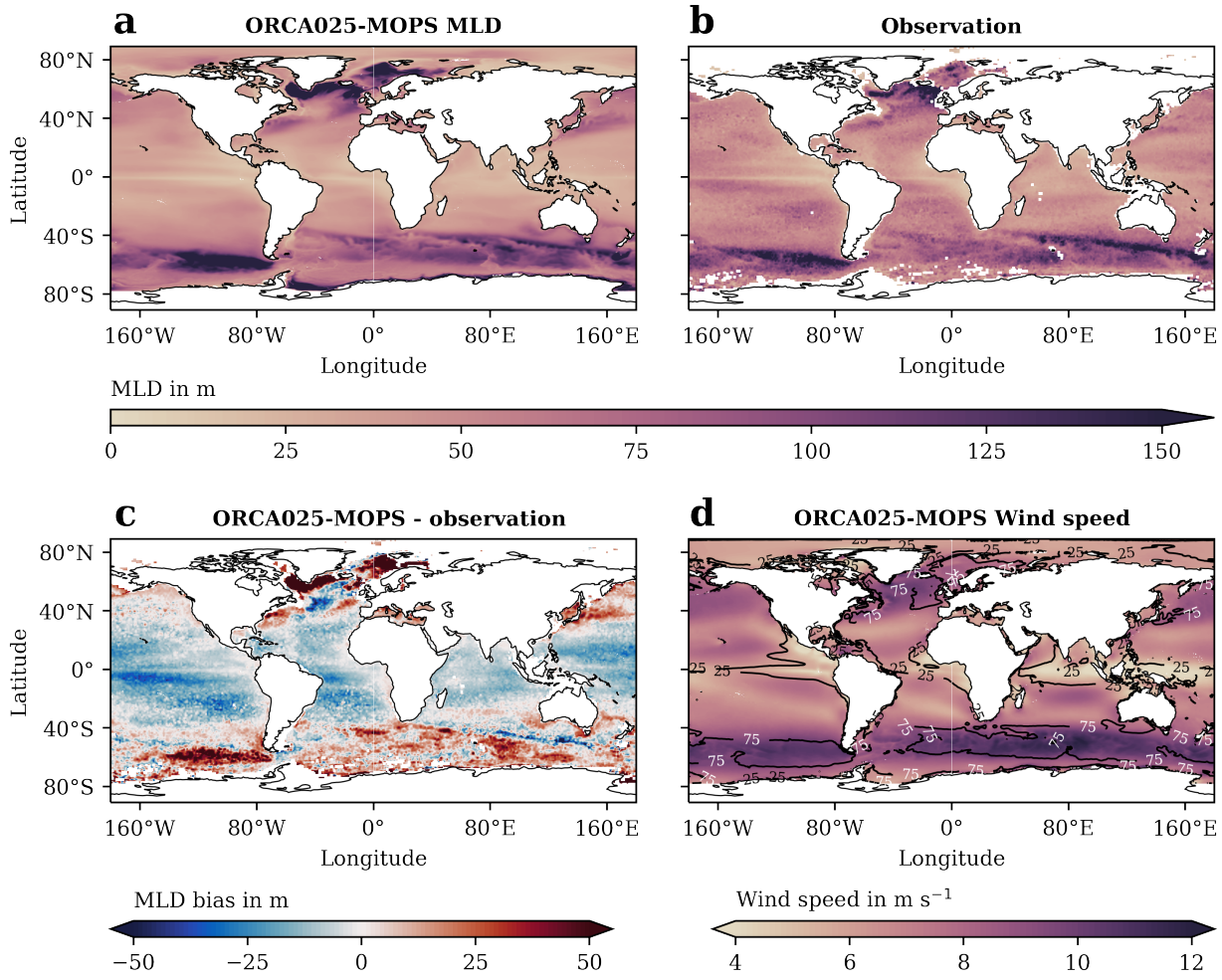

Figure A.7: Mixed layer depth climatology in **(a)** the ORCA025-MOPS hindcast simulation from 2000 to 2018 and **(b)** corresponding observational data from 2000 to 2021. Differences between model and observations are shown in **(c)**. The observational data are derived from Argo profiles (Holte et al. 2017), with additional details in Section 2.4. **(d)** Wind speed climatology in the ORCA025-MOPS hindcast simulation from 1958 to 2018. Contour lines in **(d)** represent mixed layer depths of 25 (black labels) and 75 m (white labels).

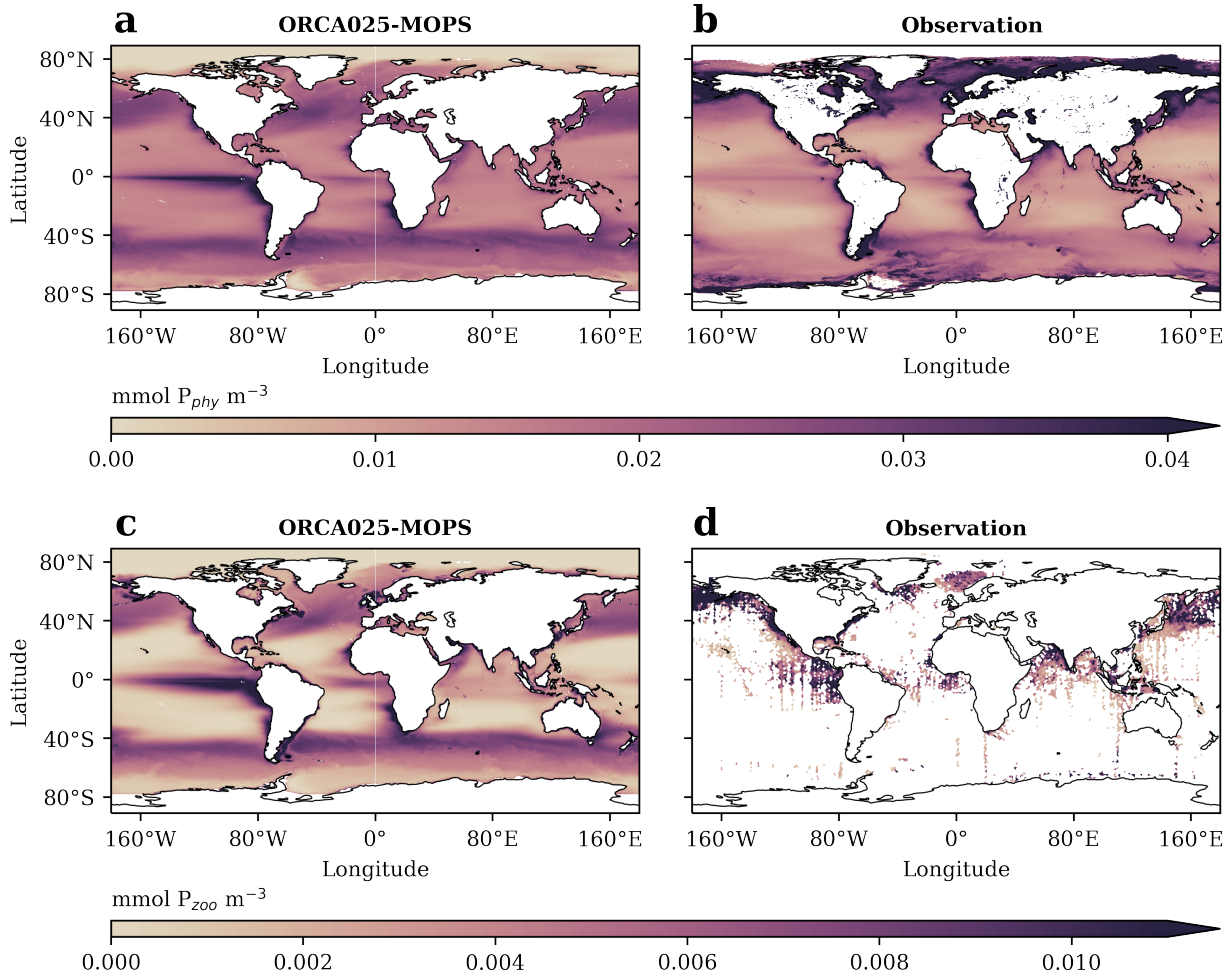

Figure A.8: Organic tracer concentrations for **(a)-(b)** the first layer (∼ 6 m) of phytoplankton and **(c)-(d)** 0–200 m of zooplankton climatologies from 2002-2017 and 1932-2010 (1958-2010 for model results), respectively, in the hindcast simulation and observations. Observational data of phytoplankton and zooplankton are derived from chlorophyll-a (MODIS-Aqua; Melin 2013) and mesozooplankton (MAREDAT; O'Brien & Moriarty 2012), respectively. For details of the observations, including details on the conversion to phosphorus units, refer to Section 2.4.

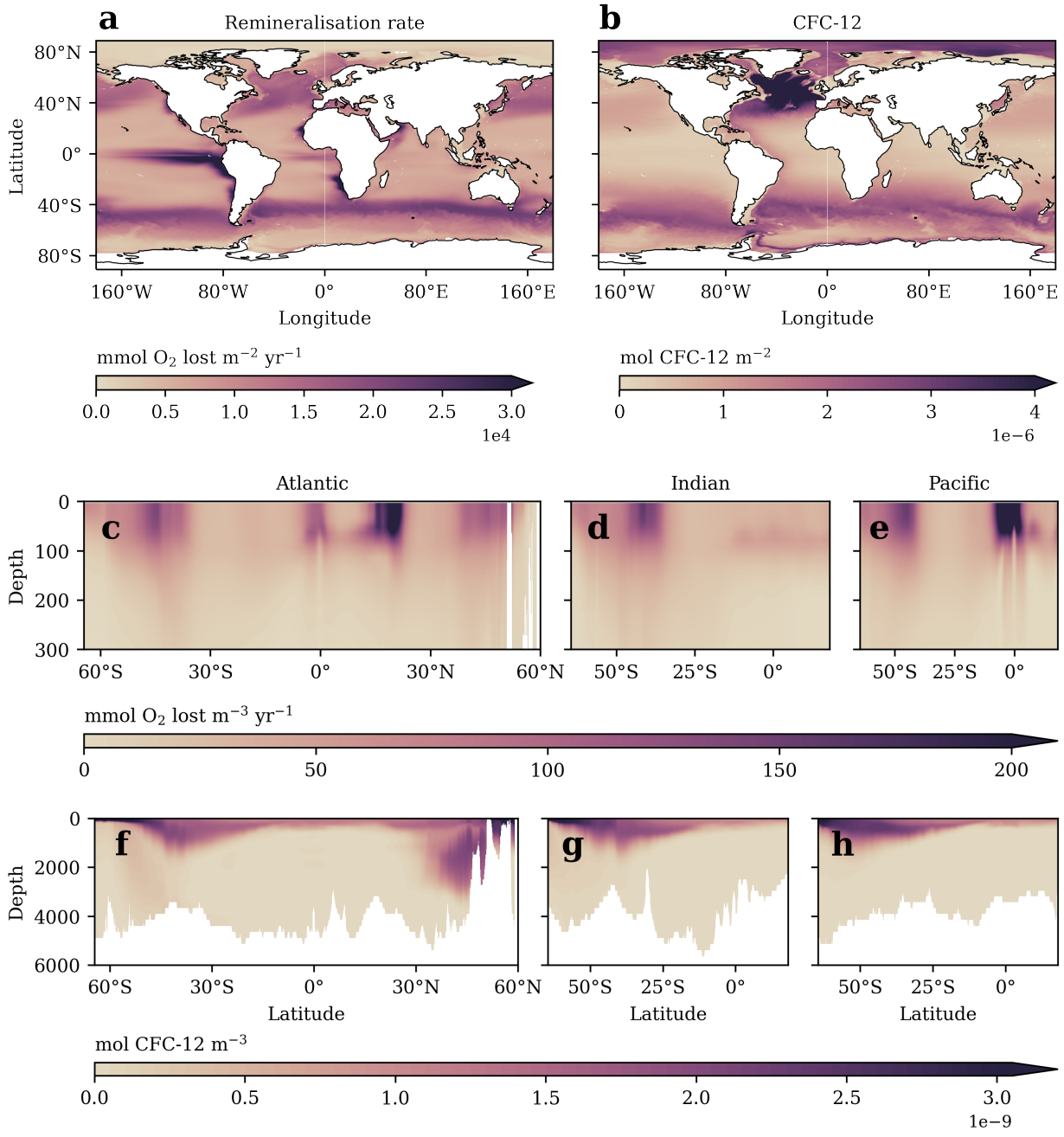

Figure A.9: Column integrated **(a)** mean remineralisation rate from 1958-2018 and **(b)** CFC-12 inventory for the year 2018 in the ORCA025-MOPS hindcast simulation. Vertical sections across the Atlantic (20°W), Indian (90°E), and Pacific (103°W) Oceans are shown in **(c)**-**(e)** for remineralisation rate and in **(f)**-**(h)** for CFC-12 concentrations. Remineralisation rate was converted from mmol phosphorus remineralised m^{-3} yr^{-1} to mmol O_2 lost m^{-3} yr^{-1} using an O_2:P ratio of 162 mol O_2 : mol P.

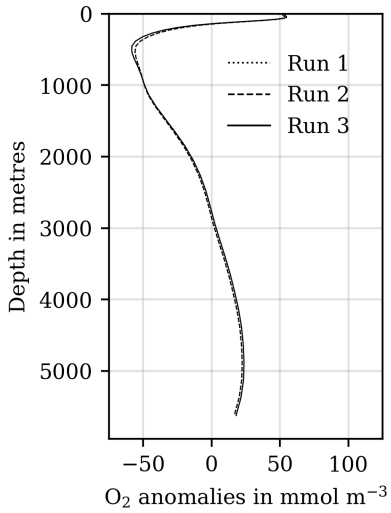

Figure A.10: Global vertical profile of O_2 concentrations simulated by the three ORCA025-MOPS HIND experiments. With reference to Table 2, the dotted lines correspond to Run 1, the dashed lines to Run 2, and the solid lines to Run 3. All data are mean centred.

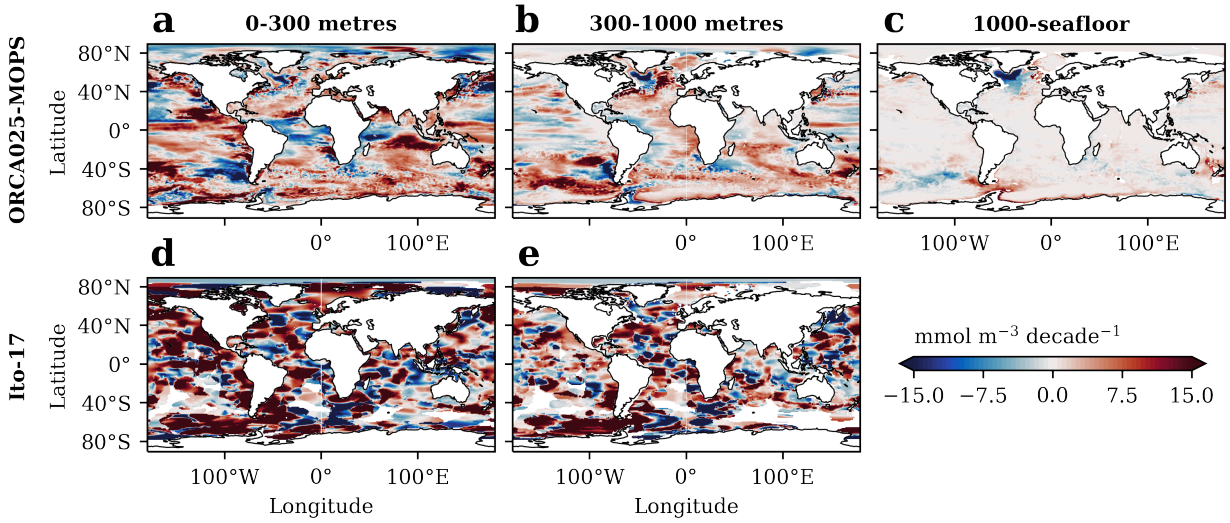

Figure A.11: Change in oxygen concentrations per decade from 1960-1967 (Period i) averaged over three different depth horizons (columns) in **(a)-(c)** ORCA025-MOPS $HIND_{ns}$ (ensemble mean) and **(d)-(e)** observations (Ito-17; Ito et al. 2017). For details of the observations, refer to Section 2.4.

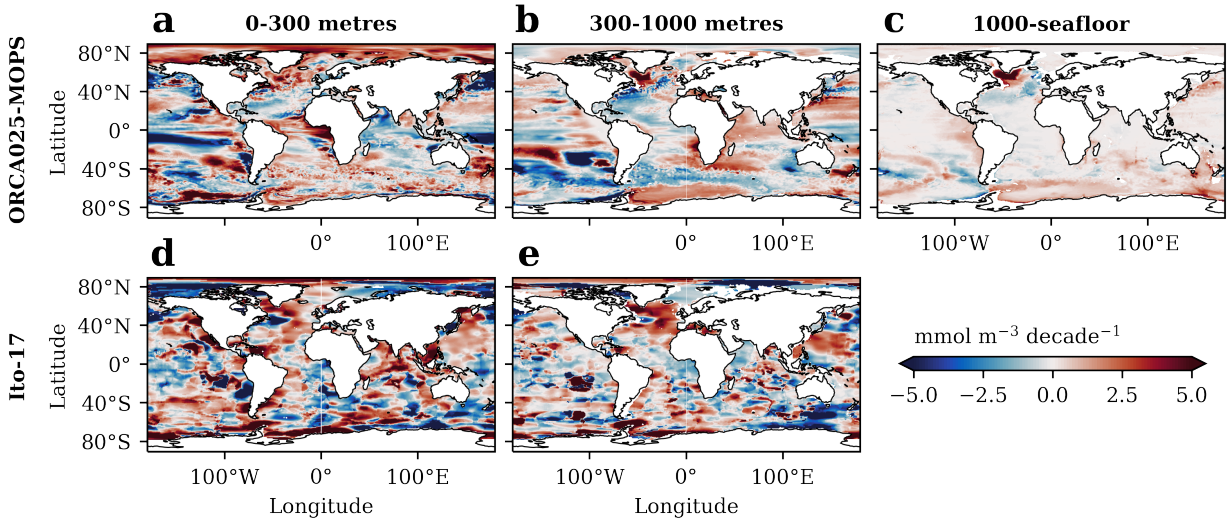

Figure A.12: Change in oxygen concentrations per decade from 1967-1994 (Period ii) averaged over three different depth horizons (columns) in **(a)-(c)** ORCA025-MOPS $HIND_{ns}$ (ensemble mean) and **(d)-(e)** observations (Ito-17; Ito et al. 2017). For details of the observations, refer to Section 2.4.

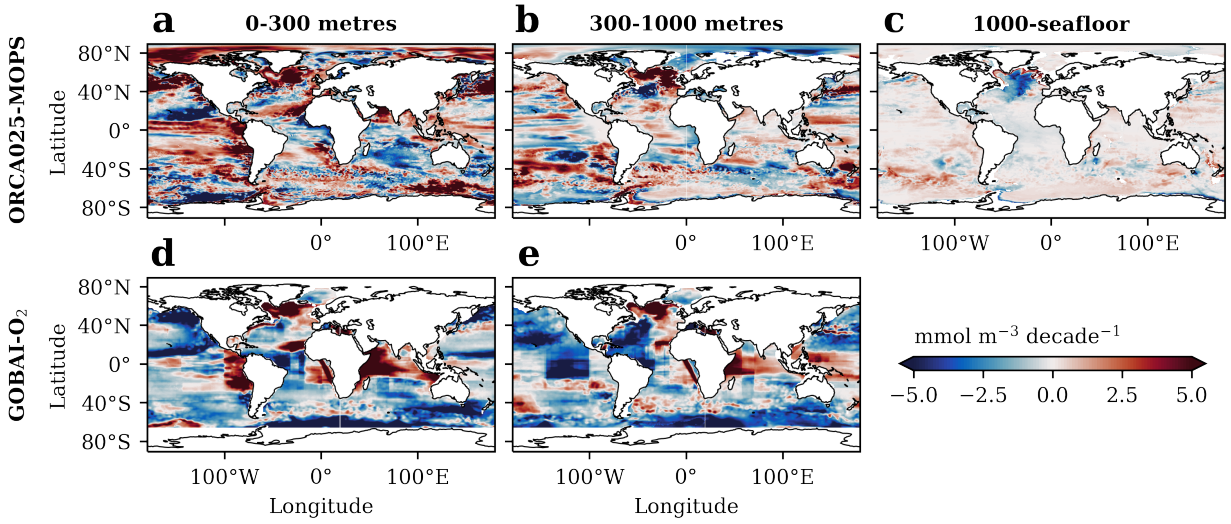

Figure A.13: Change in oxygen concentrations per decade from 2004-2018 (Period iv) averaged over three different depth horizons (columns) in **(a)-(c)** ORCA025-MOPS $HIND_{ns}$ (ensemble mean) and **(d)-(e)** observations (GOBAI-O_2; Sharp et al. 2022a). For details of the observations, refer to Section 2.4.

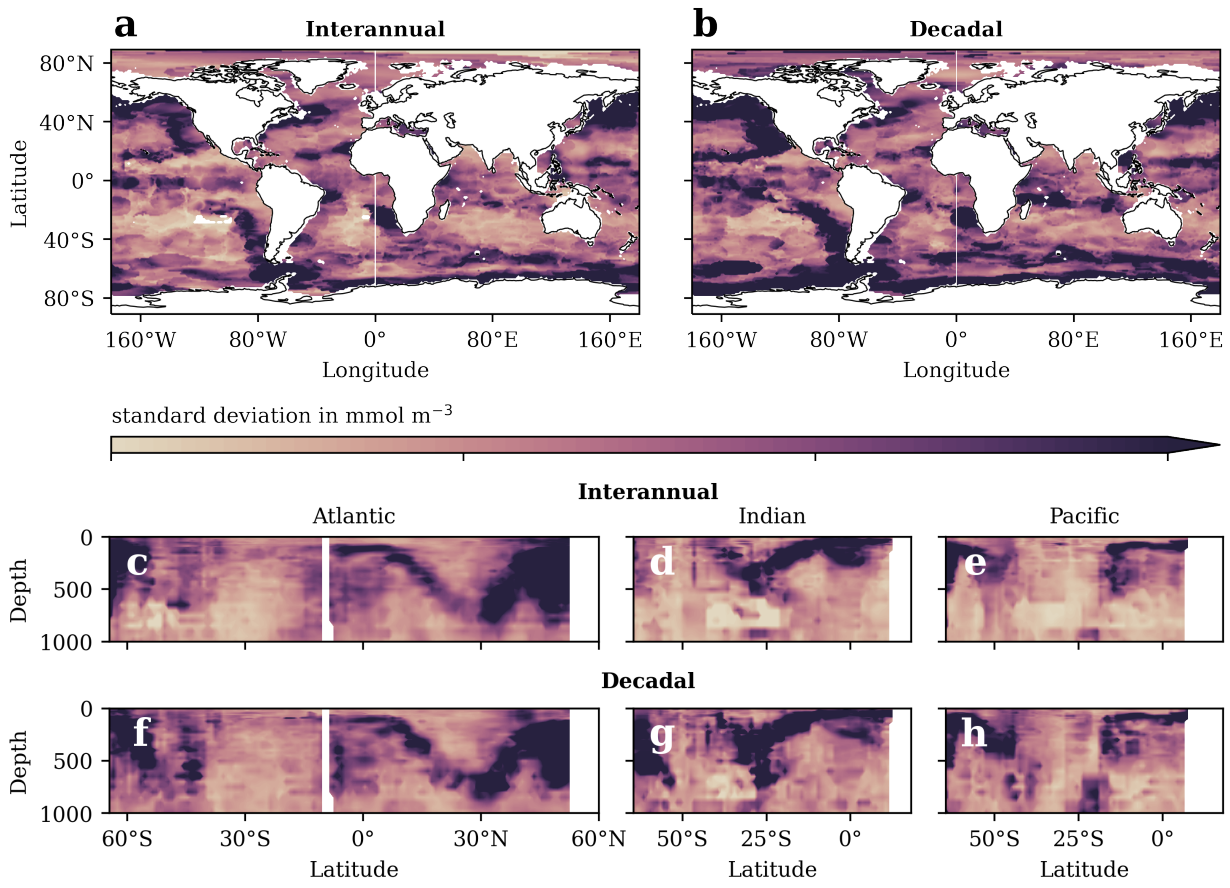

Figure A.14: As Figure 8, but showing standard deviations of *observational* O_2 anomaly data from 1960-2010. The observational data used are from Ito et al. (2017). For details of the observations, refer to Section 2.4. Contour lines are not shown.

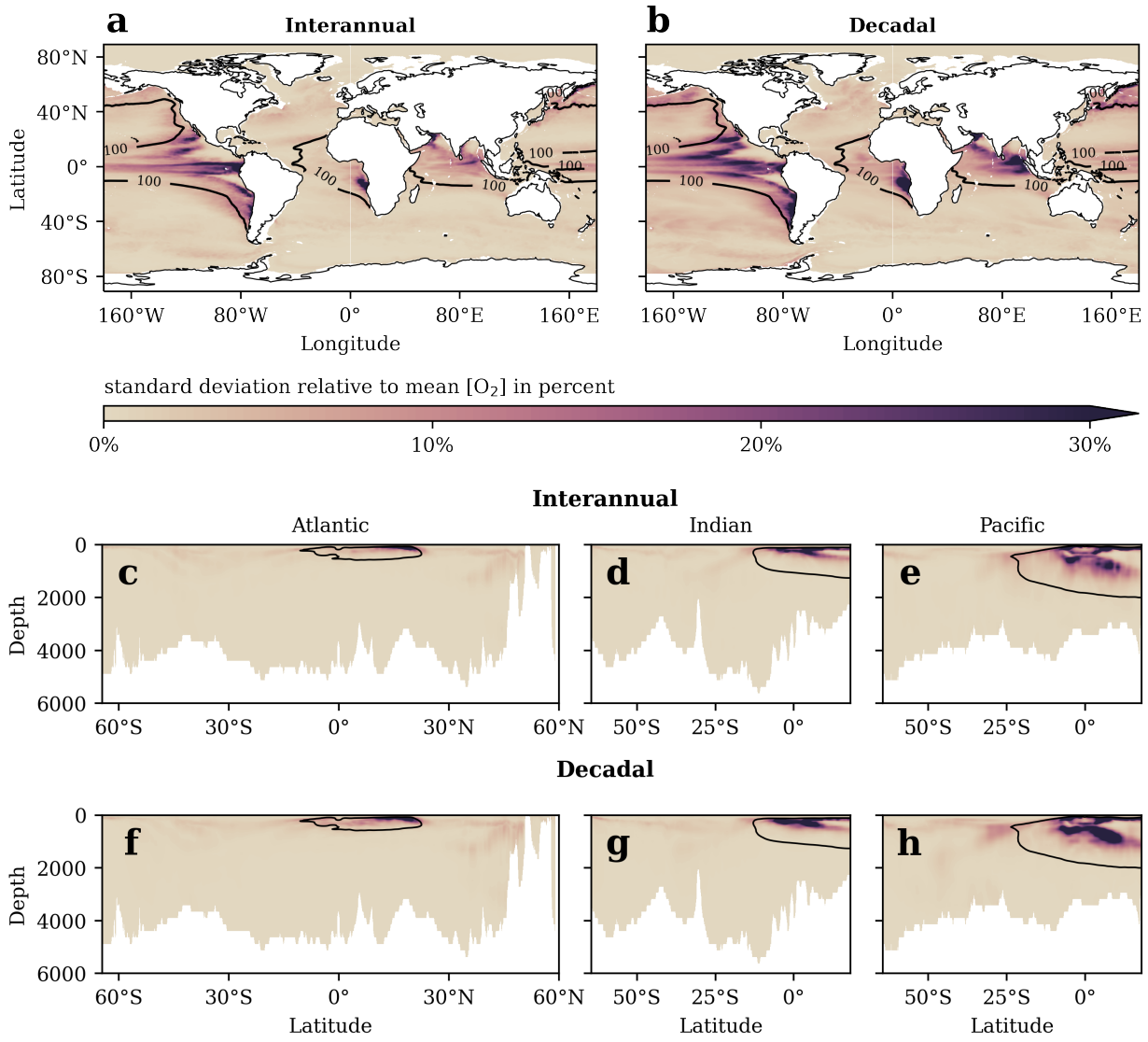

Figure A.15: As Figure 8, but showing *normalised* standard deviations, relative to the 1958-2018 mean oxygen concentration in ORCA025-MOPS HIND. Contour lines correspond to an climatological mean O_2 concentration (i.e., corresponding to Figure 2) of 100 mmol m^{-3}.

Table A.2: Results of ordinary least squares regression analyses for changes in globally integrated oxygen, O_2^{sat}, CFC-12, and remineralisation rate from 1960 to 1967 (Period i). Estimates refer to fitted slopes with the respective units in parentheses. Intercepts are not shown.

Experiment	Estimate ± se	p-value	$R^2_{adj.}$	F-statistic (df)
Oxygen change (Tmol dec^{-1})				
Hindcast	257.11 ± 26.67	.000	.920	92.92 (1,7)
Wind stress	87.54 ± 11.49	.000	.877	58.09 (1,7)
Buoyancy	148.10 ± 30.40	.002	.740	23.73 (1,7)
O_2^{sat} change (Tmol dec^{-1})				
Hindcast	124.38 ± 14.01	.000	.907	78.86 (1,7)
Wind stress	51.40 ± 7.75	.000	.843	43.96 (1,7)
Buoyancy	64.34 ± 10.08	.000	.832	40.74 (1,7)
CFC-12 change (% of mean inventory dec^{-1})				
Hindcast	.039 ± .247	.877	-0.139	.026 (1,7)
Wind stress	-0.335 ± .136	.043	.388	6.08 (1,7)
Buoyancy	.015 ± .273	.957	-0.142	.003 (1,7)
RR change (Tmol O_2 lost year^{-1} dec^{-1})				
Hindcast	-30.59 ± 37.17	0.438	.088	.677 (1,7)

Abbreviations: se = standard error; df = degrees of freedom; RR = remineralisation rate.

Note: For CFC-12 change, regressions were fitted to CFC-12 inventory (inv.) anomalies in percent relative to the CFC-12 inv. of the respective year ($HIND_{ns} \div CLIM \times 100$) to adjust for the increase in CFC-12 inv. over 1958-2018 and the inherently smaller absolute CFC-12 inv. anomalies (HIND-CLIM) at the beginning of the simulation.

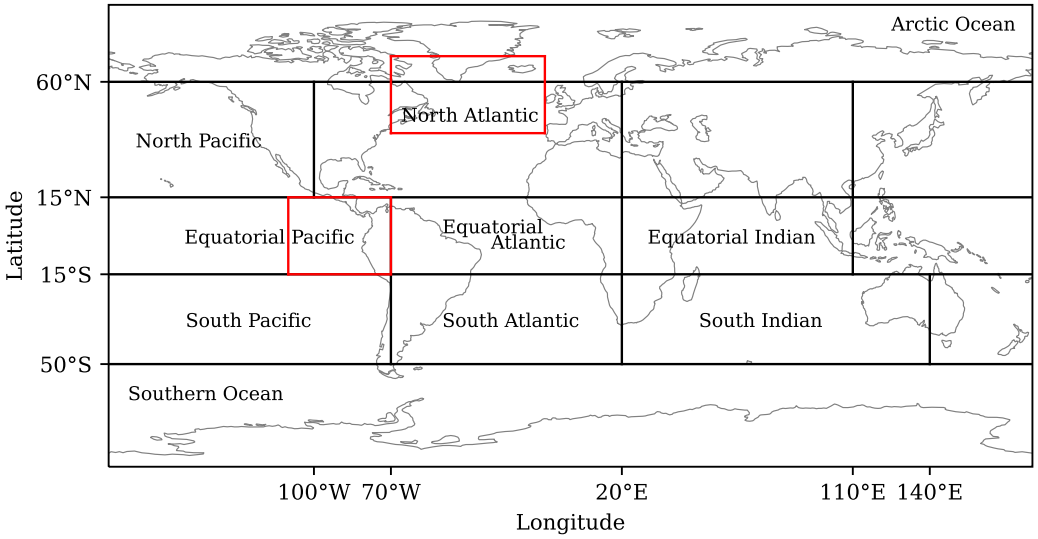

Figure A.16: Overview of the boundaries of the sub-regions analysed. The regions under discussion in the main text are outlined in red, while the broader regions are outlined in black.

Table A.3: As Table A.2, but for Period ii (1967-1994).

Experiment	Estimate ± se	p-value	$R^2_{adj.}$	F-statistic (df)
Oxygen change (Tmol dec^{-1})				
Hindcast	-45.72 ± 5.02	.000	.759	82.83 (1,25)
Wind stress	69.07 ± 4.08	.000	.917	287.1 (1,25)
Buoyancy	-95.18 ± 4.56	.000	.944	436.2 (1,25)
O_2^{sat} change (Tmol dec^{-1})				
Hindcast	-1.89 ± 2.77	.503	-0.021	0.4627 (1,25)
Wind stress	36.86 ± 1.86	.000	.938	391.0 (1,25)
Buoyancy	-28.46 ± 2.24	.000	.860	160.9 (1,25)
CFC-12 change (% of mean inventory dec^{-1})				
Hindcast	-0.290 ± .051	.000	.548	32.56 (1,25)
Wind stress	.499 ± .051	.000	.787	97.07 (1,25)
Buoyancy	-0.496 ± .049	.000	.793	100.7 (1,25)
RR change (Tmol O_2 lost $year^{-1}$ dec^{-1})				
Hindcast	-37.95 ± 14.70	0.016	0.179	6.665 (1,25)

Abbreviations: se = standard error; df = degrees of freedom; RR = remineralisation rate.

Table A.4: As Table A.2, but for Period iv (2002-2018).

Experiment	Estimate ± se	p-value	$R^2_{adj.}$	F-statistic (df)
Oxygen change (Tmol dec^{-1})				
Hindcast	-109.18 ± 6.39	.000	.954	292.1 (1,13)
Wind stress	28.53 ± 5.90	.000	.615	23.39 (1,13)
Buoyancy	-174.80 ± 5.53	.000	.986	999.2 (1,13)
O_2^{sat} change (Tmol dec^{-1})				
Hindcast	-69.75 ± 2.72	.000	.979	656.2 (1,13)
Wind stress	6.86 ± 2.54	.018	.310	7.293 (1,13)
Buoyancy	-76.66 ± 3.79	.000	.967	408.6 (1,13)
CFC-12 change (% of mean inventory dec^{-1})				
Hindcast	-0.296 ± .035	.000	.832	70.33 (1,13)
Wind stress	.060 ± .025	.029	.265	6.038 (1,13)
Buoyancy	-0.374 ± .019	.000	.965	391.3 (1,13)
RR change (Tmol O_2 lost $year^{-1}$ dec^{-1})				
Hindcast	-61.55 ± 23.52	0.021	0.295	6.848 (1,13)

Abbreviations: se = standard error; df = degrees of freedom; RR = remineralisation rate.

Table A.5: As Table A.2, but for Periods ii-iv (1967-2018).

Experiment	Estimate ± se	p-value	$R^2_{adj.}$	F-statistic (df)
Oxygen change (Tmol dec^{-1})				
Hindcast	-34.23 ± 2.70	.000	.757	160.2 (1,50)
Wind stress	64.18 ± 1.85	.000	.959	1198.0 (1,50)
Buoyancy	-92.23 ± 2.62	.000	.960	1240.0 (1,50)
O_2^{sat} change (Tmol dec^{-1})				
Hindcast	-11.96 ± 2.19	.000	.362	29.95 (1,50)
Wind stress	27.39 ± 1.35	.000	.889	409.7 (1,50)
Buoyancy	-29.86 ± 1.43	.000	.895	433.6 (1,50)
CFC-12 change (% of mean inventory dec^{-1})				
Hindcast	-0.119 ± .019	.000	.442	41.33 (1,50)
Wind stress	.317 ± .019	.000	.840	268.7 (1,50)
Buoyancy	-0.295 ± .018	.000	.842	272.4 (1,50)
RR change (Tmol O_2 lost year^{-1} dec^{-1})				
Hindcast	-13.84 ± 5.16	0.010	0.108	7.199 (1,50)

Abbreviations: se = standard error; df = degrees of freedom; RR = remineralisation rate.

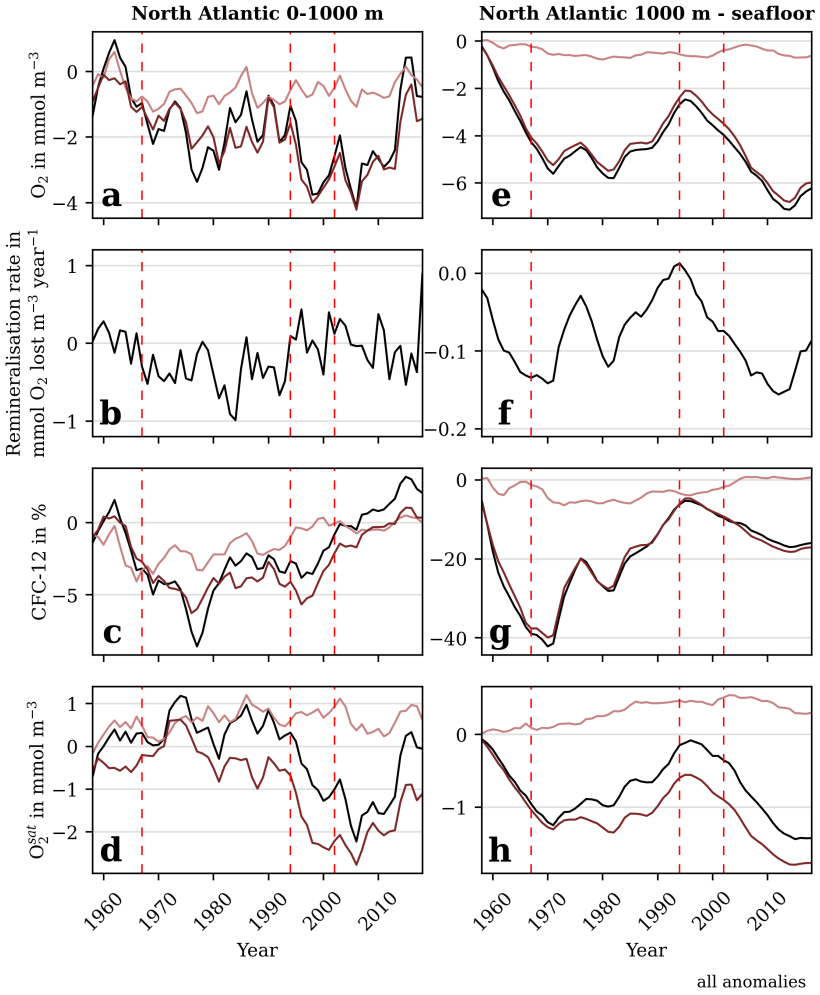

Figure A.17: Time series of mean **(a)** O_2 concentration, **(b)** remineralisation rate, **(c)** CFC-12 concentration, and **(d)** O_2^{sat} anomalies for the North Atlantic Ocean (40°N-70°N latitude; 70°W-10°W longitude) in ORCA025-MOPS $HIND_{ns}$ (black), $WIND_{ns}$ (rose), and $BUOY_{ns}$ (purple). The specific area boundaries are provided in Table 3. Red dashed lines mark the four different periods of O_2 content evolution (Section 4.1.1). For CFC-12 concentration anomalies, percentages are computed relative to the mean CFC-12 concentration of the respective year as $HIND_{ns} \div CLIM \times 100$.

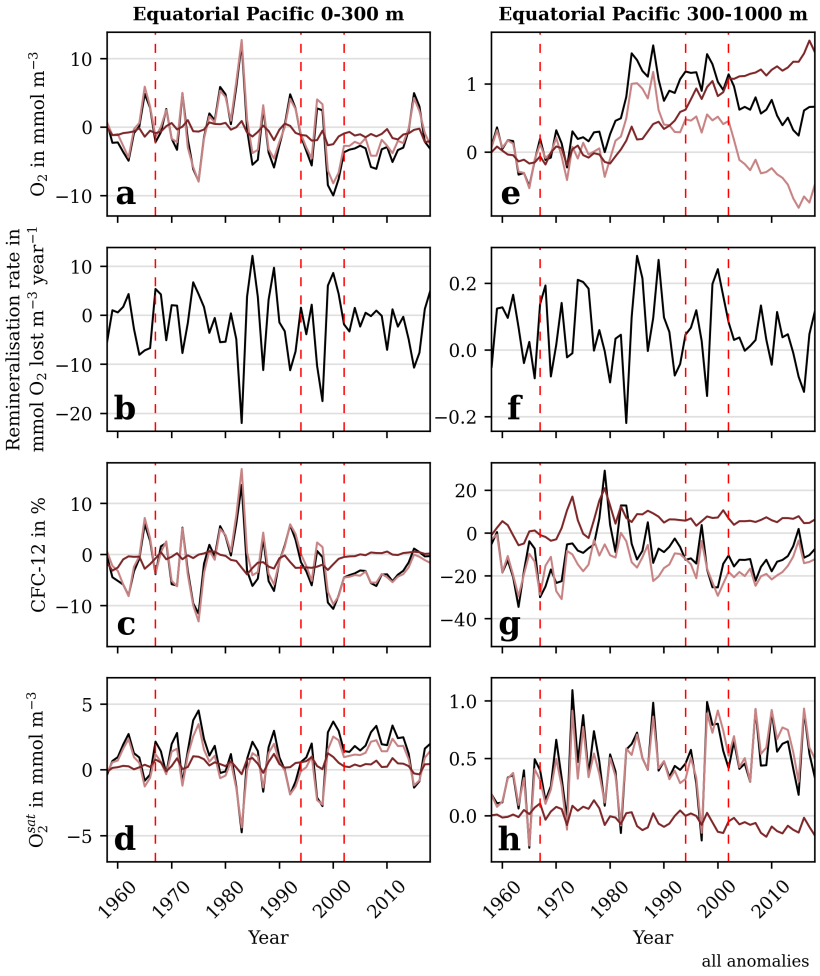

Figure A.18: As Figure A.17, but for the eastern equatorial Pacific Ocean (15°S-15°N latitude; 110°W-70°W longitude).

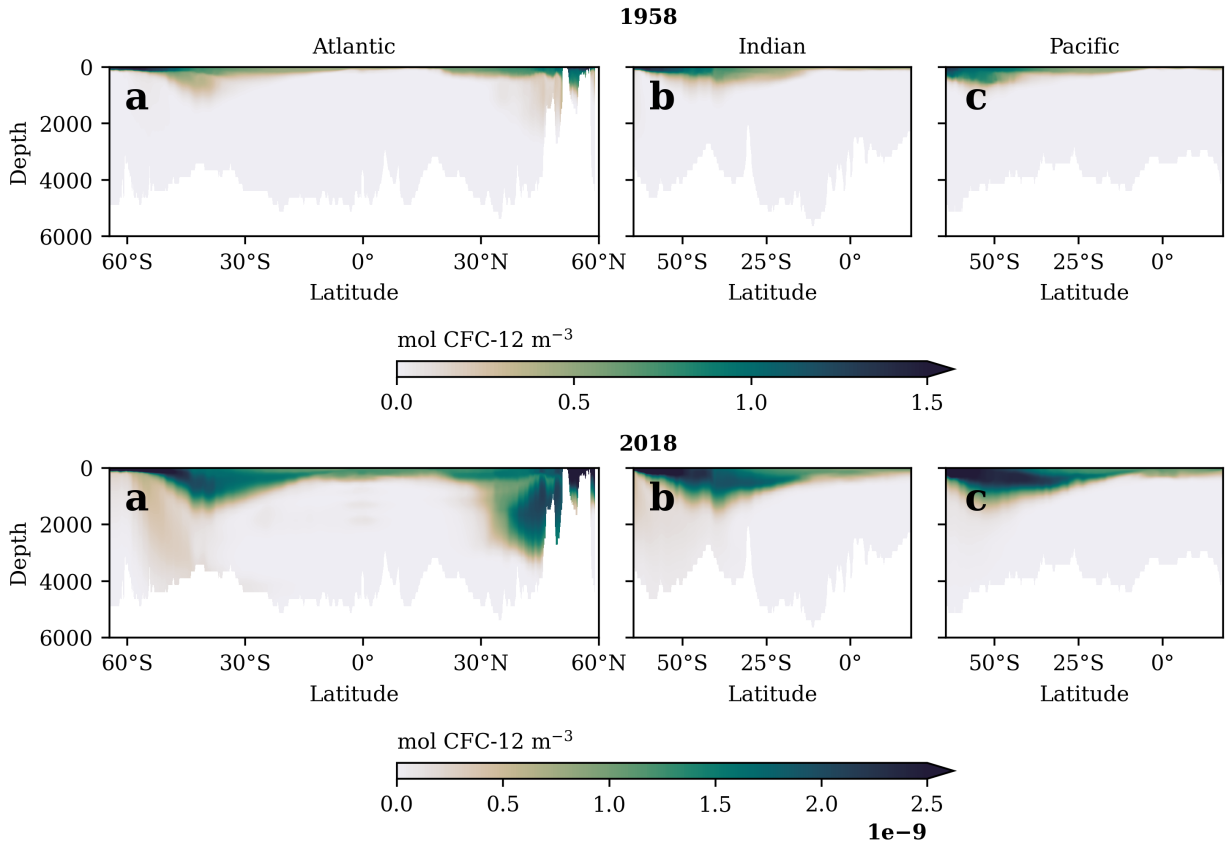

Figure A.19: O_2 climatology from 1958-2018 in the ORCA025-MOPS hindcast simulations (ensemble mean) across the **(a)** Atlantic (20°W), **(b)** Indian (90°E), and **(c)** Pacific (103°W) Oceans. The corresponding differences between model and observations are shown in **(d)**-**(f)**, respectively. The observational data used are from the World Ocean Atlas 2018 (Garcia et al. 2019). For details of the observations, refer to Section 2.4. Contour lines in **(a)**-**(c)** correspond to an O_2 concentration of 10 mmol m^{-3}.

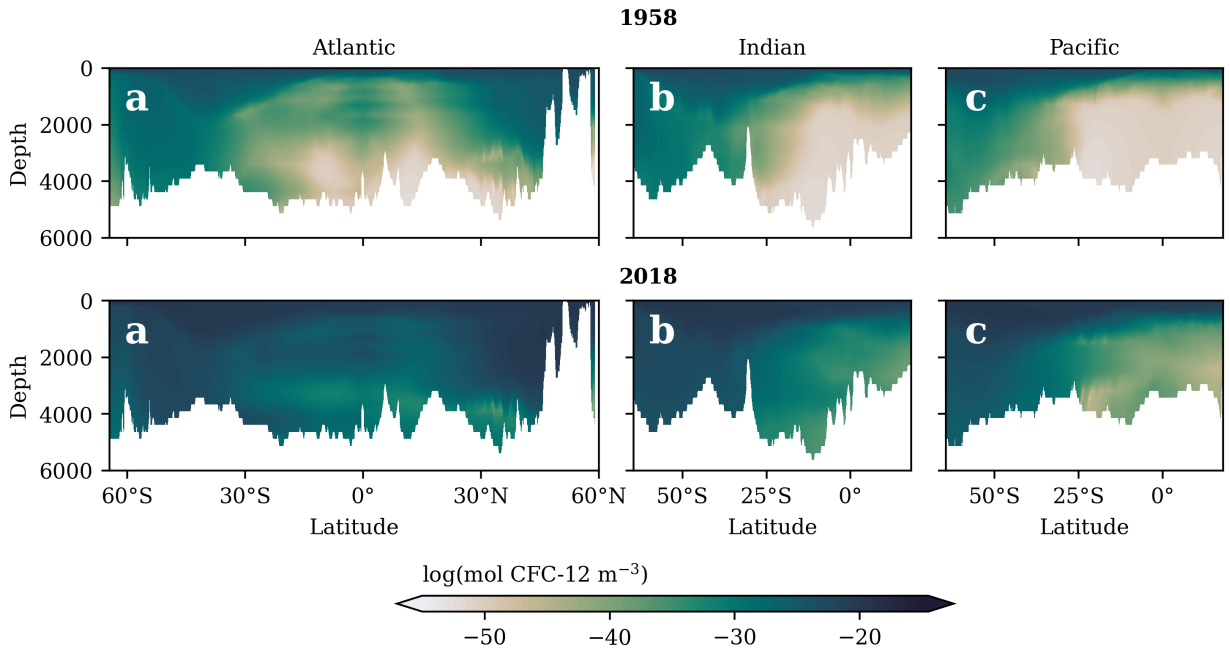

Figure A.20: O_2 climatology from 1958-2018 in the ORCA025-MOPS hindcast simulations (ensemble mean) across the **(a)** Atlantic (20°W), **(b)** Indian (90°E), and **(c)** Pacific (103°W) Oceans. The corresponding differences between model and observations are shown in **(d)**-**(f)**, respectively. The observational data used are from the World Ocean Atlas 2018 (Garcia et al. 2019). For details of the observations, refer to Section 2.4. Contour lines in **(a)**-**(c)** correspond to an O_2 concentration of 10 mmol m^{-3}.

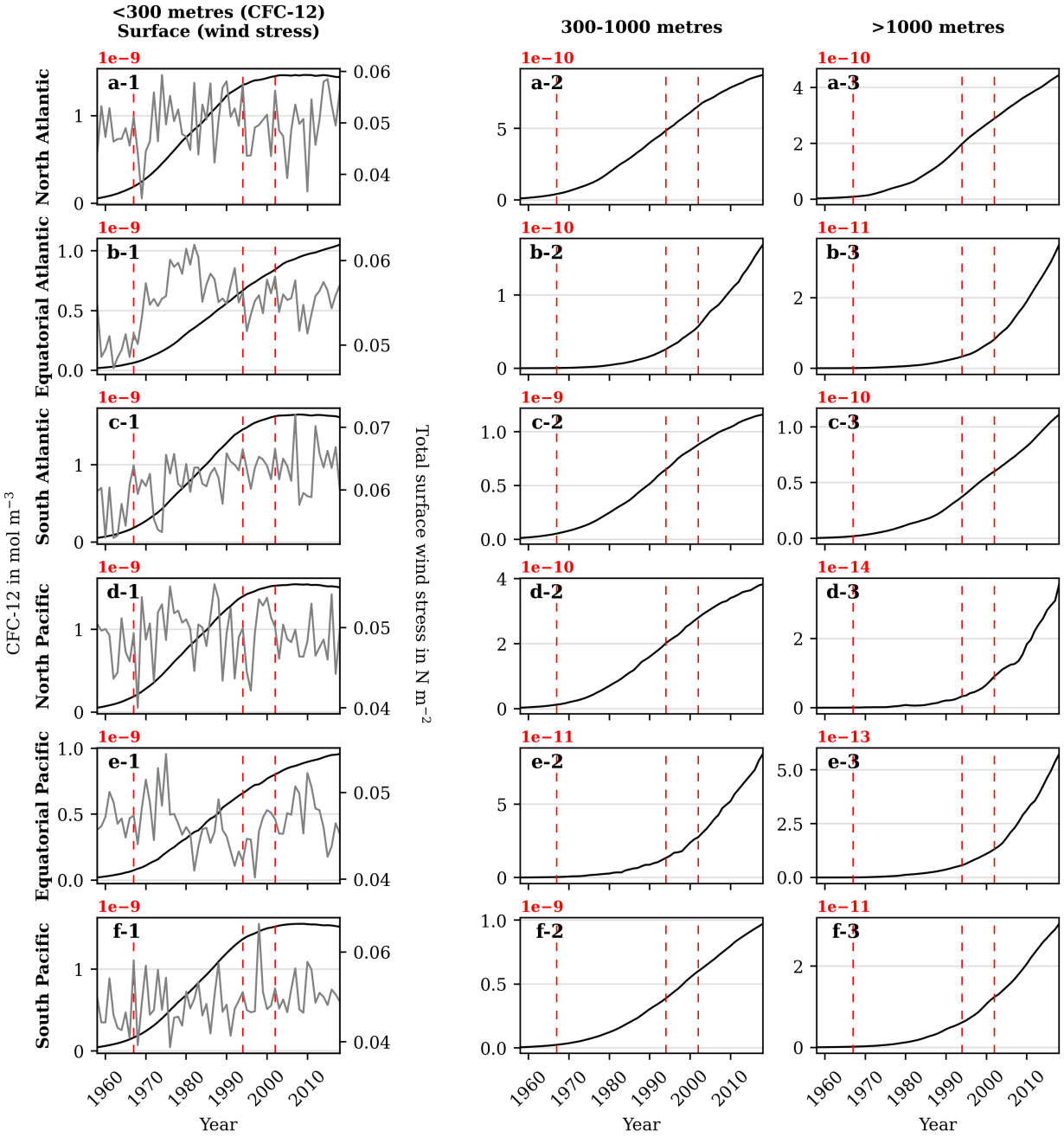

Figure continues on the next page.

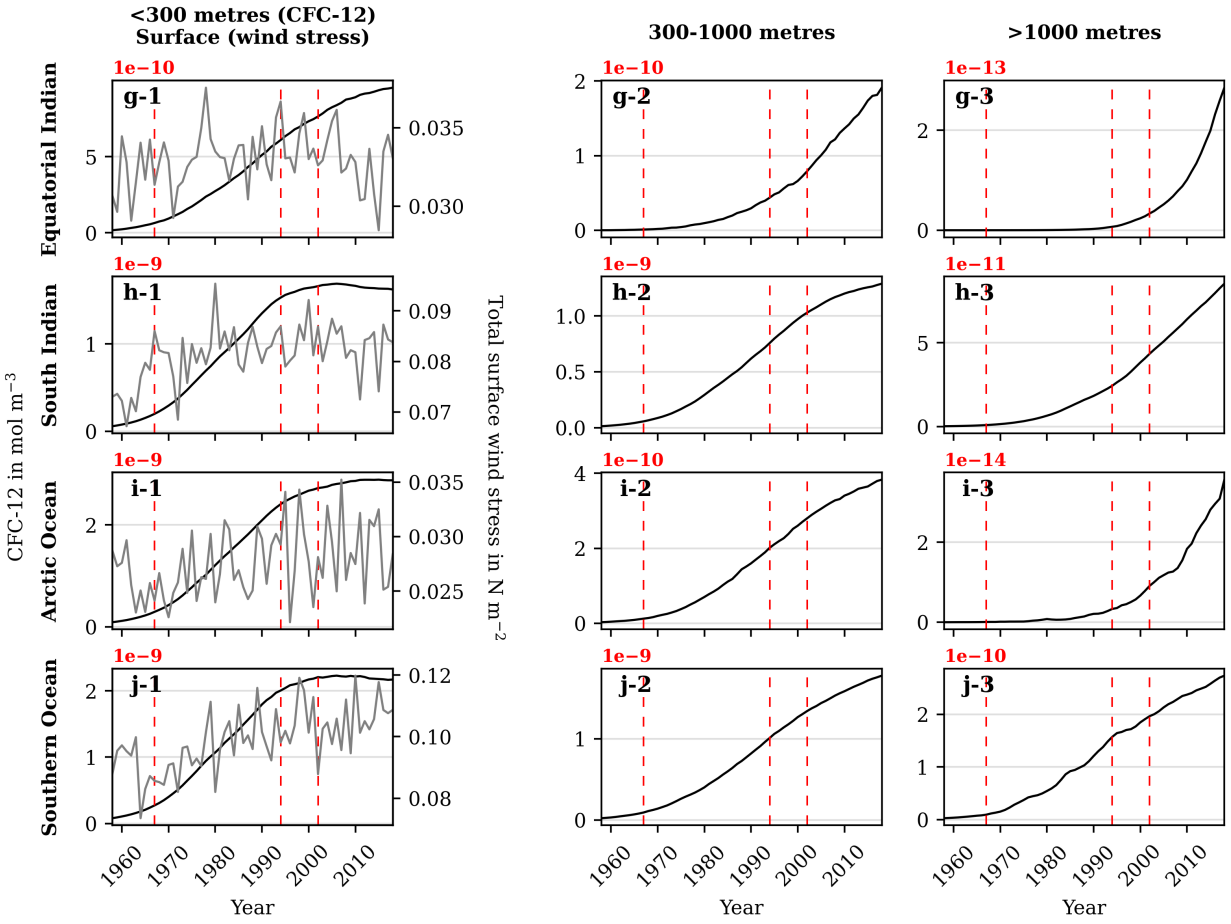

Figure A.21: Time series of average CFC-12 concentrations (black; left axis) and average vector sum surface wind stress (grey; right axis) for 10 different ocean regions (rows) and for CFC-12 concentrations over 3 different depth ranges (columns). An overview of the area boundaries for the sub-regions is shown in Figure A.16. Red dashed lines mark the four different periods of O_2 content evolution as described in Section 4.1.1.

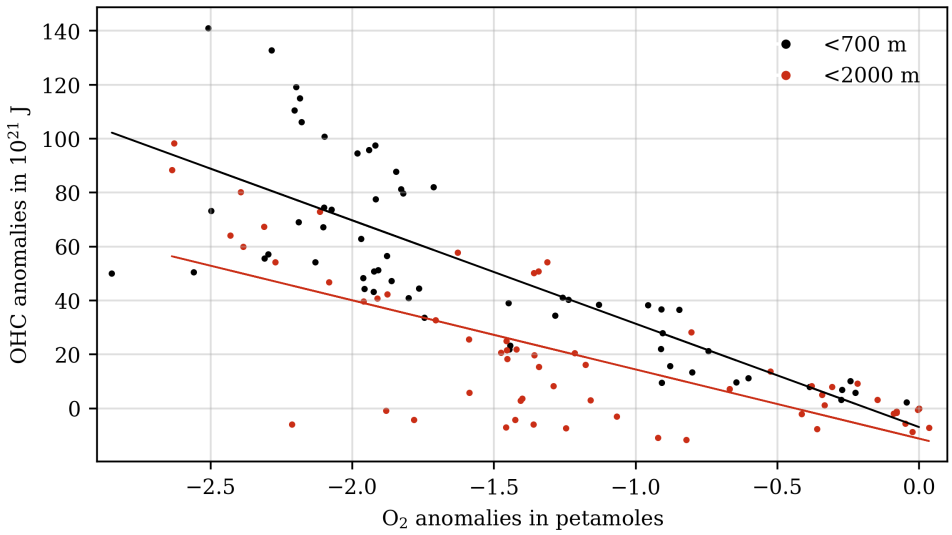

Figure A.22: Relation between global oxygen inventory and ocean heat content for the 0-700 m (black) and 0-2,000 m (red) layers in ORCA025-MOPS $HIND_{ns}$. Changes are relative to 1967 and plotted over 1958-2018.

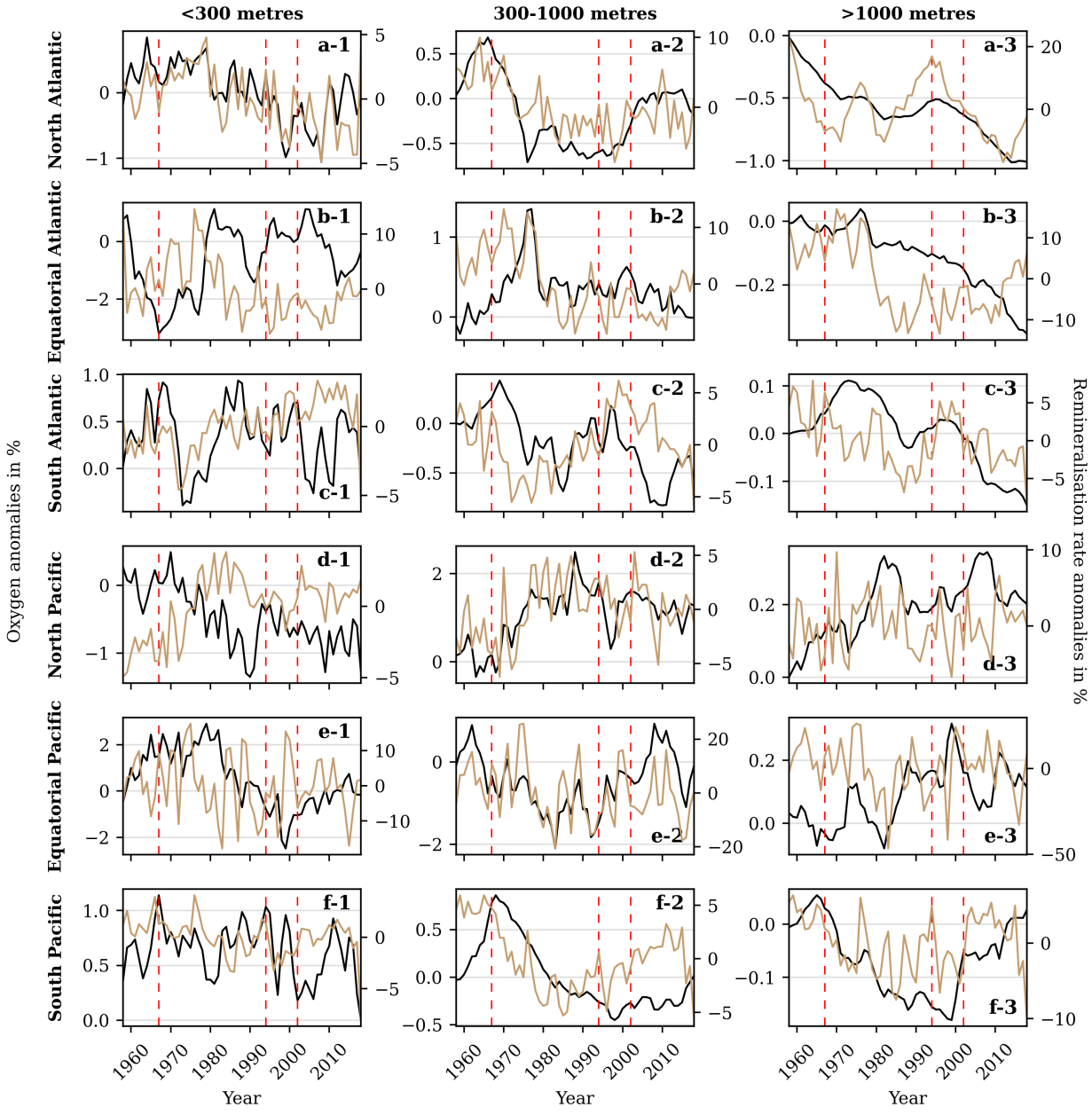

Figure continues on the next page.

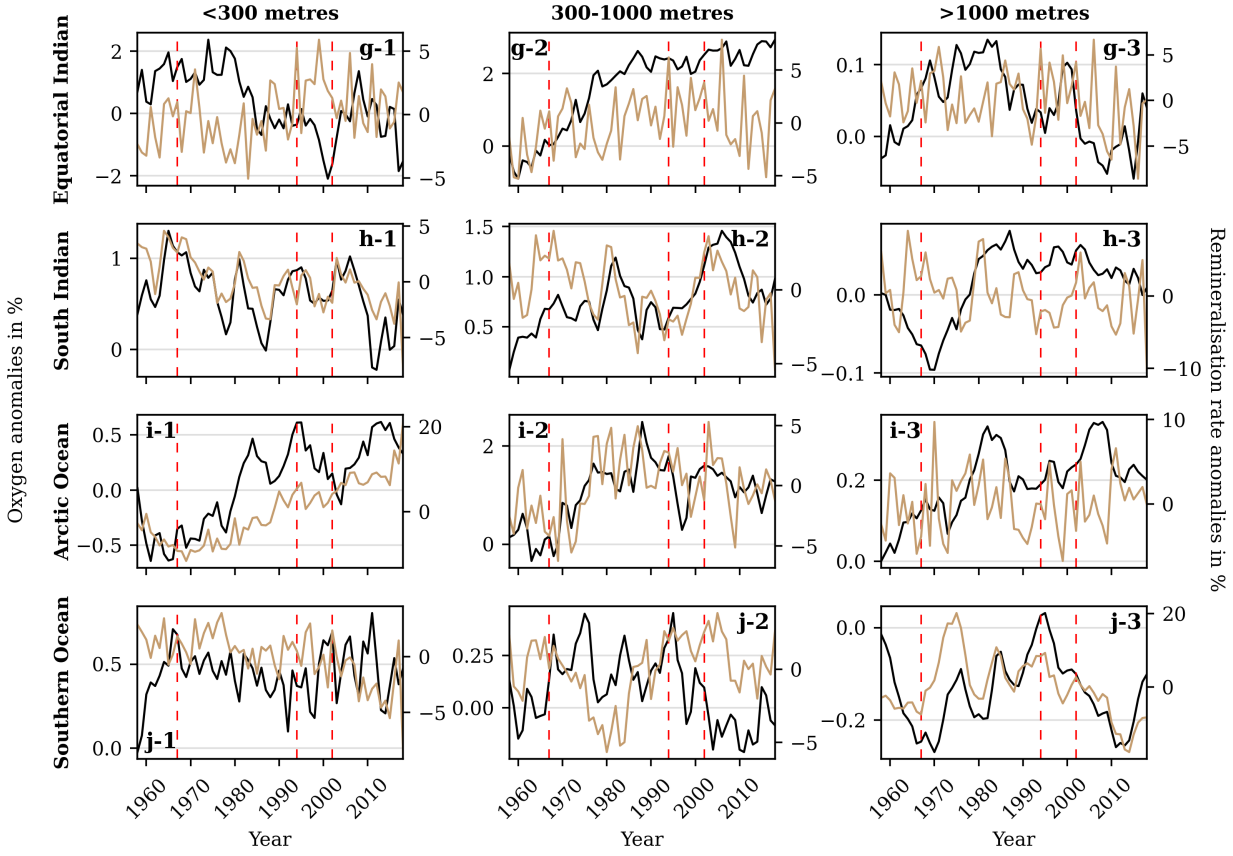

Figure A.23: Time series of O_2 inventory anomalies (black; left axis) and remineralisation rate anomalies (brown; right axis) in percent (relative to the long-term climatological mean; 1958-2018) for 10 different ocean regions (rows) over 3 different depth ranges (columns). An overview of the area boundaries for the sub-regions is shown in Figure A.16. Red dashed lines mark the four different periods of O_2 content evolution as described in Section 4.1.1.

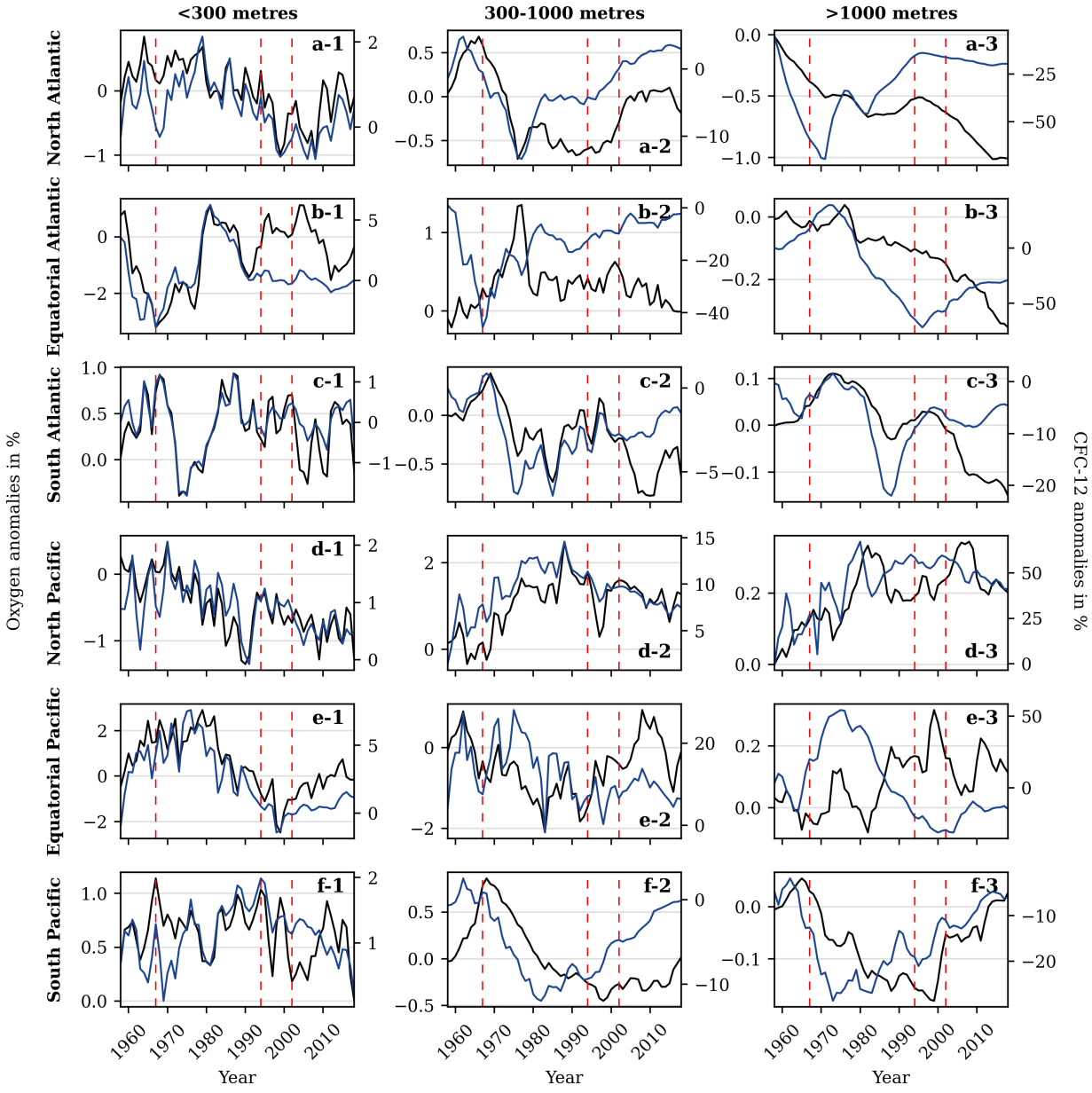

Figure continues on the next page.

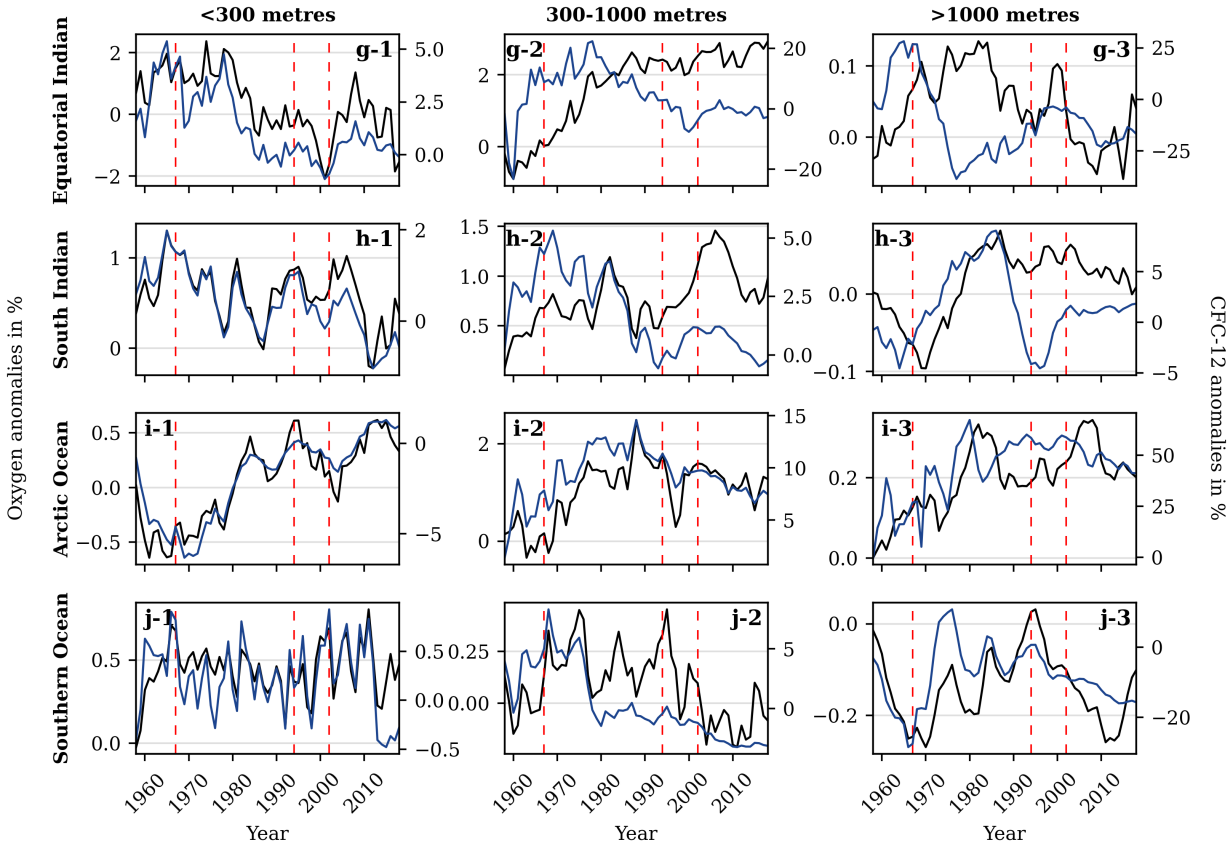

Figure A.24: Time series of O_2 inventory anomalies (black; left axis) and CFC-12 inventory anomalies (blue; right axis) in percent for 10 different ocean regions (rows) over 3 different depth ranges (columns). An overview of the area boundaries for the sub-regions is shown in Figure A.16. For O_2 inventory anomalies, percentages are computed relative to the 1958-2018 mean. Instead, for CFC-12 inventory anomalies, percentages are computed relative to the CFC-12 inventory (inv.) of the respective year ($HIND_{ns} \div CLIM \times 100$) to adjust for the increase in CFC-12 inv. over 1958-2018 and the inherently smaller absolute CFC-12 inv. anomalies (HIND-CLIM) at the beginning of the simulation. Red dashed lines mark the four different periods of O_2 content evolution as described in Section 4.1.1.

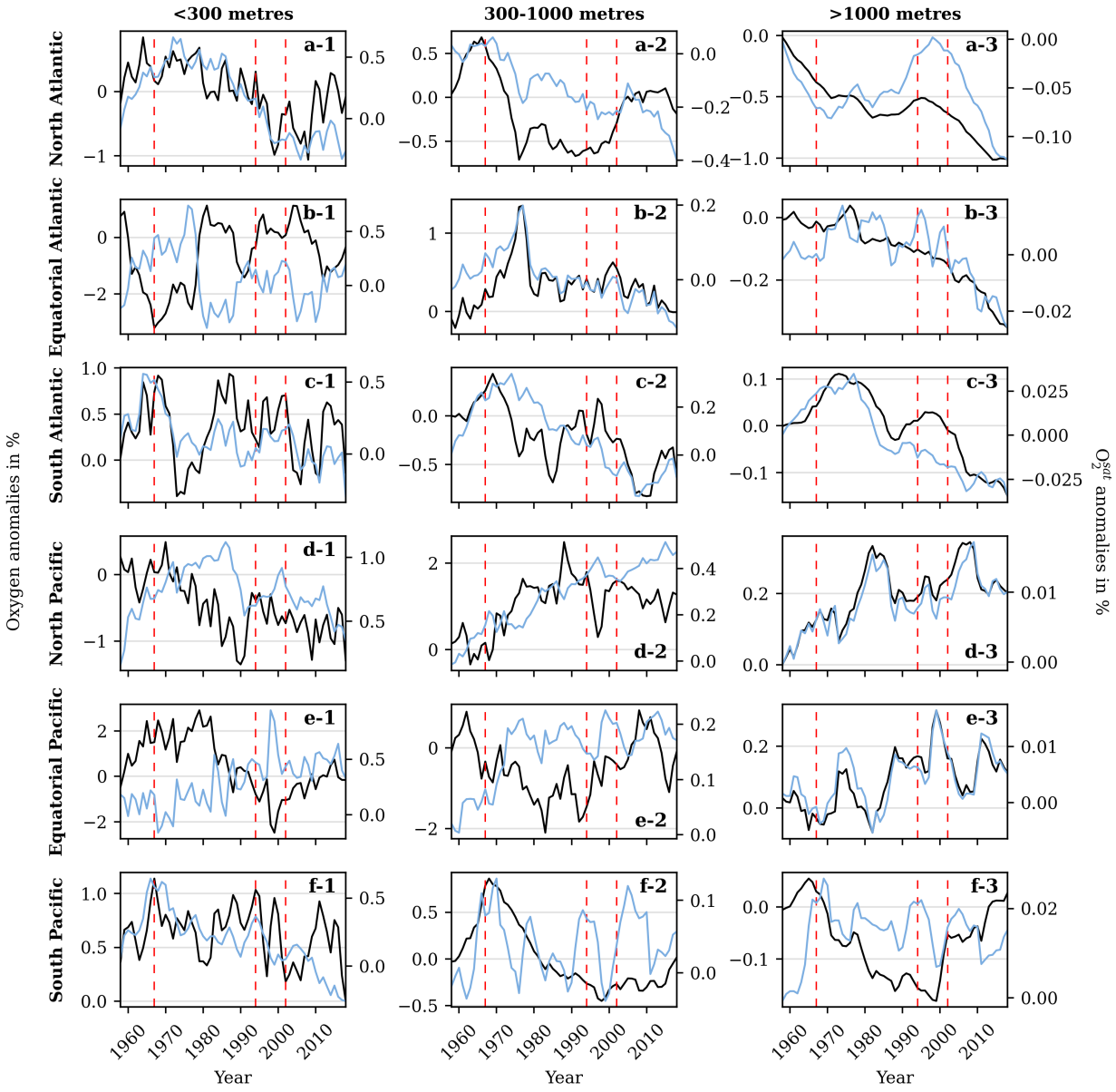

Figure continues on the next page.

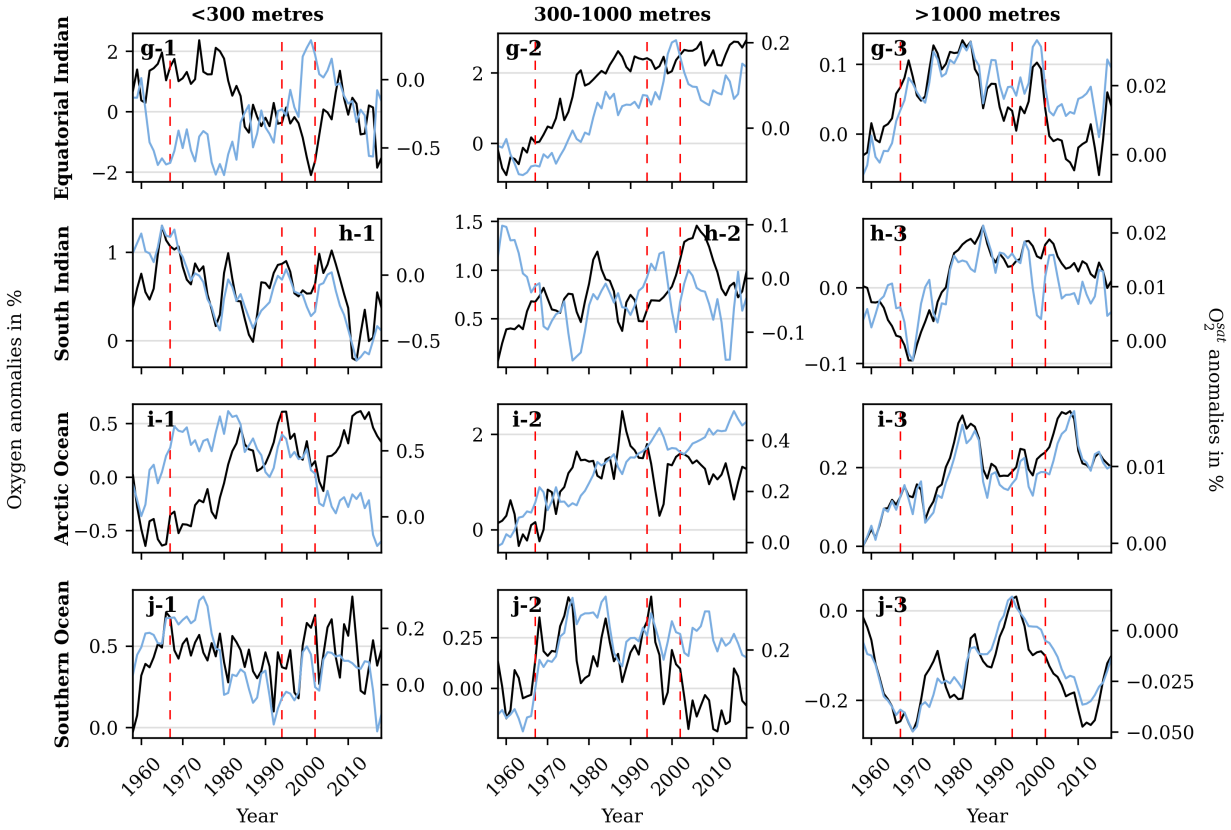

Figure A.25: Time series of O_2 inventory anomalies (black; left axis) and O_2^{sat} anomalies (blue; right axis) in percent (relative to the long-term climatological mean; 1958-2018) for 10 different ocean regions (rows) over 3 different depth ranges (columns). An overview of the area boundaries for the sub-regions is shown in Figure A.16. Red dashed lines mark the four different periods of O_2 content evolution as described in Section 4.1.1.

Statutory Declaration

I hereby declare that I have prepared this thesis independently and without outside assistance. I have not used any sources or aids other than those indicated.
The submitted written version of the thesis corresponds to the one on the electronic storage medium.
Furthermore, I certify that this work has not been submitted as a thesis elsewhere.

Helene A. L. Hollitzer	26.09.2023
Name	Date
	1168066
Signature	Matriculation Number